



Title	Study on the Relation between Interfacial Electronic Connection and Functionality of Chemically Modified Electrodes
Author(s)	佐藤, 志野
Citation	北海道大学. 博士(理学) 甲第12319号
Issue Date	2016-03-24
DOI	10.14943/doctoral.k12319
Doc URL	<a href="http://hdl.handle.net/2115/64838">http://hdl.handle.net/2115/64838</a>
Type	theses (doctoral)
File Information	Shino_Sato.pdf



[Instructions for use](#)

**Study on the Relation between  
Interfacial Electronic Connection and Functionality  
of Chemically Modified Electrodes**

分子修飾電極における金属－分子界面接合と機能性の解明

**Shino Sato**

*Graduate School of Chemical Sciences and Engineering,  
Hokkaido University*

**2016**





# Contents

## **Chapter 1 General introduction ..... 1**

1.1 Design of functional electrode surfaces	1
1.2 Chemically functionalized electrodes	4
1.3 Background information related to the work	6
1.3.1 Molecular functions of metal-macrocyclic complexes	6
1.3.2 Theoretical treatment of intramolecular and intermolecular electron transfers	10
1.3.3 Kinetic analysis of interface electron transfers using a rotating disk electrode	12
1.4 This work	14

## **Chapter 2 layer-by-layer assembly of functional molecular layers on a metal surface ..... 19**

2.1 Introduction	19
2.2 Experimental	20
2.2.1 Layer-by-layer fabrication of chemically modified electrodes	20
2.2.2 Characterization methods of the fabricated molecular layers	23
2.3 SAMs of wire molecules on an Au electrode	24
2.4 Control of metal-molecule junctions using monoatomic metal overlayers	27
2.5 Surface density of metalloporphyrins adsorbed on SAM-covered electrodes	29
2.5.1 Metalloporphyrin monolayer	29
2.5.2 Metalloporphyrin bilayer	32

## **Chapter 3 Kinetic behavior of electrochemical reactions on catalytic active sites connected with an Au electrode ..... 36**

3.1 Introduction	36
3.2 Experimental	37
3.3 ORR rates of CoP/wire/Au	38
3.4 Influence of wire structures on ORR rates	41

3.5 Influence of metal-anchor junctions 48

3.6 Conclusion 53

**Chapter 4 Internal quantum efficiency of photo-induced uphill electron transfer through photo-absorbing dyes connected with an Au electrode**

..... 60

4.1 Introduction 60

4.2 Experimental 61

4.3 Contribution of electron- and energy-transfer between the metal substrate and dye molecules to IQE 62

4.3.1 Photoelectrochemical characteristics of RuP/ImC<sub>9</sub>SH-SAM/Au 62

4.3.2 Wire length dependence of IQE for a series of RuP/wire molecule/Au 64

4.4 Contribution of energy-transfer between dye molecules to IQE 66

4.5 Conclusion 71

**Chapter 5 General conclusion ..... 76**

**Acknowledgments 78**

# Chapter 1

## General introduction

### 1.1 Design of functional electrode surfaces

Electron transfer at electrode-electrolyte interfaces is one of main issues in physical chemistry. This is related to the interaction between electrical energy and chemical change. Thus, various functions are realized by controlling interfacial electron transfers. For example, fuel cells are an electrochemical device that converts chemical energy to electrical energy using redox reactions at electrode surfaces.<sup>1,2</sup> Photovoltaic devices treat a conversion from solar energy to electrical energy through management of separation of photo-excited electron-hole pairs using interface potential.<sup>3-5</sup> Electrochemical sensors can be realized by the use of selective electrochemical reactions or molecular recognition at chemically designed electrode surfaces.<sup>6-8</sup> These interfacial electron transfers are thought of as a conversion between conducting electrons in delocalized electronic states of a metallic electrode and localized electrons in molecular orbitals of reactants or products. It is, therefore, obvious that physical and chemical properties of electrode surfaces affect the efficiency of this conversion. Indeed, the relation between the electrochemical reactivity and surface structures has been extensively studied in various reactions.<sup>9-12</sup> For example, the

oxygen reduction reaction (ORR) activity of Pt-group metals is known to be surface structure-sensitive on the atomic scale.<sup>11</sup> Figure 1.1.1 shows influence of surface morphology and electronic surface properties on the ORR activity in acidic solution, measured for pure Pt and Pt<sub>3</sub>Ni alloy single-crystal surfaces. For both of Pt and Pt<sub>3</sub>Ni crystals, the surface atomic

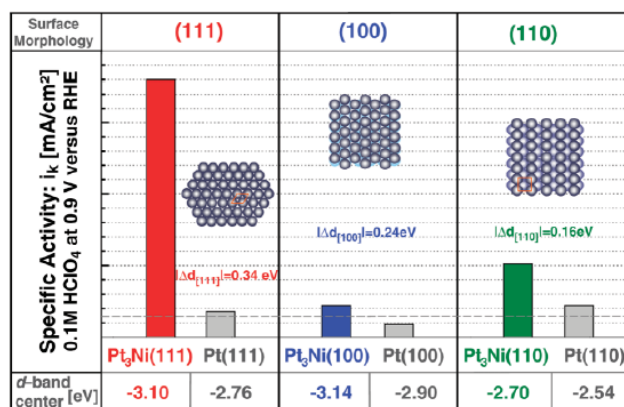


Figure 1.1.1. Influence of surface morphology and electronic surface properties on kinetics of ORR, measured for Pt and Pt<sub>3</sub>Ni surfaces. (ref11)

layers consist of pure Pt atoms (i.e., all form the so-called Pt-skin structures). Therefore, the activity difference between Pt and Pt<sub>3</sub>Ni crystals with same orientations is attributed to the difference in surface electronic structures of the Pt skin layers induced by the electronic and

structural differences of bulk crystals. Moreover, the crystal orientation dependence of the activity is induced by the difference in the surface electronic structures as well as the difference in the number of free Pt sites available for the adsorption of O<sub>2</sub>. Accordingly, Pt<sub>3</sub>Ni crystals showed the highest activity on (111) face while Pt crystals on (110) surface. Clearly, it is difficult to reach comprehensive understanding of such a complicated relation for various electrochemical reactions. So far, there is no general strategy for constructing active or functional surface structures.

For better understanding of surface functions, it is useful to consider a simple model electrode consisting of functional surface sites and a conducting substrate (for Pt<sub>3</sub>Ni, the Pt skin layer and the bulk crystal correspond to the functional surface layer and the substrate, respectively). In this model, the overall performance should be dependent on the internal electron transfer (IET) through the substrate–functional site connections as well as the chemical electron

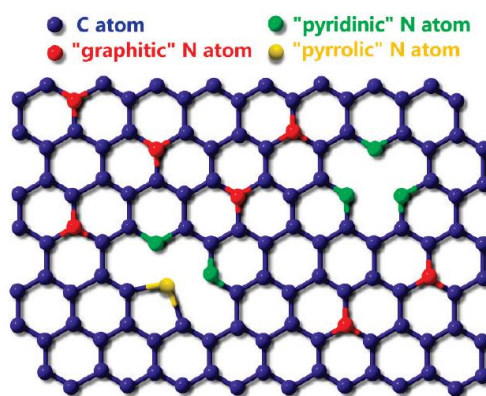


Figure 1.1.2. N-doped graphene with catalytic active N sites (ref15), which is an example of the strongly coupled connection between substrate and functional sites.

transfer (CET), which initiates chemical reactions, between the functional sites and electrolytes. For the electronic connection between the substrate and functional surface sites, two theoretical approximation conditions can be assumed, depending on the coupling strength; the strong coupling and the weak coupling limits. In the approximation of the strong coupling limit, the functional surface sites is not independent of the electronic structure of the substrate, and thus theoretical design of catalytic sites is rather complicated; although the influence of IET to the overall function may be negligible, the kinetics of CET is dependent on both of the functional layer and the substrate. For example, the property of Pt<sub>3</sub>Ni is clearly explained by this model, as already mentioned. Another example is a boron nitride (BN) layers formed on Au surface.<sup>13,14</sup> The ORR activity is induced as a result of the interaction between BN and Au even though BN is originally an insulator. Nitrogen-doped graphene is also a typical case for this limit. As shown Figure 1.1.2, nitrogen atoms are embedded into the conducting carbon matrix, and these nitrogen sites are believed to function as catalytic sites for ORR.<sup>15</sup> However, the detailed mechanism of

the activity enhancement still remains under discussion. These examples strongly suggest that unified design of functional electrodes is difficult under the condition of the strong coupling limit. Nevertheless, many attempts for fabricating functional electrodes have been made by direct attachment of functional molecules onto a conducting substrate such as carbon, graphite, or a metal surface, because of the experimental simplicity.

In the weak coupling limit, on the other hand, IET and CET can be separately treated theoretically and experimentally. This means that the design of functional electrodes can be simplified under the condition of the weak coupling limit. Actually, the overall reaction rate under this condition may be limited by IET between the electrode and the catalytic sites rather than CET between the functional sites and

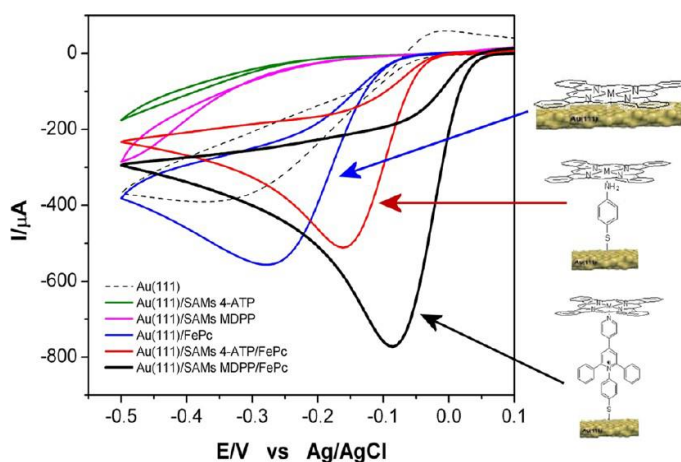


Figure 1.1.3. Comparison of ORR polarization curves on three different electronic coupling between Fe phthalocyanine and Au electrodes. (ref16).

reactant molecules. Therefore, in a practical system, the coupling strength needs to be optimized between these two limits in order to maximize the overall reaction rate. In this sense, a molecular catalyst–modified electrode seems to be a good model to investigate this issue. For example, Zagal and co-workers has reported that the ORR activity of Fe phthalocyanine (FePC) on Au electrode was varied with the structure of FePC–Au junctions, as shown in Figure 1.1.3.<sup>16</sup> Although they did not consider the influence of IET to the overall reaction rate, it is natural to consider the importance of IET in molecule-modified electrodes. Indeed, the kinetics of IET between the substrate and functional sites has been extensively studied in the absence of CET.<sup>17-21</sup> For example, a ferrocene-terminated alkanethiol monolayer on a metal electrode exhibits characteristic redox behavior of ferrocene moieties. When the chain length is sufficiently long, their kinetics is well explained by assuming that IET is a typical quantum electron tunneling process through the alkyl chains.<sup>20,22</sup> Unfortunately, limited information is currently available for heterogeneous electrochemical reactions involving both IET and CET.<sup>23</sup> For further improvement in molecular-scale design of electrocatalysts, therefore, it is necessary to understand

how the electronic coupling among the conducting electrode and catalytic active sites affects the overall kinetics.

## 1.2 Chemically functionalized electrodes

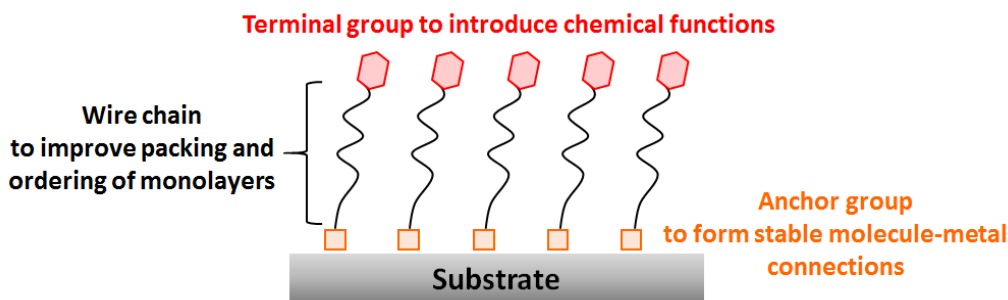


Figure 1.2.1. Illustration of a functional molecule-covered electrode surface.

As discussed in the previous section, chemically functionalized electrodes, i.e., molecular monolayer-covered metal electrodes, are a good model for studying the relation the surface structure and the functionality under the approximation of the weak coupling limit. Molecule-modified functional electrodes may be constructed self-assembly using molecules consisting of a terminal functional group, wire chain, and anchor group, as shown in Figure 1.2.1. The terminal group acts as a functional site, which characterize the functionality of the electrode. The anchor group is needed to immobilize the molecule on the surface. For the wire chain, a long alkyl chain is usually utilized to improve packing and ordering of the monolayers. In this thesis, however, the structure of the wire chain is considered as one of the key factors to control the electronic coupling between the functional sites and substrate. The terminal group may consist of a single

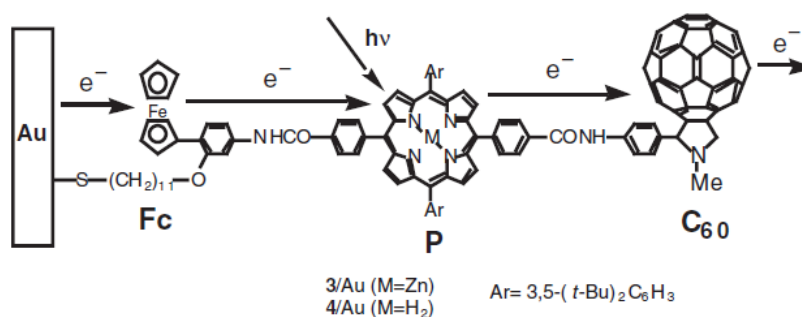


Figure 1.2.2. An example of supramolecular system with integrated multiple functional components, which is fabricated using pre-synthesized molecules. (ref24)

molecular component such as porphyrin or ferrocene or of a supramolecule with multiple molecular components. Figure 1.2.2 shows an example for supramolecule-modified electrodes with functional sites consisting of a ferrocene-porphyrin-fullerene linked structure.<sup>24</sup> The porphyrin moiety absorbs photon energy, and a pair of ferrocene and fullerene improves the charge separation efficiency, leading to efficient photo-energy conversion. When SAMs with such a complicated structure are fabricated, the constituent molecules are normally pre-synthesized.<sup>24-27</sup> Unfortunately, it is difficult

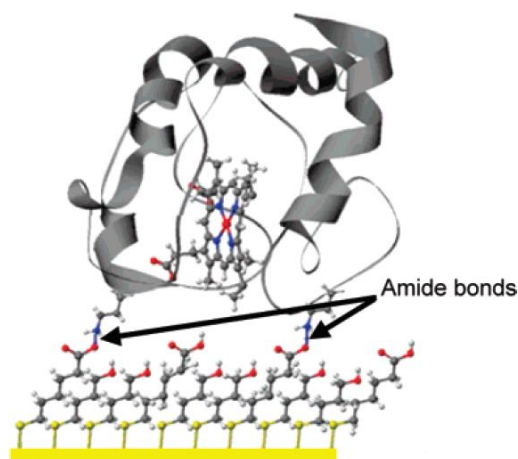


Figure 1.2.3. Illustrate of a covalent SAM/cytochrome *c* layer-by-layer assembly resulting from the formation of multiple amide bonds between  $\text{-COOH}$  terminated on the SAM and lysine residues on cytochrome *c*. (ref28)

for such molecules with a bulky terminal group to form well-organized SAMs. The quality of SAMs may influence the overall functionality. When more complicated or large functional groups such as proteins are utilized as terminal groups, the pre-synthesis of functional molecules is no longer useful for fabricating chemically functionalized surfaces. Alternatively, layer-by-layer assembly is thought to be useful. Figure 1.2.3 shows the layer-by-layer assembly of cytochrome *c* on Au surface.<sup>28</sup> In this case, well-organized SAMs of wire molecules are firstly formed, and then cytochrome *c* protein molecules are attached on top of the SAM through amide bond formation.<sup>28-31</sup> The quality of the wire-molecule SAMs is independent of the structure of functional molecules in this system, and hence, it is expected that the electronic coupling between the functional groups and metal substrate can be well controlled by alternating wire molecules.

## 1.3 Background information related to the work

### 1.3.1 Molecular functions of metal-macrocylic complexes

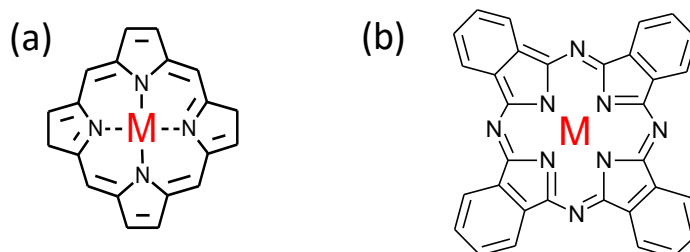


Figure 1.3.1. Molecular structures of (a) metalloporphyrin, (b) metallophthalocyanine.

Metal-macrocylic complexes such as metalloporphyrin and metallophthalocyanine are extremely versatile materials with multi-functionality. Because of the multi-functionality, metal-macrocylic complexes are suitable as a model for functional molecules. In this thesis, therefore, a variety of metal-macrocylic complexes were utilized to form functional surface sites. As shown in Figure 1.3.1, they possess a  $N_4$  inner structure that is common in naturally occurring molecules such as chlorophyll, heme groups in hemoglobin, cytochrome c, vitamin B12, and so on. Due to their macrocylic nature including extended-systems, metal-macrocylic complexes are capable of undergoing fast redox processes, with minimal reorganizational energies and can act as mediators in electron transfer processes involving a great variety of molecules.<sup>32-36</sup> Moreover, metal-macrocylic complexes are also promising for promoting photocatalytic reactions. They can act as spectroscopic sensitizers deposited on semiconductor electrodes<sup>37-51</sup> or metal electrodes and can have applications in photo-energy conversion devices. Metalloporphyrin color is due to optical transition within a porphyrin ligand involving the excitation of electrons from  $\pi$  to  $\pi^*$  porphyrin ring orbital. Figure 1.3.2 shows the absorption spectrum of Ru-tetraphenylporphyrin exhibiting two distinct absorption bands. The first strong peak at about 400 nm, which is called the Soret or B band, is assigned to the transition from the ground state to the second excited state ( $S_0 \rightarrow S_2$ ). The second absorption region in the range between 500-700 nm (the Q bands) is

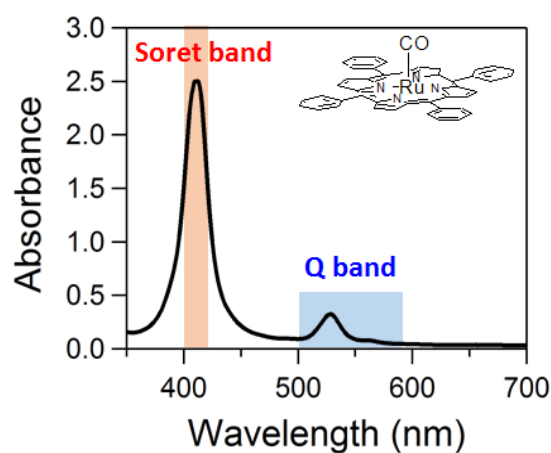


Figure 1.3.2. Typical absorption spectrum for a Ru-tetraphenylporphyrin.

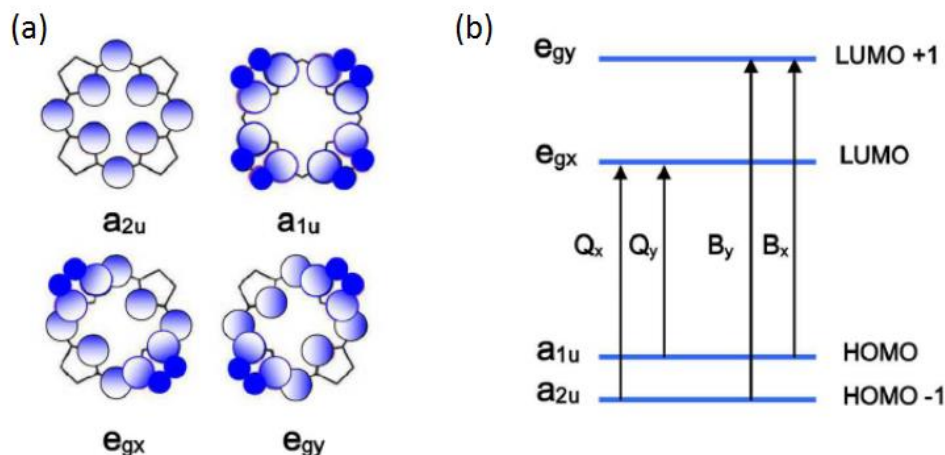


Figure 1.3.3. Porphyrin HOMOs and LUMOs. (a) Representation of the four Gouterman orbitals in porphyrins. (b) Drawing of the energy levels of the four Gouterman orbitals. The set of  $e_g$  orbitals gives rise to Q and Soret bands.

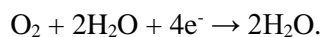
assigned to a weak transition to the first excited state ( $S_0 \rightarrow S_1$ ). These transitions can be well explained by considering the Gouterman's four-orbital model of porphyrin excited states, as shown in Figure 1.3.3.<sup>52,53</sup> According to this theory, the absorption bands in porphyrin systems arise from transitions between two  $\pi$  highest occupied orbitals (HOMOs) and two  $\pi^*$  lowest unoccupied orbitals (LUMOs), and it is the identities of the metal center and the substituents on the ring that effect the relative energies of these transitions. The HOMOs are represented as an  $a_{1u}$  and an  $a_{2u}$  orbital, while the LUMOs are represented as a degenerate set of  $e_g$  orbitals. The transitions from the two HOMOs and the doubly degenerated LUMO account for the typical spectrum of porphyrins.

Metal-macrocylic complexes are also known to be a good catalyst for oxygen reduction reaction (ORR).<sup>16,54-68</sup> This triggered extensive research on metal-macrocylic complexes as possible electrocatalysts for ORR for the development of low cost fuel cells in many places in the world. Porphyrins constitute an interesting type of catalysts since they present several advantages over noble metals such as platinum, not only because of the cost. In particular, they provide very interesting models for theoretical and experimental studies since their catalytic action can be described in terms of definite parameters such as chemical structure and chemical and physical properties. This is of course an essential point to investigate the relation between the surface structure and functionality in this thesis.

ORR is a multi-electron reaction that has two main possible pathways: one involving the transfer of two electrons to produce  $H_2O_2$ , and the other, a direct four-electron pathway to produce water. The two-electron pathway can be written as:



The direct four-electron pathway can be written as:



The adsorption of  $\text{O}_2$  to the metal center is the first step for ORR on metal-macrocylic complexes. The interaction between catalyst and  $\text{O}_2$  molecule and its effect to dissociation of O-O bond is important in understanding the reaction mechanism. The O-O bond cleavage of  $\text{O}_2$  molecule is necessary for the four-electron ORR. Tsuda et al. attributed the ORR abilities of metal-macrocylic complexes to dissociate  $\text{O}_2$  into the lowest unoccupied molecular orbital and highest occupied molecular orbital (LUMO-HOMO) characters.<sup>54</sup> Therefore, the type of central metal atom determinatively influences their catalytic activities. Actually, Fe porphyrin (FeP) and Fe phthalocyanine (FePC) are known to promote four-electron ORR pathway, whereas Co porphyrin (CoP) and Co phthalocyanine (CoPC) are act as two-electron ORR catalyst.<sup>16,54-62</sup> Moreover, Wang et al. mentioned that the two- or four-electron reduction process is dependent on the oxygen adsorption configuration; a side-on adsorption configuration leads to four-electron reduction, and an end-on adsorption leads to two-electron reduction, as illustrated in Figure 1.3.4.<sup>62</sup> For end-on  $\text{M-O}_2$  complexes, the major

interaction for both  $\sigma$  and  $\pi$  bonding occurs with the  $\pi^*$  antibonding orbitals of the  $\text{O}_2$ .

The  $\sigma$  interaction is essentially between the metal  $3d_{z^2}$  and the in plane  $\pi_g^s$  orbital (symmetric orbital) of dioxygen with

respect to the  $\text{MO}_2$  plane. This can be viewed as an electron transfer from the metal ion to  $\text{O}_2$ . The  $\pi$  interaction involves essentially the metal  $3d_{yz}$  and the  $1\pi_g^a$  ( $\pi$  antibonding antisymmetric orbital) on the  $\text{O}_2$  and can be visualized as a back-bonding interaction. In both interactions the  $\pi_u^s$  and  $\pi_u^a$  play a lesser role in the composition of the bonding orbitals. For the side-on interaction, a  $3d_{z^2}$  orbital of the metal will interact with the  $1\pi_u^u$  bonding orbital (back-bonding interaction) and a  $3d_{xz}$  with a  $1\pi_g^s$  antibonding orbital of dioxygen. Figure 1.3.5 shows the optimized structural configurations for the  $\text{O}_2$  adsorbed on FePC and CoPC molecules.<sup>63</sup> Shi and Zhang conducted a density functional theory study of metal phthalocyanines and metal

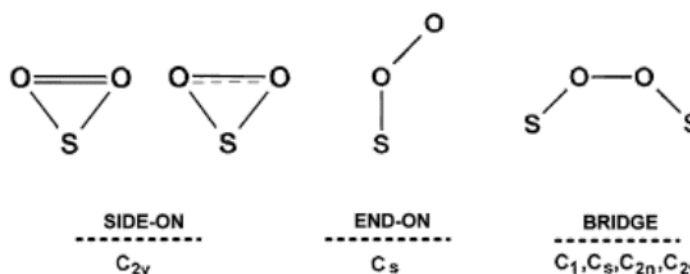


Figure 1.3.4. Possible configurations for molecular oxygen for its interaction with active sites on the electrode surface.

porphyrins to investigate the dioxygen-binding abilities and their relation with the catalytic activity.<sup>63,68</sup> They investigated both end-on and side-on binding modes. Density functional theory calculations have indicated that O<sub>2</sub> interacts with CoPC via an end-on interaction whereas for FePC both end-on and side on interactions are plausible. They also evaluated the electronic properties of the complexes such as the ionization potential and Mulliken charge. The catalytic activity varied linearly with the ionization potential. The ionization potential correlates

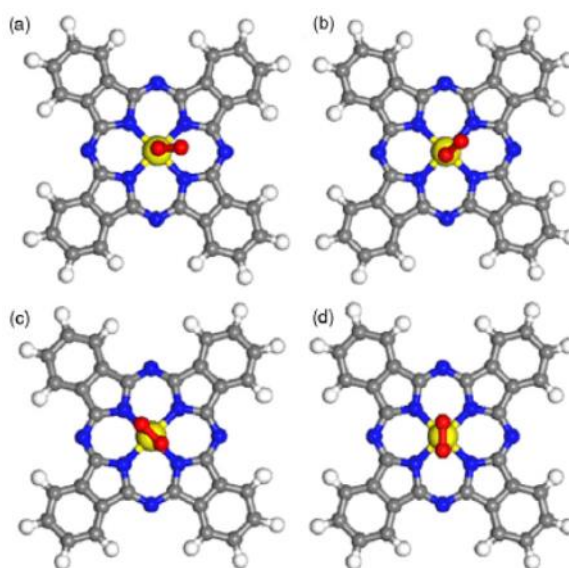


Figure 1.3.5. Optimized structural configurations for the O<sub>2</sub> adsorbed on FePC and CoPC molecules. (a) and (b) two end-on configurations. (c) and (d) two side-on configurations. The central yellow ball represents metal Fe or Co atom, the central two red balls represent the adsorbed O<sub>2</sub> molecules, blue balls represent N atoms, gray balls represent C atoms and light white balls represent H atoms. (ref63)

directly with the redox potential of the catalysts, based on previous experimental studies by Zagal and co-workers.<sup>64-66</sup> Co porphyrins have high ionization potentials, which make them better catalysts than the iron counter parts. In contrast with other phthalocyanines, iron derivatives have large ionization potentials and better oxygen binding ability which makes them good catalysts for O<sub>2</sub> reduction.

The active site in metal-macrocylic complexes usually involves the M(II) state. In the case of Co complexes, Co(III) is probably not formed upon its interaction with the dioxygen molecule since the Co(III)/(II) redox process occurs at much

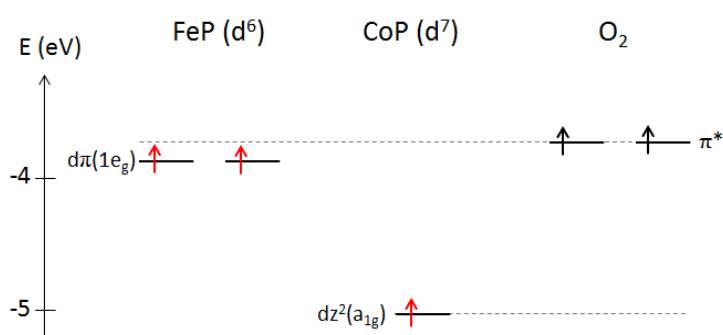


Figure 1.3.6. Relative orbital energies of dioxygen, FeP, and CoP. For simplicity, only one electron is shown on a single occupied molecular orbital of FeP and CoP.

more positive potentials than the Fe(III)/Fe(II) process but first step is still crucial since the catalytically active site is Co(II). Co atom generally has a small Mulliken charge than the

corresponding Fe atom. This is due to lower d orbital energies of Co, which make them easier to gain electrons than the corresponding Fe orbitals. The calculated HOMO energies of CoPC systems are in general lower than that of O<sub>2</sub> (which has a higher HOMO energy), as shown in Figure 1.3.6. Electron-donating substituent raises the Co 3d orbital energy; hence, the energy gap between the interaction orbitals of Co and O<sub>2</sub> decreases, so the dioxygen binding energy increases.<sup>64,67</sup> For FePC, HOMO is 3d Fe orbital, which lies very close to the HOMO of O<sub>2</sub> and both electron-donating and withdrawing groups increase the energy gap, so the dioxygen binding energies decrease.<sup>64</sup> For ORR on FePC or FeP, O<sub>2</sub> is reduced to H<sub>2</sub>O; for that on CoPC or CoP, O<sub>2</sub> is just reduced to H<sub>2</sub>O<sub>2</sub>. The difference energy level of the 3d orbital between FePC and CoPC strongly affect the ORR pathway.

In the earlier studies, most of the work was focused on the ORR but was later shown over the years that they catalyze a myriad of reactions. Some porphyrins and related macrocyclic complexes catalyze, for example (i) the electrooxidation of formic acid, CO and SO<sub>2</sub><sup>69-71</sup> (ii) the electroreduction of H<sub>2</sub>O<sub>2</sub>, CO<sub>2</sub>, NO.<sup>72-74</sup> Therefore, the use of metal-macrocyclic complexes as functional molecules can be investigated to systematic electron transfer reaction on multi-chemical reactions.

### 1.3.2 Theoretical treatment of intramolecular and intermolecular electron transfers

In this thesis, the rate of CET between surface active sites and reactants, i.e., intermolecular electron transfer, is of great importance that characterizes the functionality of the electrode. In the weak coupling limit, the rate of IET through wire molecules, i.e., intramolecular electron transfer, is another important factor to affect the performance of the functional electrode. Although these two factors may not be separately quantified under the strong coupling region, it is still effective to consider the problem as a perturbation from the weak coupling limit. The theoretical aspects of electron transfers is well described by Marcus theory. The original Marcus theory was formulated to explain outer sphere electron reactions, but the extended theory is now used to describe a number of important processes in chemistry and biology including photosynthesis.<sup>3</sup> When electron transfer in a donor-bridge-acceptor (D-B-A) model is considered in the nonadiabatic limit, the rate of electron transfer is given by

$$k_{D \rightarrow A} = 2\pi/\hbar |V_{DA}|^2 D_{FC} \quad (1)$$

where  $V_{DA}$  is the coupling between the donor and acceptor electronic states and  $D_{FC}$  is the Franck-Condon-weighted density of nuclear states coupled to vibronic reservoirs. The coupling,  $V_{DA}$ , is critically dependent on the bridge length. For the simple model, the long bridge may be described by a chain of repeated molecular units. Besides, it is assumed that the nearest-neighbor coupling is effective among the units and the interaction between D and A is in the weak coupling limit. Then, if the quantum electron tunneling is assumed as the electron transfer mode, the rate of electron transfer is described in terms of  $N$ , the number of the units in the chain, as:

$$k_{D \rightarrow A} = k_0 \exp(-\beta N), \quad (2)$$

or in terms of the distance,  $r_{DA}$ , as:

$$k_{D \rightarrow A} = k_0 \exp(-\beta r_{DA}) \quad (3)$$

Here,  $\beta_N$  or  $\beta$  is the decay coefficient. Note that this exponential relation will be broken when the approximation of the weak coupling limit is broken between D and A, which is expected for very short  $r_{DA}$ . Experimentally, the length dependence of electron transfer has been extensively studied in metal-molecule-metal junctions.<sup>75-79</sup> When a metal-molecule-metal junction is treated in the D-B-A model,  $D_{FC}$  is supplemented by the additional factor due to the electronic manifold of the metal. The relation between the rate of electron transfer  $k_{D \rightarrow A}$  and molecular conductance,  $g$ , can be expressed as:

$$g \sim \frac{8e^2}{\pi^2 \Gamma_A \Gamma_B} \left( \frac{k_{D \rightarrow A}}{D_{FC}} \right) \quad (4)$$

where  $\Gamma_A$  and  $\Gamma_B$  are related to the coupling strength at the metal-molecule contacts. In general, the tunneling probability is related to the barrier height. In the case of the metal-molecule-metal junctions, the barrier may consist of the molecular chain body barrier and the contact barriers at both ends. For the molecular chain body barrier, many investigations have been reported in the weak coupling limit, i.e., for the long molecular wires.<sup>76,77</sup> The molecular chain body barrier is sensitive to the degree of  $\pi$ -conjugation;  $\beta$  for unsaturated molecular chains is known to be smaller than that for the saturated alkyl chains because of the difference in the HOMO-LUMO energy gap. On the other hand, limited information is available for the contact barrier because of the experimental difficulty in control of the metal-molecule interface structures on the atomic scale. In this thesis, the coupling between metal surface and functional sites is tuned by changing both of the body- and contact-barriers through alternating the structure and  $\pi$ -conjugation of wire molecules, and adsorption geometry.

### 1.3.3 Kinetic analysis of interface electron transfers using a rotating disk electrode

In this thesis, accurate evaluation of electron transfer rates is a critical point in the experiments. An electrode reaction involves mass transfer of a reactant (R) from bulk solution to the electrode surface, chemical reactions following electron transfer at the electrode surface, and mass transfer of the product (P) to the bulk solution.



The simplest electrochemical reactions are those in which the rates of all associated chemical reactions are very rapid compared to those of mass-transfer processes. When the net rate of the electrode reaction,  $v_e$ , is governed totally by the rate at which the electroactive species brought to the surface by mass transfer,  $v_{\text{mt}}$ , the reaction rate is written as

$$v_e = v_{\text{mt}} = \frac{i}{nFA} = \frac{j}{nF} \quad (6)$$

where  $A$  is the electrode area ( $\text{cm}^2$ ),  $F$  is Faraday's constant ( $\text{C}\cdot\text{mol}^{-1}$ ),  $n$  is the number of electron consumed in the electrode reaction and  $j$  is the current density ( $\text{A}\cdot\text{cm}^{-2}$ ). Mass transfer processes involve various modes such as migration, diffusion and convection, which is stirring or hydrodynamic transport. Therefore, in a conventional electrochemical situation, the rate of mass transfer is not constant and is time-dependence, as the extent of depletion of reactant near the electrode governs the rate of mass transfer, and this changes with time. This often leads to irregular or unpredictable currents. Therefore, to investigate electrode reaction kinetics, diffusion coefficients is needed to be determined by controlling mass transfer rates.

A so-called rotating disk electrode (RDE) method has been widely used to control mass transfer conditions for steady-state measurements.<sup>80</sup> This electrode has an advantage that there exists a precise theory of convection diffusion at a rotating disk. Moreover, the rates of mass transfer at the electrode surface are typically larger than the rates of diffusion alone, so that the relative contribution of mass transfer to electron-transfer kinetics is often smaller. The RDE acts as a pump, drawing the solution up toward the electrode along the  $z$ -axis (Figure 1.3.7), then finding it out radially across the electrode surface. According to Levich, the diffusion layer has the same thickness over the entire area of a rotating disk provided edge effects can be neglected. For laminar flow the diffusion layer thickness,  $\delta$ , is given by the following function:

$$\delta = 1.61D^{1/3}\nu^{1/6}\omega^{-1/2} \quad (7)$$

where  $D$  is the diffusion coefficient of the solution species ( $\text{cm}^2\cdot\text{sec}^{-1}$ ),  $\nu$  the kinematic viscosity of solvent ( $\text{cm}^2\cdot\text{sec}^{-1}$ ), and  $\omega$  is the angular velocity of the disk ( $\text{rad}\cdot\text{s}^{-1}$ ).<sup>81</sup> Thus,  $\delta$  is dependent

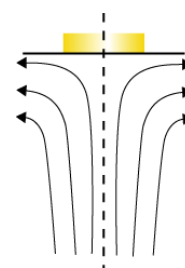


Figure 1.3.7. Schematic resultant flows.

on the rotation rate. Moreover, a mass transport limiting current on the RDE is given by

$$i_L = nFADc/\delta, \quad (8)$$

$$i_L = 0.62nFAD^{2/3}\nu^{-1/6}\omega^{1/2}c \quad (8)'$$

$c$  being the concentration of the reactant species as the Levich equation.<sup>81</sup> From RDE measurements of mass transport limiting currents, the quantity  $D \cdot c$  can be thus obtained with precision.

On the other hand, when the mass transport is not rate-limiting, the current,  $i$ , is given by the Koutecky-Levich equation,

$$\frac{1}{i} = \frac{1}{i_L} \pm \frac{1}{nFAk_e c} \quad (9)$$

Here,  $k_e$  is the first-order rate constant.<sup>81</sup> The first term in equation (9) can be varied by changing  $\omega$ , while the second term can be varied by changing the electrode potential and hence  $k_e$ . This relationship allows the relative effects of the rate of mass transport (the first term) and the rate of electrochemical reaction (the second term) on the overall reaction rate to be quantified. The practical evaluation of kinetic data (the activation-controlled current density  $i_{ac}$ , transition coefficient  $\alpha$ ) is as follows: plotting  $1/i_{ac}$  against  $1/\sqrt{\omega}$  for constant values of the overpotential  $\eta$  one deduces from the slope and the ordinate at  $\omega = \infty$  for  $k_e$ .

In the region  $\eta \gg RT/nF$ , the rate constant at a given electrode overpotential can calculate both  $i_{ac}$  and  $\alpha$  in the usual way

$$i = nFk_e = i_{ac} \exp\left(-\alpha\eta \frac{nF}{RT}\right) \quad (\text{Reduction reaction, 10})$$

$$i = nFk_e = i_{ac} \exp\left((1 - \alpha)\eta \frac{nF}{RT}\right) \quad (\text{Oxidation reaction, 11})$$

From equation (10) and (11), Tafel equation applies,

$$\eta = a + b \log |i_{ac}| \quad (12)$$

Here, the Tafel slope and intercept are  $b = 2.3RT/(anF)$  and  $-a/b = \log |i| = \log |nFk_e|$ , respectively.<sup>83</sup> The Tafel slope reaches constant values as it to be expected for purely diffusion controlled polarization. In Chapter 3, we measured the ORR rate on the catalyst-modified electrodes using the RDE method and conducted kinetic analyses.

## 1.4 This work

In this thesis, kinetics of electron transfer at metal-electrolyte interfaces through functional molecular monolayers are treated from the viewpoint of electronic coupling between the metal substrate and functional moieties, to provide valuable insights on the relation between the surface structure and functionality. A chemically functionalized metal surface is usually obtained by surface modification with molecules consisting of anchor, wire, and functional moieties. While a large number of studies on molecular design of functional moieties has been reported, very limited information is currently available regarding contributions of wire and anchor groups to the overall electron transfer kinetics. To focus on this problem, functional molecular layers are formed by stacking wire molecules and functional molecules using layer-by-layer assembly. Then, the electron transfer kinetics of the molecular layers are thoroughly investigated by alternating the combination of wire molecules and functional molecules. The main body of the thesis is divided into three parts:

The first part (Chapter 2) deals with the layer-by-layer assembly of functional molecular layers on Au electrode. As a model functional group, we focus on transition metal macrocyclic complexes such as metalloporphyrins and metallophthalocyanines because of their multifunctionality. Molecular wires with various lengths and structures are utilized to tune the electronic coupling between Au and the macrocyclic complexes. For the anchor group of the wire molecules, thiol and isocyanide groups are mainly studied, which can bind to metal surfaces strongly. The connection between wire molecules and macrocyclic complexes is formed by axial ligation of the central metal ions to terminal groups of the wire molecules. Moreover, the anchor geometry is controlled by surface modification of Au electrode with monoatomic foreign metal overlayers.

Studies on the contribution of the interfacial electronic coupling to electrochemical potential-controlled downhill electron transfers are presented in the second part (Chapter 3). Here, we focus on the catalytic activity of metalloporphyrins and metallophthalocyanines for oxygen reduction reaction (ORR).

In the third part (Chapter 4), the contribution of the electron- and energy-transfers at the metal-molecule interfaces to photo-driven uphill electron transfers are discussed using strong photo-absorbing metalloporphyrins.

Chapter 5 give a general conclusion of the thesis, along with an outlook on development of functional electrodes from fundamental aspects.

## References

- (1) Willner, I. *Science*, **2002**, 298, 2407.
- (2) Wang, B. *Angew. J. Power Sources*, **2005**, 152, 1.
- (3) Marcus, R. A. *Annu. Rev. Phys. Chem.*, **1964**, 15, 155.
- (4) Har-Lavan, R.; Ron, I.; Thieblemont, F.; Cahen, D. *Appl. Phys. Lett.*, **2009**, 94, 043308.
- (5) Grätzel, M. *Inorg. Chem.*, **2005**, 44, 6841.
- (6) Gooding, J. J. *Electroanalysis*, **2008**, 20, 573.
- (7) Gooding, J. J.; Mearns, F.; Yang, W.; Liu, J. *Electroanalysis*, **2003**, 15, 81.
- (8) Aryaa, S. K.; Sahab, S.; Ramirez-Vickc, J. E.; Guptab, V.; Bhansalid, S.; Singh, S. P. *Anal. Chim. Acta*, **2012**, 737, 1.
- (9) Stamenkovic, V. R.; Mun, B. S.; Arenz, M.; Mayrhofer, K. J. J.; Lucas, C. A.; Wang, G.; Ross, P. N.; Markovic, N. M. *Nat. Mater.*, **2007**, 6, 241.
- (10) Greeley, J.; Nørskov, J. K.; Mavrikakis, M. *Annu. Rev. Phys. Chem.*, **2002**, 53, 319.
- (11) Stamenkovic, V. R.; Fowler, B.; Mun, B. S.; Wang, G.; Ross, P. N.; Lucas, C. A.; Marković, N. M. *Science*, **2007**, 315, 493.
- (12) Mavrikakis, M.; Stoltze, P.; Nørskov, J. K. *Catal. Lett.* **2000**, 64, 101.
- (13) Uosaki, K.; Elumalai, G.; Noguchi, H.; Masuda, T.; Lyalin, A.; Nakayama, A.; Taketsugu, T. *J. Am. Chem. Soc.* **2014**, 136, 6542.
- (14) Lyalin, A.; Nakayama, A.; Uosaki, K.; Taketsugu, T. *Phys. Chem. Chem. Phys.* **2013**, 15, 2809.
- (15) Wang, H.; Maiyalagan, T.; Wang, X. *ACS Catal.* **2012**, 2, 781-794.
- (16) Ponce, I.; Silva, J. F.; Oñate, R.; Rezende, M. C.; Zagal, J. H.; Pavez, J. *J. Phys. Chem. C* **2012**, 116, 15329.
- (17) Chi, Q. J.; Zhang, J. D.; Andersen, J. E. T.; Ulstrup, J. *J. Phys. Chem. B* **2001**, 105, 4669.
- (18) Chidsey, C. E. D.; Bertozzi, C. R.; Putvinski, T. M.; Mujsc, M. *J. Am. Chem. Soc.* **1990**, 112, 4301.
- (19) Uosaki, K.; Sato, Y.; Kita, H. *Langmuir*. **1991**, 7, 1510.

- (20) Smaller, J. F.; Feldberg, S. W.; Chidsey, C. E. D.; Linford, M. R.; Newton, M. D.; Liu, Y-P. *J. Phys. Chem.* **1995**, *99*, 13141.
- (21) Kondo, T.; Uosaki, K. *J. Photochem. Photobiol. C.* **2007**, *8*, 1.
- (22) Hsu, C.-P.; Marcus, L. A. *J. Chem. Phys.* **1997**, *106*, 584.
- (23) Imahori, H.; Norieda, H.; Nishimura, Y.; Yamazaki, I.; Higuchi, K.; Kato, N.; Motohiro, T.; Yamada, H.; Tamaki, K.; Arimura, M. et al. *J. Phys. Chem. B* **2000**, *104*, 1253.
- (24) Yamada, H.; Imahori, H.; Nishimura, Y.; Yamazaki, I.; Ahn, T. K.; Kim, S. K.; Kim, D.; Fukuzumi, S. *J. Am. Chem. Soc.*, **2003**, *125*, 9129.
- (25) Liu, J.; Paddon-Row, M. N.; Gooding, J. J. *J. Phys. Chem. B* **2004**, *108*, 8460.
- (26) Wang, Y.; Yao, X.; Wang, J.; Zhou, F. *Electroanalysis*, **2004**, *16*, 1755.
- (27) Kilian, K. A.; Böcking, T.; Gaus, K.; Gal, M.; Gooding, J. J. *ACS Nano*, **2007**, *1*, 355.
- (28) Davis, K. L.; Drews, B. J.; Yue, H.; Waldeck, D. H.; Knorr, K.; Clark, R. A. *J. Phys. Chem. C* **2008**, *112*, 6571.
- (29) Fabre, B.; Hauquier, F. *J. Phys. Chem. B*, **2006**, *110*, 6848.
- (30) Lin, V. S.-Y.; Motesharei, K.; Dancil, K.-P. S.; Sailor, M. J.; Ghadiri, M. R. *Science*, **1997**, *278*, 840.
- (31) Kilian, K. A.; Böcking, T.; Gooding, J. J. *Chem. Commun.*, **2009**, 630.
- (32) Moser, F. H.; Thomas, A. L.; The Phthalocyanines, vols. 1 and 2, CRC Press, Boca Raton, FL, 1983.
- (33) Katalyse und Phthalocyaninen, M. Kropf, F. Steinbach (Eds.), Georg Thieme, Verlag Stuttgart, 1973.
- (34) Manassen, J. *Catal. Rev. Sci. Eng.* **1974**, *9*, 223.
- (35) Bocler, L. J.; in: G.A. Melson (Ed.), Coordination Chemistry of Macrocyclic Compounds, Plenum Press, New York, 1979.
- (36) Leznoff, C. C.; Lever, A. B. P. Phthalocyanines, Properties and Applications, vols.1-4, VCH Publishers Inc., New York, 1989.
- (37) Tachikawa, M.; Faulkner, L. R. *J. Am. Chem. Soc.* **1978**, *100*, 4379.
- (38) Minami, N.; Watanabe, T.; Fujishima, A.; Honda, K.; Bunsenges, B. *Phys. Chem.*, **1976**, *83*, 476.
- (39) Fan, F. F.; Bard, A.J. *J. Am. Chem. Soc.* **1979**, *101*, 6139.
- (40) Shepard Jr., V. R.; Armstrong, N. R. *J. Phys. Chem.* **1979**, *83*, 1268.
- (41) Fan, F.; Faulkner, L. R. *J. Am. Chem. Soc.* **1979**, *101*, 4779.
- (42) Minami, N. *J. Chem. Phys.* **1980**, *72*, 6317.
- (43) Nakato, Y.; Shioji, M.; Tsuboura, M. *J. Phys. Chem.* **1981**, *85*, 1670.
- (44) Klofta, T.; Linkous, C.; Armstrong, N. R. *J. Electroanal. Chem. Interfacial Electrochem*

- 1985**, 185, 73.
- (45) Loempoel, P.; Castro-Acuña, A.; Dan, F. R. F.; Bard, A. J. *J. Phys. Chem.* **1982**, 86, 1396.
- (46) D. Schlettwein, in: Zagal, J. H.; Bedioui, F.; Dodelet, J. P. (Eds.), *N<sub>4</sub> Macrocyclic Metal Complexes*, Springer, New York, 2006, p. 467.
- (47) Flora, W. H.; Hall, H. K.; Armstrong, N. R. *J. Phys. Chem. B*, **2003**, 107, 1142.
- (48) Imahori, H.; Sakata, Y. *Adv. Mater.*, **1997**, 9, 537.
- (49) Fukuzumi, S.; Imahori, H. in *Electron Transfer in Chemistry*, ed. V. Balzani, Wiley-VCH, Weinheim, **2001**, vol. 2, pp. 270–337.
- (50) Ebersson, L. *Electron Transfer Reactions in Organic Chemistry; Reactivity and Structure*, Springer, Heidelberg, **1987**, vol. 25.
- (51) Imahori, H.; Guldi, D. M.; Tamaki, K.; Yoshida, Y.; Luo, C.; Sakataand, Y.; Fukuzumi, S. *J. Am. Chem. Soc.*, **2001**, 123, 6617.
- (52) Gouterman, M. *J. Chem. Phys.* **1959**, 30, 1139
- (53) Gouterman, M. In “The Porphyrins”; Dolphin, D., Ed.; Academic: New York, 1978; Vol. 3, p 1.
- (54) Tsuda, M.; Dy, E. S.; Kasai, H. *J. Chem. Phys.* **2005**, 122, 244719.
- (55) Jasinski, R. A. Y. M. *Nature* **1964**, 201, 1212.
- (56) Vasudevan, P.; Santosh; Mann, N.; Tyagi, S. *Transition. Met. Chem* **1990**, 15, 81.
- (57) Ricard, D.; Didier, A.; L’Her, M.; Boitrel, B. *C. R. Chimie* **2002**, 5, 33.
- (58) Zagal, J. H.; Sen, R.; Yeager, E. *J. Electroanal. Chem* 1977, 83, 207.
- (59) Shi, C; Steiger, B; Yuasa, M; Anson, F. C. *Inorg. Chem.* **1997**, 36, 4294.
- (60) Lucas, C. A.; Beck, F. *J. Appl. Electrochem.* **1977**, 7, 239.
- (61) Sun, S.; Jiandg, N.; Xia, D. *J. Phys Chem. C* **2011**, 115, 9511.
- (62) Chen, R.; Li, H.; Chu, D.; Wang, G. *J. Phys. Chem. C* **2009**, 113, 20689.
- (63) Wang, G. F.; Ramesh, N.; Hsu, A.; Chu, D.; Chen, R. *Mol. Simul.* **2008**, 34, 1051.
- (64) Zagal, J. H.; Silva, F.; Paez, M. in: Zagal, J.H.; Bedioui, F.; J.P. Dodelet (Eds.), *N<sub>4</sub>-Macrocyclic Metal Complexes*, Springer, New York, 2006, p. 41.
- (65) Zagal, J. H.; Gulppi, M.; Isaacs, M.; Cardenas-Jiron, G.; Aguirre, M. *J. Electrochim. Acta* **1998**, 44, 1349.
- (66) Cardenas-Jiron, G. I.; Gulppi, M.A.; Caro, C.A.; Del Rio, R.; Paez, M.; Zagal, J. H. *Electrochim. Acta* **2001**, 46, 3227.
- (67) Zagal, J. H.; Cardenas-Jiron, G. I. *J. Electroanal. Chem.* **2000**, 489 (1-2), 96.
- (68) Shi, Z.; Zhang, J. *J. Phys. Chem. C* **2007**, 111, 7084.

- (69) Jasinski, R. *J. Electrochem. Soc.* **1965**, *112*, 526.
- (70) Jahnke, H.; Schonborn, M.; Zimmermann, G. *Topics in Curr. Chem.* **1976**, *61*, 133.
- (71) Ma, J.; Liu, Y.; Zhang, P.; Wang, J. *Electrochem. Commun.* **2008**, *10*, 100.
- (72) Radyushkina, K. A.; Tarasevich, M. R.; Akhundov, E. A. *Elektrokhimiya* **1979**, *15*, 1884.
- (73) Meshitsuka, S.; Ichikawa, M.; Tamaru, K. *J. Chem. Soc. Chem. Commun.* **1974**, 158.
- (74) Yoshida, T.; Kamato, K.; Tsukamoto, M.; Iida, T.; Schlettwein, D.; Woehrle, D.; Kaneko, M. *J. Electroanal. Chem.* **1995**, *385*, 209.
- (75) Kushmerick, J. G. *Mater. Today* **2005**, *8* (7), 26.
- (76) Nitzan, A.; Ratner, M. A. *Science* **2003**, *300*, 1384.
- (77) Heath, J. R.; Ratner, M. A. *Phys. Today* **2003**, *56* (5), 43.
- (78) Patrone, L.; Palacin, S.; Charlier, J.; Armand, F.; Bourgoin, J. P.; Tang, H.; Gauthier, S. *Phys. Rev. Lett.* **2003**, *91*, 096802.
- (79) Yaliraki, S. N.; Kemp, M.; Ratner, M. A. *J. Am. Chem. Soc.* **1999**, *121*, 3428.
- (80) Levich, V. G. *Acta. Physicochim. URSS*, **1942**, *17*, 257.
- (81) Koutecky, J.; Levich, V. G. *Zh. Fiz. Khim.* **1958**, *32*, 1565.
- (82) Tafel, J. Z. *Physik. Chem.* **1905**, *50A*, 641.

## Chapter 2

# Layer-by-layer assembly of functional molecular layers on a metal surface

---

### 2.1 Introduction

Chemically modified electrodes can provide opportunities to investigate the relation between surface structures and functionality at the atomic or molecular scale. In particular, when chemical layers are formed by stacking of molecular components, their integrated structure is expected to be changed systematically by alternating the combination of molecular components. Functional molecules utilized for surface modification usually consist of an anchor head group, a wire body, and a functional terminal group. If such functional molecules are pre-synthesized and used to form molecular layers self-assembly, the packing or ordering of the chemical layers formed may not be well-controlled because of the bulky functional groups. In the case of the layer-by-layer assembly, the functional components and wire components are separately stacked on the surface, resulting that the connection between the substrate and functional groups can be well controlled. Consequently, distance and electronic connection between the metal surface and functional groups can be well tuned by changing the structure or physical properties of wire molecules. This chapter deals with a general procedure for layer-by-layer assembly of functional molecular layers on a metal electrode. The formed layers are characterized using electrochemical and spectroscopic means. As a model functional group, we focus on transition metal macrocyclic complexes such as metalloporphyrins and metallophthalocyanines because of their multi-functionality. Molecular wires with various lengths and structures are utilized to tune the electronic coupling between Au and the complexes. For the anchor group of the wire molecules, thiol and isocyanide groups are mainly studied, which can bind to metal surfaces strongly. The connection between wire molecules and macrocyclic complexes is formed by axial ligation of the central metal ions to terminal groups of the wire molecules. Moreover, the adsorption geometry of anchor groups is controlled by surface modification of Au electrode with monoatomic foreign metal overlayers.

## 2.2 Experimental

### 2.2.1 Layer-by-layer fabrication of chemically modified electrodes

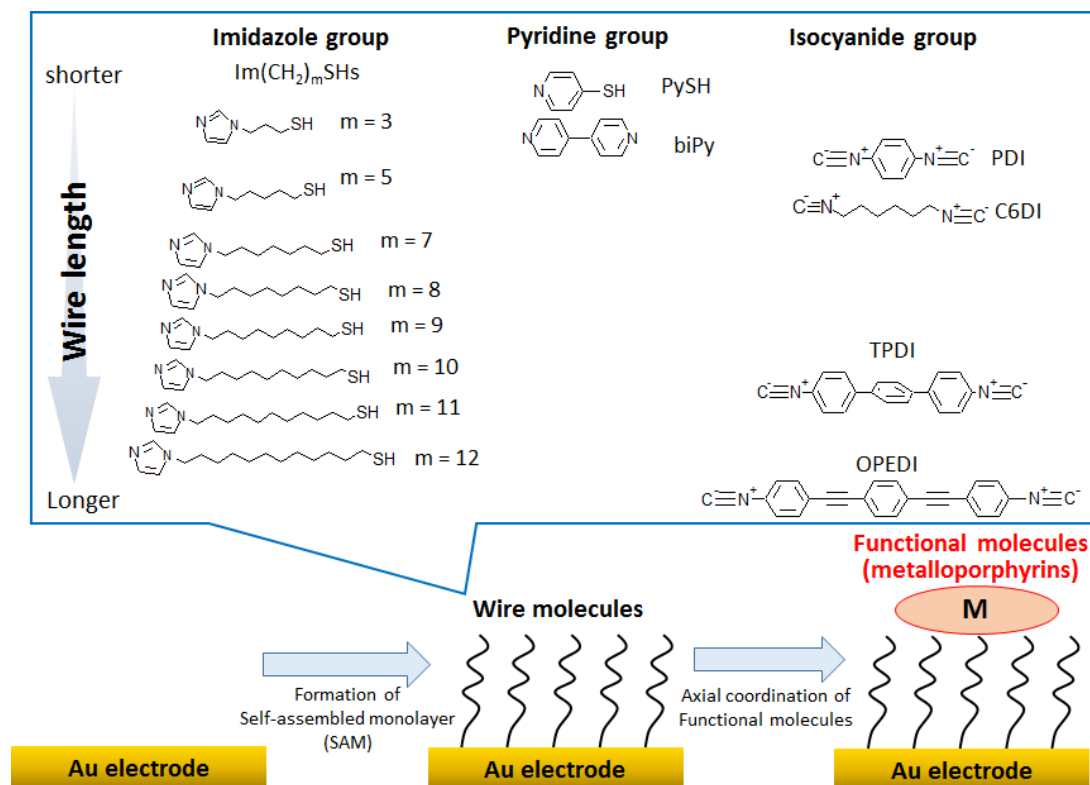


Figure 2.2.1. Schematic illustration of layer-by-layer stepwise assembly of catalytic chemical layers on a gold electrode. The catalytic local surface sites are created using metal-macrocylic complexes, which are adsorbed on top of SAMs of wire molecules. The electronic connection between the catalytic sites and electrode can be varied by alternating the wire molecule.

Figure 2.2.1 shows a procedure for layer-by-layer assembly of chemical layers on a gold electrode. A polycrystalline Au disk with diameter of 10 mm and purity of 99.999% was utilized as the electrode. The electrode surface was mirror-finished by mechanical polishing and annealing so that the roughness factor of the surface was less than 1.2. The prepared Au disk was further cleaned using piranha solution and hydrogen flame annealing before use. Then, monolayers of wire molecules were self-assembly fabricated on the surface. The upper panel of Fig. 2.2.1 shows a series of wire molecules utilized in this work: imidazole tagged alkanethiols ( $\text{ImC}_m\text{SH}$ ,  $m = 3, 5, 7, 8, 9, 10, 11, 12$ ), 4-pyridinethiols ( $\text{PySH}$ ), 4,4'-bipyridine ( $\text{biPy}$ ), hexane diisocyanide ( $\text{C}_6\text{DI}$ ), 1,4-phenylene diisocyanide ( $\text{PDI}$ ), 4,4'-terphenyl diisocyanide ( $\text{TPDI}$ ), and 1,4-bis[2-(4-isocyanophenyl)ethynyl]benzene ( $\text{OPEDI}$ ). The series of  $\text{ImC}_m\text{SH}$  was purchased from ProChimia Surfaces sp z o.o.  $\text{PySH}$ ,  $\text{biPy}$ ,  $\text{PDI}$ , and  $\text{C}_6\text{DI}$  were purchased from Aldrich.  $\text{TPDI}$  and  $\text{OPEDI}$  were synthesized by reported methods<sup>1,2</sup> with slight modification. These

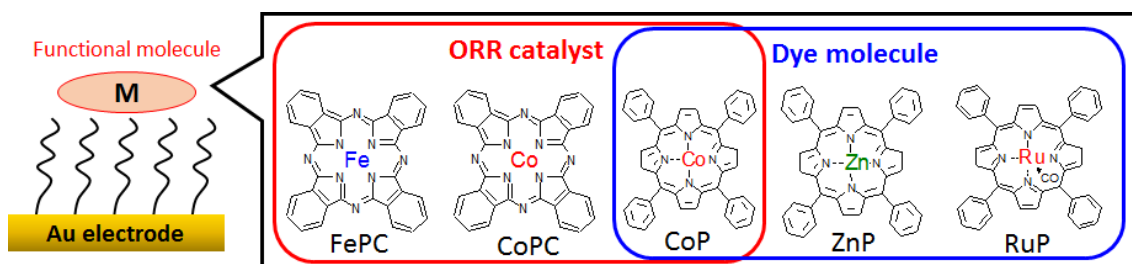


Figure 2.2.2. Structures of the functional molecule; FePC, CoPC, CoP, ZnP, RuP, formed on the various wire molecules.

chemicals were utilized as received without further purification. Since these molecules have an anchor group such as thiol or isocyanide, well-organized self-assembled monolayers (SAMs) of these molecules can be formed on the electrode.<sup>3-7</sup> The formation conditions of the monolayers are summarized in Table 1. For diisocyanide molecules, all solutions and SAMs were prepared inside a glovebox filled with Ar in order to avoid oxidation of the anchor group. The lengths of the wire molecules were estimated using Hartree-Fock calculations with 6-31G\* basis sets (Gaussian 09, revision A02). These wire molecules have a terminal group such as imidazole or pyridine, and hence, metallomacrocycles can be attached on top of the SAMs through axial coordination of the central metal ion with the terminal group.<sup>8-12</sup> For the adsorption geometry of the isocyanide anchor, the density functional theory (DFT) was performed under B3PW91 level with LanL2DZ for Au or Pd atoms and with 6-31g\*\* for PDI molecule.

Figure 2.2.2 shows metallomacrocycles utilized as model functional molecules in this work; cobalt(II)-tetraphenylporphyrin (CoP), zinc(II)-tetraphenylporphyrin (ZnP), ruthenium(II)-tetraphenylporphyrin carbonyl (RuP), iron(II)-phthalocyanine (FePC) and cobalt(II) phthalocyanine (CoPC). CoP, CoPC, and FePC are utilized as ORR catalysts, and CoP, ZnP, and RuP are utilized as photoreaction centers. These molecules were purchased from Aldrich and Alfa Aesar, and were utilized as received. To immobilize these molecules on top of the SAMs, the SAM-covered Au disk was immersed into solution containing each molecules. The formation conditions of the functional layer are summarized in Table 2.

Table 1. Formation conditions of SAMs of various wire molecules.

Wire molecule	Conc. (mM)	Solvent	Temp. (°C)	Immersion time
ImC <sub>3</sub> SH	1	Ethanol	25	1 day
ImC <sub>5</sub> SH	1	Ethanol	25	1 day
ImC <sub>7</sub> SH	1	Ethanol	25	1 day
ImC <sub>8</sub> SH	1	Ethanol	40	1 day
ImC <sub>9</sub> SH	1	Ethanol	40	1 day
ImC <sub>10</sub> SH	1	Ethanol	25	1 day
ImC <sub>11</sub> SH	1	Ethanol	25	2 days
ImC <sub>12</sub> SH	1	Ethanol	40	1 day
PySH	1	Ethanol	25	6 hours
BiPy	1	Ethanol	25	6 hours
PDI	10	THF	25	6 hours
TPDI	1	Dichloromethane	25	1 day
OPEDI	1	Dichloromethane	25	1 day
C <sub>6</sub> DI	1	Methanol	25	6 hours

Table 2. Formation conditions of catalyst layers on SAM-covered Au.

Catalyst	Conc. (mM)	Solvent	Temp. (°C)	Immersion time
CoP	0.1	Chloroform	25	3 days
CoPC	0.1	Chloroform	25	3 days
FePC	0.1	Chloroform	25	1 day
RuP	0.1	Toluene	25	3 days
ZnP	0.1	Chloroform	25	1 day

A Pd monolayer-modified Au electrode was also utilized as a substrate for chemical functional layers to tune the substrate-anchor interactions. The Pd monoatomic layer (Pd<sub>ML</sub>) was prepared on Au electrodes by using the underpotential deposition (UPD) method.<sup>13,14</sup> The Au disk was firstly cleaned using piranha solution and hydrogen flame annealing. Then, the disk was immediately transferred to an electrochemical cell containing 0.1 M H<sub>2</sub>SO<sub>4</sub> aqueous solution with 1 mM PdCl<sub>2</sub> and 2 mM HCl under application of the electrochemical potential of +0.85 V vs. Ag/AgCl. Next, Pd was deposited on the Au surface by potential sweep from +0.85 V to +0.60 V with the scan rate of 1 mV·sec<sup>-1</sup>. To improve the quality of the Pd<sub>ML</sub>, the potential was kept at +0.6 V for 10 minutes, and then the disk electrode was removed from the solution, followed by careful rinse with Milli-Q water. The obtained Pd<sub>ML</sub>-covered Au electrode (Pd<sub>ML</sub>/Au) was immediately immersed into the solution containing wire molecules such as PDI, TPDI, OPEDI and C<sub>6</sub>DI. The formation conditions of the wire monolayers and functional monolayers are same as those for the Au surfaces.

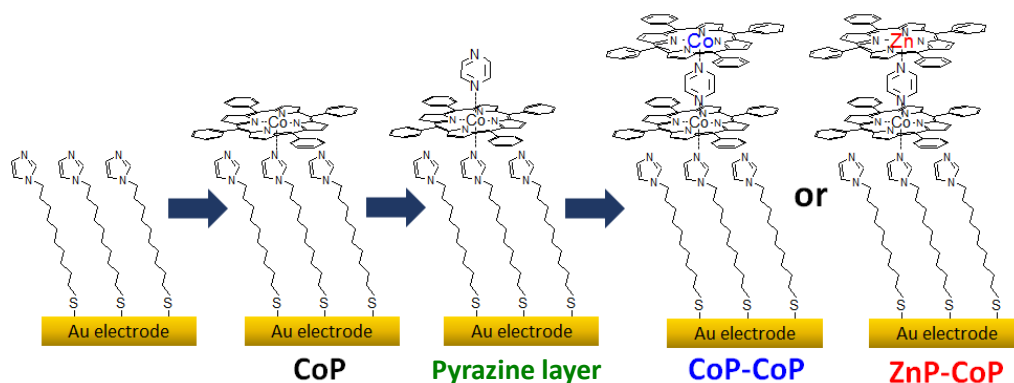


Figure 2.2.3. Schematic illustration of layer-by-layer stepwise assembly of CoP-CoP and ZnP-CoP bilayers on Au electrodes.

As for the photoelectrochemical study, metalloporphyrin bilayers were also prepared by the layer-by-layer formation process, as shown in Figure 2.2.3. ImC<sub>11</sub>SH molecules were utilized to interconnect the Au electrode and the metalloporphyrin bilayers. The formation process of the first layer of CoP, which was directly attached to ImC<sub>11</sub>SH-SAM, was same as the process shown in Figure 2.2.1. Then, additional attachment of pyrazine molecules onto the immobilized CoP was conducted by immersion into toluene solution containing 10 mM pyrazine for 1 day at 25 °C. The second layer of metalloporphyrins was finally stacked on the pyrazine layer by incubating the modified electrode in the solution with porphyrin molecules for 1 day at 25 °C. When CoP molecules were attached as the second layer, CoP-CoP homo-bilayers were formed. When ZnP molecules were utilized for the second layer, ZnP-CoP hetero-bilayers were prepared on the electrode surface.

## 2.2.2 Characterization methods of the fabricated molecular layers

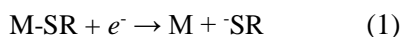
For the series of wire molecules with the thiol anchor group, the surface coverages of SAMs were measured using linear sweep voltammograms (LSVs) for reductive desorption of the thiol anchor groups in 0.1 M KOH aqueous at the scan rate of 20 mV·s<sup>-1</sup>; the amount of molecules adsorbed on the electrode can be determined from the Faradic charge of the thiol-reduction reaction. For the other wire molecules, the quantitative estimation of the surface coverage was not conducted because of the lack of redox active moieties. Instead, the quality of the formed SAMs was examined by checking whether the electrodes were electrochemically inert in a redox solution. For the isocyanide molecules, the structure of the substrate-anchor junctions was examined using Polarization Modulation Infrared Reflection Adsorption

Spectroscopy (PM-IRRAS). PM-IRRAS measurements were performed using a fourier-transform-infrared-spectrometer (iS50R, Thermo Fisher Scientific) with a PM-IRRAS module. The IR signals were collected at the incident angle of 85° with accumulation of 1024 scans in the range of 4000-400 cm<sup>-1</sup> at a resolution of 4 cm<sup>-1</sup>. The baseline of the spectra was corrected using the spectra for the bare metal substrate.

The surface density of metalloporphyrin molecules formed on SAM-covered electrodes was estimated from the electrochemical response of metal ion centers in a 0.1 M HClO<sub>4</sub> aqueous solution, measured by CVs with a scan rate of 50 mV·s<sup>-1</sup>. All of the electrochemical measurements were performed using a potentiostat (Hokuto Denko, HSV-110) in a standard three-electrode electrochemical cell with a platinum wire counter electrode and a Ag/AgCl (saturated KCl) reference electrode. All electrolyte solution in the cell was deaerated by bubbling of ultrapure Ar gas (99.999 %) for 30 minutes.

### 2.3 SAMs of wire molecules formed on an Au electrode

For the thiol molecules, the optimum preparation conditions of SAMs were determined by measuring reductive desorption charge of thiol-SAMs in 0.1 M KOH aqueous solution. It is known that the self-assembly of alkane-thiols is achieved by chemical bond formation between the substrate atoms and sulfur atoms of the thiols. Since Widrig et al. reported that alkanethiol-SAMs are desorbed from the metal-surface (M) by the following one electron reduction process in an alkaline aqueous solution.<sup>15</sup>



Many researchers have utilized electrochemical reaction (1) to characterize SAMs because the appearance of the cathodic peak, e.g., the peak shape, position, and area, provide useful information regarding the quality of the SAMs such as the amount of adsorbed molecules, uniformity, and adsorption energy. For example, it was found that the reductive peak potential became more negative when the alkyl chain was longer, reflecting the stronger van der Waals attractive interaction among alkyl chains.<sup>16</sup>

Figure 2.3.1a shows typical linear-sweep voltammograms for the desorption of the series of ImC<sub>m</sub>SH-SAM with different chain lengths (m = 3, 5, 9, 11). The reductive peak potentials were indeed gradually shifted to the negative direction with increasing carbon numbers (m) of the alkyl chains. The estimated surface densities of ImC<sub>m</sub>SH-SAMs are shown in Figure 2.3.1b. The surface density was slightly dependent on the chain length; it increased gradually with increasing the number of carbons, suggesting that the quality of SAMs became better. The surface densities for these molecules were smaller than the ideal value expected for the saturated coverage of alkanethiol-SAMs with a ( $\sqrt{3} \times \sqrt{3}$ ) R30° structure on Au(111) surface,  $7.6 \times 10^{-10} \text{ mol}\cdot\text{cm}^{-2}$ .

<sup>17-19</sup> This is reasonable because the present molecules have a bulky terminal group, and the Au substrate utilized was polycrystalline. Thus, it is expected that well-ordered SAMs were formed on the surface.

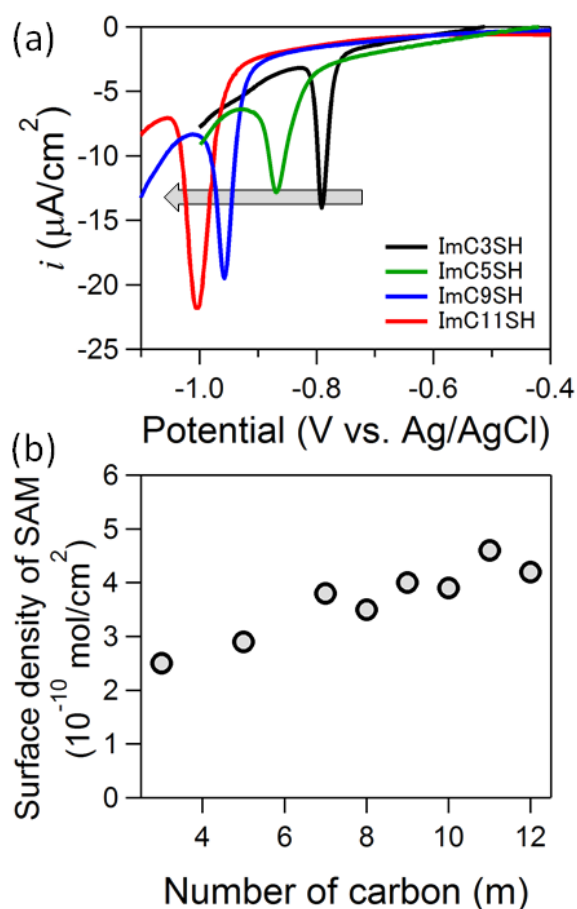


Figure 2.3.1. (a) Typical linear-sweep voltammograms for reductive desorption of ImC<sub>m</sub>SH-SAM (m = 3, 5, 9, 11) measured in 0.1 M KOH aqueous solution. Scan rate is 20 mV·s<sup>-1</sup>. (b) Carbon number dependence of surface density of ImC<sub>m</sub>SH-SAM (m = 3, 5, 7-12).

The formation of SAMs of the diisocyanide molecules were examined using PM-IRRAS. IR spectroscopy is a useful tool for analyzing substrate-isocyanide bonding because isocyanide molecules have the strong CN stretching mode ( $\nu\text{CN}$ ) and its frequency is sensitive to the interaction to the substrate. For diisocyanide molecules, two types of isocyanide bands are often observed on gold surfaces. One of the bands is attributed to the vibration of free CN ( $\nu\text{CN}_{\text{free}}$ ). The other with higher frequency is associated with the vibration of CN bound to Au surface ( $\nu\text{CN}_{\text{Au}}$ ). The blue shift of  $\nu\text{CN}_{\text{Au}}$  is explained by the contribution of  $\sigma$ -donation from CN to Au.

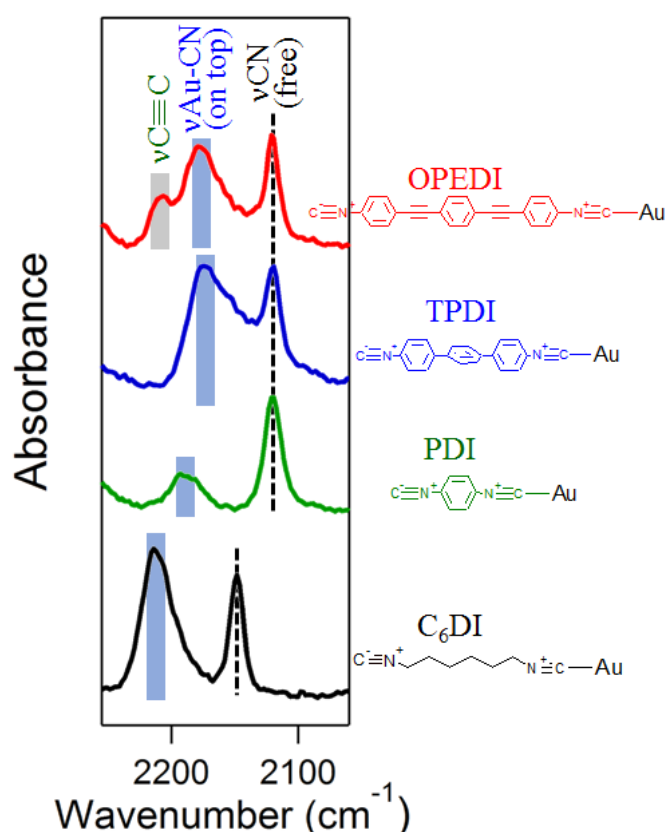


Figure 2.3.2. PM-IRRAS spectra of diisocyanide-SAMs formed on Au. The spectra were measured with a resolution of  $4\text{ cm}^{-1}$  and 1024-integration.

In Figure 2.3.2, the two peaks of  $\nu\text{CN}$  and  $\nu\text{CN}_{\text{Au}}$  were observed for all of these molecules when the preparation condition was optimized.<sup>1,20,21</sup> The frequency difference in  $\nu\text{CN}_{\text{free}}$  between  $\text{C}_6\text{DI}$  and the other diisocyanides is due to the electronic difference between the saturate alkane chain and  $\pi$ -conjugated chains next to the CN. The appearance of  $\nu\text{CN}_{\text{free}}$  indicates that these diisocyanide molecules stand up on the surface with edge-on configuration, which is essential to form the stacked functional layers. In particular,  $\text{C}_6\text{DI}$  tends to adsorb on Au with lying-down configuration using both ends. Moreover, this molecule easily form multilayers.<sup>21</sup> Therefore, the formation condition was carefully controlled especially for this molecule.

## 2.4 Control of metal-molecule junctions using monoatomic metal overlayers

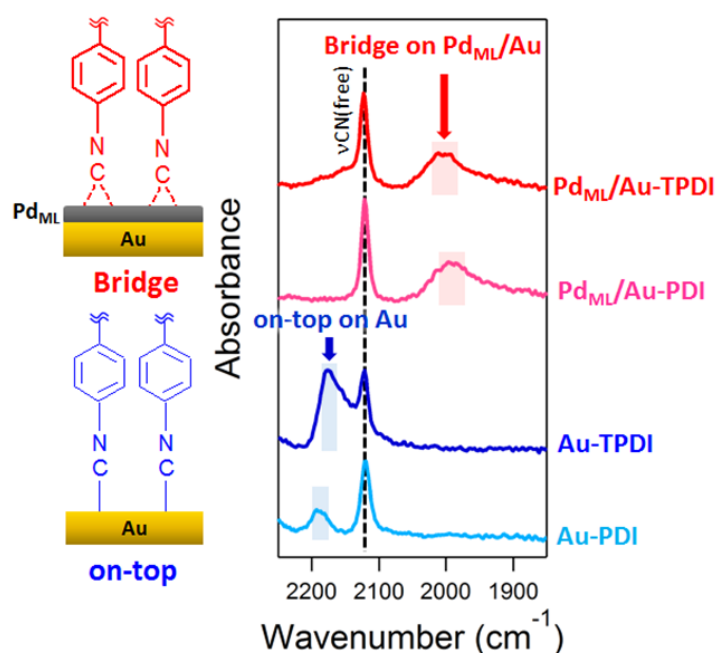


Figure 2.4.1. PM-IRRAS spectra of PDI-SAMs and TPDI-SAMs formed on Au and Pd<sub>ML</sub>/Au. The spectra were measured with a resolution of 4 cm<sup>-1</sup> and 1024-integration

The metal-molecule interface junction was changed by forming Pd monoatomic layer (Pd<sub>ML</sub>) on Au surfaces. It is known that thiols can bind more strongly to Au surfaces than to platinum group metal (PGM) surfaces. On the other hand, isocyanides can bind more strongly to PGM surfaces such as the Pd layer than to Au surfaces. The adsorption geometry of isocyanides was compared on Au and Pd<sub>ML</sub> using PM-IRRAS, as shown in Figure 2.4.1. As already showed in Figure 2.3.2, PDI and TPDI on Au exhibited  $\nu\text{CN}_{\text{free}}$  and  $\nu\text{CN}_{\text{Au}}$ .<sup>1,20,21</sup> According to the peak position of  $\nu\text{CN}_{\text{Au}}$ , the adsorption geometry of these molecules was assigned to the on-top configuration. On the Pd<sub>ML</sub>/Au surface,  $\nu\text{CN}_{\text{Au}}$  for the on-top configuration disappeared and a new peak appeared with lower frequency. This new peak can be assigned to the bridge configuration of the CN. The bridge configuration is formed through  $\pi$  back-donation from the metal surface to isocyanides as well as  $\sigma$ -donation from isocyanides to the surface. Therefore, the population of ligand orbitals are antibonding with respect to the CN bond, resulting in a subsequent decrease in CN stretching frequencies.

Figure 2.4.2 shows theoretically optimized structures of PDI molecule adsorbed on Au<sub>4</sub> and Pd<sub>3</sub> clusters and their IR spectra, obtained by DFT calculations. The stable adsorption geometry of PDI was obtained as the on-top configuration on Au, and the bridge and three-fold hollow

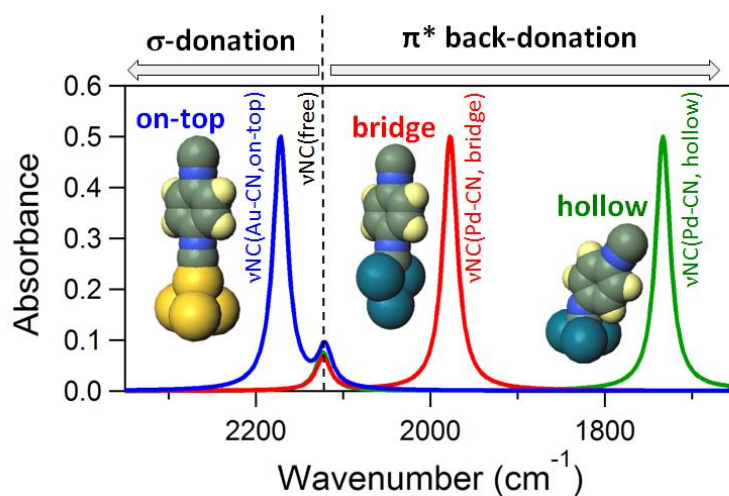


Figure 2.4.2. Optimized structures of PDI molecule adsorbed on Au<sub>4</sub> and Pd<sub>3</sub> clusters and their IR spectra, obtained by DFT calculations.

configurations on Pd atoms. IR spectra for on-top on Au cluster and bridge on Pd cluster were in good agreement with the experimentally measured IR spectra. On the other hand, the vNC-Pd (hollow) mode was not observed experimentally. Note that the on-top and bridge adsorptions have the linear molecular geometry while the hollow adsorption is bent. Therefore, one can assume that the thickness of PDI-SAMs is similar between on-top and bridge configurations.

## 2.5 Surface density of metalloporphyrins adsorbed on SAM-covered electrodes

### 2.5.1 Metalloporphyrin monolayer

#### 2.5.1.1. CoP monolayers

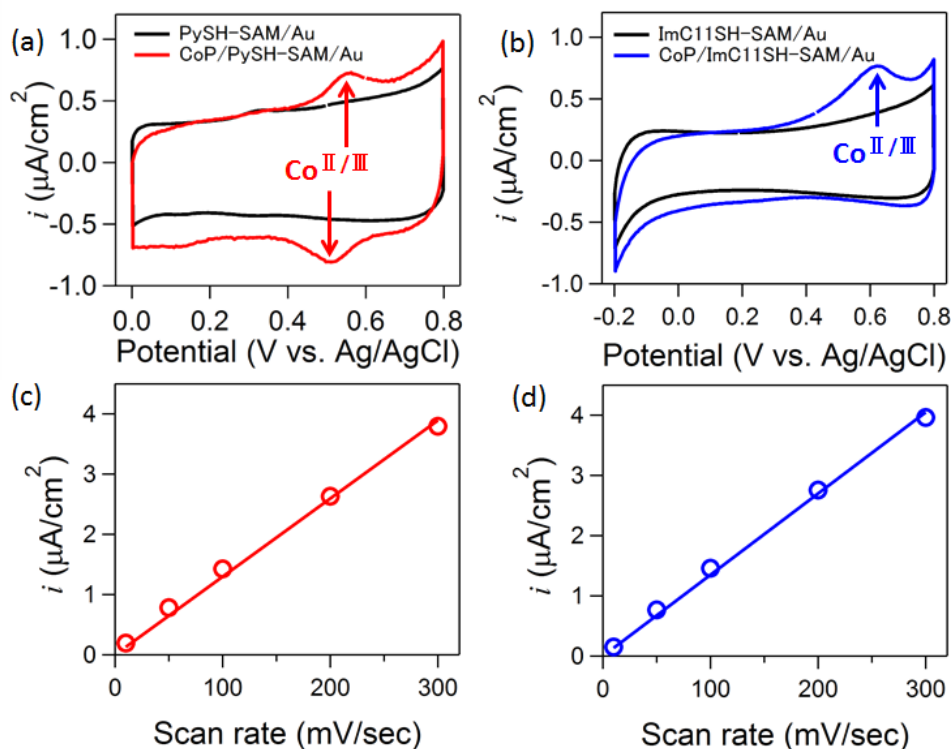


Figure 2.5.1. CVs for (a) PySH-SAM/Au (black line) and CoP/PySH-SAM/Au (red line), and (b) ImC<sub>11</sub>SH-SAM/Au (black line) and CoP/ImC<sub>11</sub>SH-SAM/Au (blue line), measured in 0.1 M HClO<sub>4</sub> solution at the scan rate of 50 mV·s<sup>-1</sup>. Plots of oxidation peak current density as a function of the sweep rate of the electrochemical potential for (c) CoP/PySH-SAM/Au and (d) CoP/ImC<sub>11</sub>SH-SAM/Au.

Figures 2.5.1a and b show CVs for PySH-SAM/Au with and without CoP and ImC<sub>11</sub>SH-SAM/Au with and without CoP, respectively, measured in 0.1 M HClO<sub>4</sub> solution at the sweep rate of 50 mV·s<sup>-1</sup>. The CV of CoP /PySH-SAM/Au clearly showed oxidation and reduction peaks of the central Co ions. As for the CV of CoP/ImC<sub>11</sub>SH-SAM/Au, however, only the oxidation peak was clearly observed because of the very slow charge transfer from CoP anions to the electrode. According to the Faradic charge of the oxidation peak, the surface density of CoP was estimated to be ca.  $6.5 \times 10^{-12}$  mol·cm<sup>-2</sup> on the PySH-SAM/Au and  $7.5 \times 10^{-12}$  mol·cm<sup>-2</sup> on the ImC<sub>11</sub>SH-SAM/Au. Figures 2.5.1c and d show plots of the oxidation peak current density of CoP/PySH-SAM/Au and CoP/ImC<sub>11</sub>SH-SAM/Au, respectively, as a function of the scan rate of the electrochemical potential. The linear relations of the plots indicate that the redox responses were indeed originated from CoP molecules adsorbed on the electrode surface. Figure

2.5.2 shows the surface density of CoP on PySH-SAM/Au as a function of the immersion time for the CoP adsorption on the electrodes. The density of CoP increased with time and saturated after three days. In the present work, the saturation condition for CoP adsorption was chosen to form the CoP layer, in order to minimize the difference in the amount of CoP adsorption among the samples. Consequently, the density of CoP was highly reproducible for the same wire molecule. On the other hand, the difference in the density of CoP among the wire molecules was not so small, as shown in Figure 2.5.3. In Chapters 3 and 4, this contribution was carefully evaluated to discuss experimental results quantitatively.

Figure 2.5.4 shows the oxidation peak potential of Co centers as a function of the number of methylene in the alkyl chain. In the long alkyl chain region with  $m > 8$ , so-called odd-even effect was clearly seen. On the other hand, in the short alkyl chain region with  $m \leq 8$ , the peak potential shifted negatively with decreasing the number of methylene group. The odd-even effect observed in the long alkyl chain region can be explained by the analogy with the

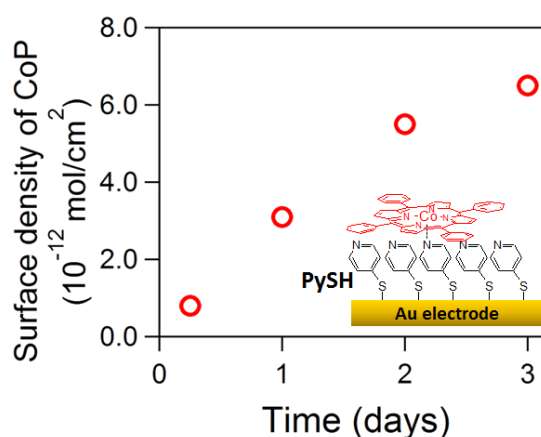


Figure 2.5.2. Surface density of CoP on PySH-SAM/Au as a function of the immersion time into chloroform solution containing 0.1 mM CoP.

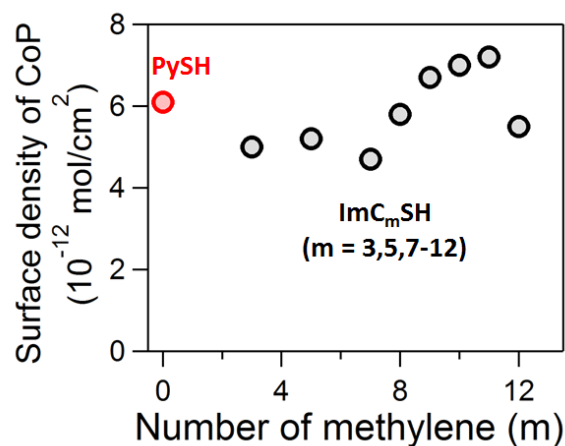


Figure 2.5.3. Estimated surface density of CoP on various wire molecules as a function of the number of methylene.

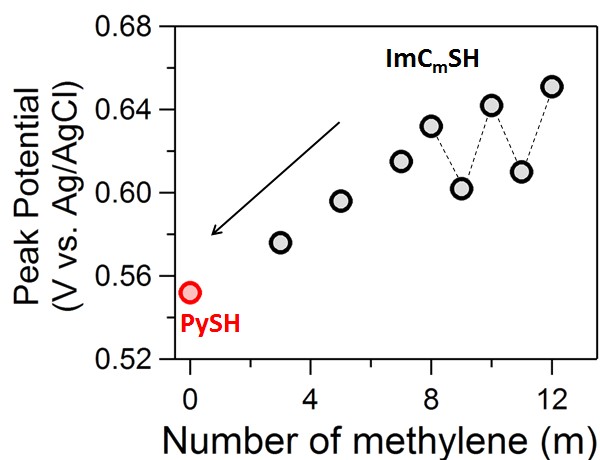


Figure 2.5.4. Oxidation peak potential of Co(II/III) as a function of the number of methylene from each CVs.

previously reported odd-even effect for alkanethiol SAMs; the terminal methyl orientation is known to be dependent on the even-and-odd number of methylene groups<sup>23,24</sup>. In the present case, the terminal imidazole orientation is expected to show similar behavior, leading to the odd-even steric effect on the strength of the coordination bonding with CoP. This difference should affect the electron density on the Co center, resulting in the shift of the redox potential of the Co center. For the significant shift observed in the short alkyl chain region, the contribution of the electronic interactions between the substrate metal and CoP is presumably dominant, which will be discussed in details in Chapter 3.

### 2.5.1.2. RuP monolayers

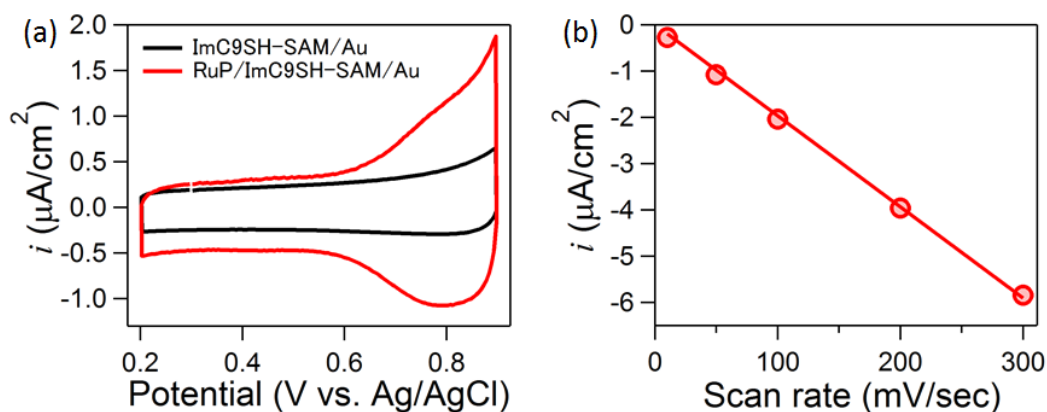


Figure 2.5.5. (a) CVs for ImC<sub>9</sub>SH-SAM/Au (black line) and RuP/ImC<sub>9</sub>SH-SAM/Au (red line), measured in 0.1 M HClO<sub>4</sub> solution at the scan rate of 50 mV·s<sup>-1</sup>. (b) Reduction peak current density of RuP/ImC<sub>9</sub>SH-SAM/Au as a function of the scan rate of the electrochemical potential.

RuP adlayers were formed on the SAM-covered Au disk using axial coordination of the central Ru ion of RuP with the terminal imidazole of ImC<sub>m</sub>SH (m = 7, 8, 9, 10, 11, 12, 17). RuP-modified electrodes were utilized for photoelectrochemical measurements presented in Chapter 4. Figure 2.5.5a shows CVs for ImC<sub>9</sub>SH-SAM/Au and RuP/ImC<sub>9</sub>SH-SAM/Au, measured in 0.1 M HClO<sub>4</sub> solution at the sweep rate of 50 mV·s<sup>-1</sup>. Both oxidation and reduction reactions of the central Ru ions was seen in the CVs, although the oxidation peak was not clearly obtained. According to the Faradic charge of the reduction peak, the surface density of RuP was estimated to be ca. 2.5 × 10<sup>-11</sup> mol·cm<sup>-2</sup>, which was larger than that of CoP. This difference is probably related to the difference in the adsorption energy of metalloporphyrins to the imidazole group. Figure 2.5.5b shows the reduction peak current density of RuP/ImC<sub>9</sub>SH-SAM/Au as a function

of the scan rate of the electrochemical potential. The linear relation indicates that the redox response observed was indeed originated from RuP molecules adsorbed on the electrode surface.

Figure 2.5.6 shows the surface density of RuP as a function of the number of methylene groups in the alkyl chain. The estimated value was nearly independent of the wire length except for the ImC<sub>17</sub>SH. In Chapter 4, these values were utilized to calculate the internal quantum efficiency (IQE) in photo-induced charge transfer reactions.

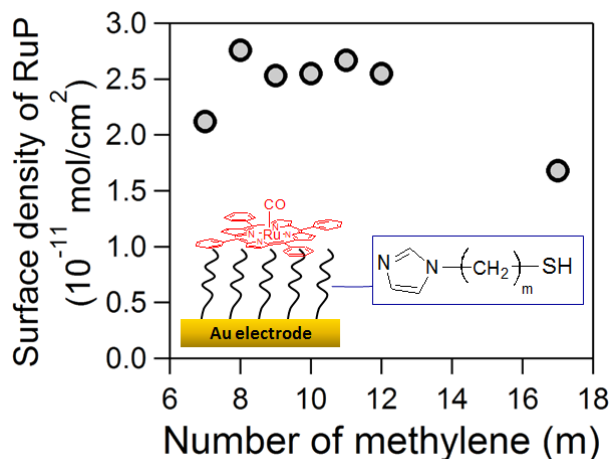


Figure 2.5.6. Estimated surface density of RuP on ImC<sub>m</sub>SH-SAM as a function of the number of methylene groups.

## 2.5.2 Metalloporphyrin bilayer

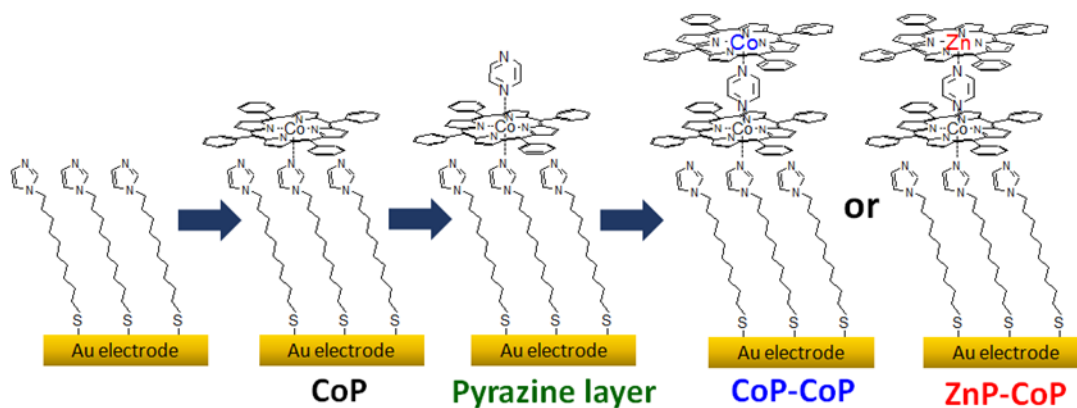


Figure 2.5.7. Schematic illustration of layer-by-layer stepwise assembly of CoP-CoP and ZnP-CoP bilayers on Au electrodes.

The advantage of the layer-by-layer method for preparing porphyrin bilayers is that both the electrode-porphyrin distance and porphyrin-porphyrin distance can be well controlled by the thickness of the imidazole-terminated monolayer and the size of the spacer molecule in the dimer, respectively. The formation of the stacked bilayers of metalloporphyrins has already been well established.<sup>8,25,26</sup> Here, pyrazine molecules were utilized as a spacer.

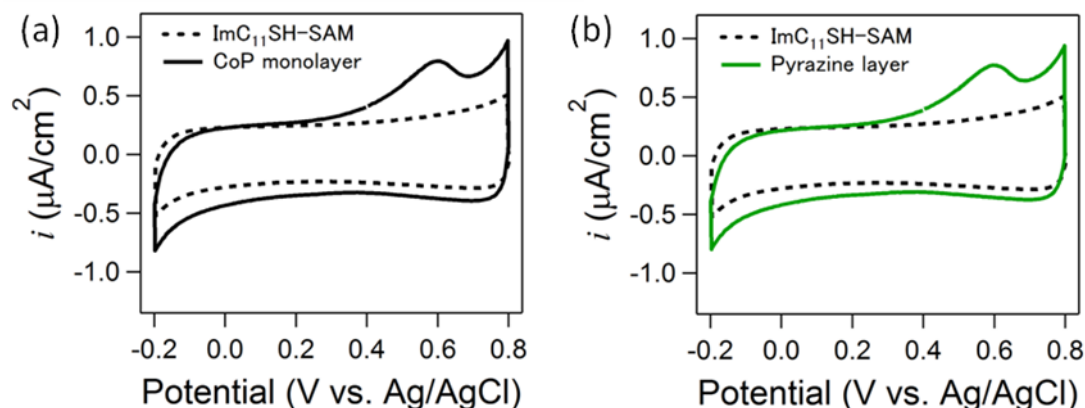


Figure 2.5.8. (a) CVs for ImC<sub>11</sub>SH-SAM (dotted line) and CoP monolayer (solid line), measured in 0.1 M HClO<sub>4</sub> solution at the scan rate of 50 mV·s<sup>-1</sup>. (b) CVs for ImC<sub>11</sub>SH-SAM (dotted line) and Pyrazine layer (green line), measured in the same electrochemical condition.

Figures 2.5.8a and b show CVs of CoP monolayer with and without pyrazine adsorption, respectively. Hereinafter, the sample with pyrazine molecules is referred to as Pyrazine layer. Clearly, the adsorption of pyrazine molecules did not affect the redox response of CoP monolayers. This indicates that the electronic structure of CoP is similar between penta-coordination without pyrazine adsorption and hexa-coordination with pyrazine adsorption.

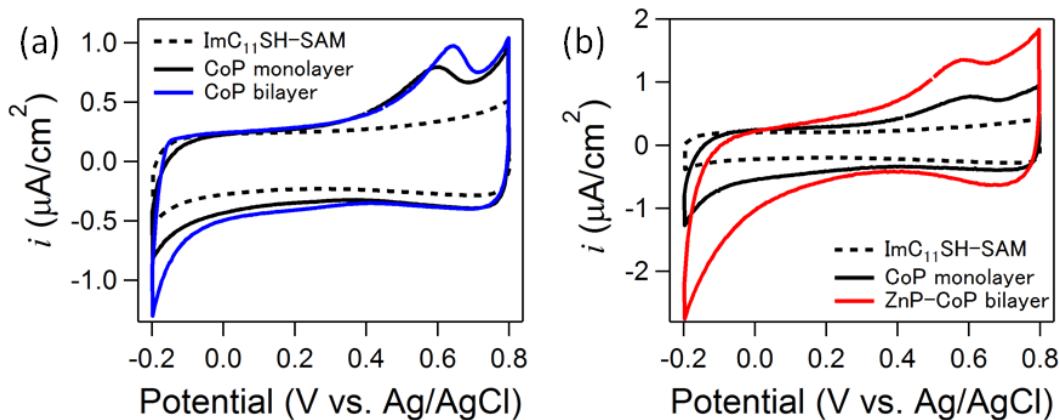


Figure 2.5.9. (a) CVs for CoP monolayer, CoP-CoP bilayer, ImC<sub>11</sub>SH-SAM. (b) CVs for CoP monolayer, ZnP-CoP bilayer, and ImC<sub>11</sub>SH-SAM

Figure 2.5.9a shows CVs for CoP monolayers and CoP-CoP bilayers. The charge of the oxidation peak for the CoP-CoP bilayers became larger than that for the CoP monolayers, indicating that the amount of the adsorbed CoP increased in the bilayers. Moreover, the peak potential of the CoP-CoP bilayers is shifted positively, indicating that the CoP-CoP dimers were indeed formed; the divalent cation formation of the CoP dimers is expected to be energetically difficult than the monovalent cation formation of the CoP monomer. The surface density of metalloporphyrin was estimated to be  $7.5 \times 10^{-12}$  mol·cm<sup>-2</sup> for CoP and  $11.5 \times 10^{-12}$  mol·cm<sup>-2</sup> for

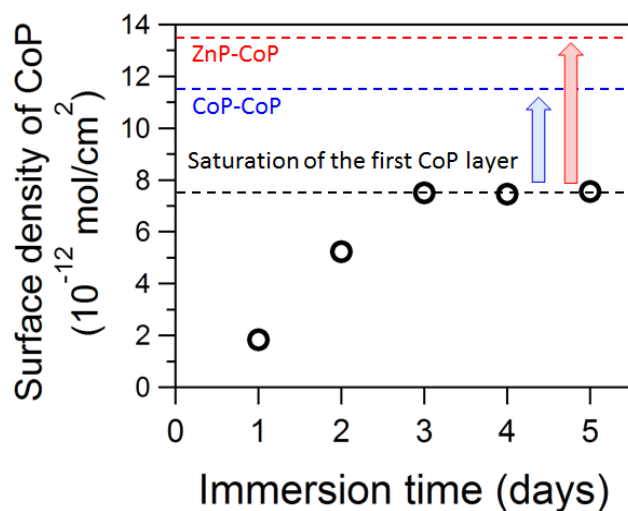


Figure 2.5.10. Surface density of CoP on ImC<sub>11</sub>SH-SAMs as a function of the immersion time of the SAM-modified electrode in 0.1 mM CoP/chloroform. The surface densities of metalloporphyrins in CoP-CoP and ZnP-CoP bilayers are also shown in the plot.

CoP-CoP; the total amount of CoP in the bilayers was 1.5 times larger than that in CoP monolayer. Therefore, the stacked dimerization of CoP occurred on the half of CoPs in the first layers. The CV for ZnP-CoP bilayer is presented in Figure 2.5.9b. An increase of the oxidation charge was observed in the ZnP-CoP bilayer, and the total amount of metalloporphyrins in ZnP-CoP bilayers was 1.8 times larger than that in the CoP monolayer. Another evidence of the bilayer formation is presented in Figure 2.5.10. The amount of CoP molecules in the first adlayers saturated after three days. The value in the first-layer saturation was exceeded only when the bilayers were formed using the spacer molecules of pyrazine.

## References

- (1) Sawaguchi, T.; Mizutani, F.; Yoshimoto, S.; Taniguchi, I. *Electrochim. Acta* **2000**, *45*, 2861.
- (2) Mayer, D.; Dretschkow, Th.; Ataka, K.; Wandlowski, Th. *J. Electroanal. Chem.* **2002**, *524-525*, 20.
- (3) Chidsey, C. E. D.; Liu, G.-Y.; Rowntree, P.; Scoles, G. *J. Chem. Phys.* **1989**, *91*, 4421.
- (4) Camillone, III, N.; Chidsey, C. E. D.; Liu, G.-Y.; Scoles, G. *J. Chem. Phys.* **1993**, *98*, 4234.
- (5) Poirier, G. E.; Tarlov, M. J. *Langmuir* **1988**, *4*, 546.
- (6) Angelici, R. J.; Lazar, M. *Inorg. Chem.* **2008**, *47*, 9155.
- (7) Murphy, K. L.; Tysoe, W. T.; Bennett, D. W. *Langmuir* **2004**, *20*, 1732.
- (8) Jagtap, S.; Kaji, Y.; Fukuoka, A.; Hara, K. *Chem. Commun.* **2014**, *50*, 5046.
- (9) Swanson, S. A.; McClain, R.; Lovejoy, K. S.; Alamdari, N. B.; Hamilton, J. S.; Scott, J. C. *Langmuir* **2005**, *21*, 5034.
- (10) Lin, S.; McCarly, R. L. *Langmuir* **1999**, *15*, 151.
- (11) El-Aziz, A. M.; Kibler, L. A. *J. Electroanal. Chem.* **2002**, *534*, 107.
- (12) Kakiuchi, T.; Usui, H.; Hobara, D.; Yamamoto, M. *Langmuir* **2002**, *18*, 5231.
- (13) Nakahara, H.; Ye, S.; Uosaki, K. *J. Phys. Chem. B* **1998**, *102*, 4366.
- (14) Kibler, L.A.; Kleinert, M.; Randler, R.; Kolb, D. M. *Surf. Sci.* **1999**, *443*, 19.
- (15) Widrig, C. A.; Chung, C.; Porter, M. D. *J. Electroanal. Chem.* **1991**, *310*, 335.
- (16) Hatchett, D. W.; Stevenson, K. J.; Lacy, W. B.; Harris, J. M.; White, H. S. *J. Am. Chem. Soc.* **1997**, *119*, 6596.
- (17) Strong, L.; Whitesides, G. M. *Langmuir* **1988**, *4*, 546-558.
- (18) Chidsey, C. E. D.; Loiacono, D. N. *Langmuir* **1990**, *6*, 682-691.
- (19) Widrig, C. A.; Alves, C. A.; Porter, M. D. *J. Am. Chem. Soc.* **1991**, *113*, 2805.
- (20) Henderson, J. I.; Feng, S.; Bein, T.; Kubiak, C. P. *Langmuir* **2000**, *16*, 6183.
- (21) Ikeda, K.; Fujimoto, N.; Uehara, H.; Uosaki, K. *Chem. Phys. Lett.* **2008**, *460*, 205.
- (22) Ikeda, K.; Fujimoto, N.; Uosaki, K. *J. Phys. Chem. C* **2014**, *118*, 21550.
- (23) Walczak, M. M.; Chung, C.; Stole, S. M.; Widrig, C. A.; Porter, M. D. *J. Am. Chem. Soc.* **1991**, *113*, 2370.
- (24) Bryant, M. A.; Pemberton, J. E. *J. Am. Chem. Soc.* **1991**, *113*, 8284.
- (25) Hara, K.; Akiyama, R.; Takakusaki, S.; Uosaki, K.; Yoshino, T.; Kagi, H.; Sawamura, M. *Angew. Chem. Int. Ed.* **2008**, *47*, 5627.
- (26) Offord, D. A.; Sachs, S. B.; Ennis, M. S.; Eberspacher, T. A.; Griffin, J. H.; Chidsey, C. E. D.; Collman, J. P. *J. Am. Chem. Soc.* **1998**, *120*, 4478.

# Chapter 3

## Kinetic behavior of electrochemical reactions on catalytic active sites connected with an Au electrode

### 3.1 Introduction

In this chapter, oxygen reduction reaction (ORR) is utilized as a model electrocatalytic reaction to investigate the relation between surface structures and functionality. ORR is of great importance as a cathodic reaction in fuel cells since the efficiency of this multi-electron reaction significantly affect the overall energy conversion efficiency. ORR can undergo two possible pathways: (i) one involving two-electron reduction to give hydrogen peroxide ( $\text{H}_2\text{O}_2$ ) which may be eventually reduced to water ( $\text{H}_2\text{O}$ ); (ii) the other involving four-electron reduction to give  $\text{H}_2\text{O}$  directly. As for fuel cells, developing an efficient four-electron reduction catalysts is the main concern because this reaction can release more energy than the two-electron reduction reaction. However, the four-electron ORR may proceed through various reaction routes involving the O-O bond cleavage, and therefore may not be suitable for a model for studying the interface electron transfer kinetics. On the other hand, the two-electron reaction is thought to be rather simple and suitable for the present work. Among various molecular catalysts, cobalt-porphyrin (CoP) and cobalt-phthalocyanine (CoPC) are known to be good catalysts for the two-electron ORR.<sup>1,2</sup> In this chapter, CoP is mainly utilized as a model catalyst forming the layer-by-layer functional layers. As explained in Chapter 2, well-defined catalyst/wire/electrode systems can be fabricated by layer-by-layer assembly of functional molecular components on an Au electrode, which enables to tune the strength of the interface coupling in the layered system by alternating wire molecules. A comprehensive study of heterogeneous electron transfer kinetics of molecular catalyst-modified electrodes is presented in terms of the contribution of the electronic coupling strength between molecular catalysts and electrode. To elucidate the

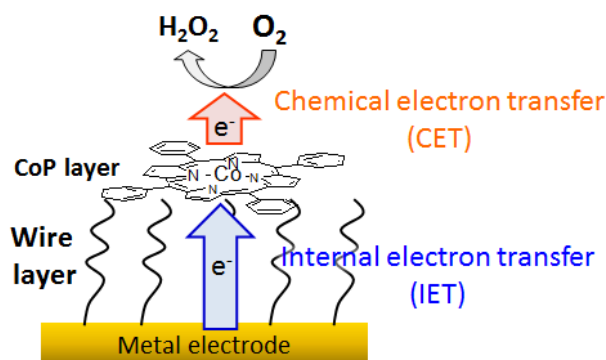


Figure 3.1.1. Schematic of CoP layer connected on a metal surface through wire molecules.

relation between the interface structure and the ORR activity, the overall reaction kinetics is hereinafter expressed as a combination of the electron transfer through wire molecules and catalytic reaction between CoP and O<sub>2</sub> molecules, as shown in Figure 3.1.1. Note that the first electron transfer step is rate-limiting in the latter reaction while the overall ORR is the two-electron reduction reaction. Thus, we can regard these two steps as internal electron transfer (IET) and chemical electron transfer (CET), respectively. When the CoP-Au interactions are weak enough, i.e., the weak coupling limit is valid, these ETs can be treated individually. The main interest here is the breaking of the weak coupling limit in the kinetic behavior when the CoP-Au interactions is non-negligible near the electrode surface. Moreover, the electrode-anchor connection is controlled by using formation of monoatomic metal overlayers, which may affect IET rather than CET. These results provide how chemically functionalized electrodes should be constructed at the molecular scale in order to improve their performance.

### 3.2 Experimental

The details for sample preparation and characterization was described in Chapter 2. The RDE measurements were conducted using a potentiostat (Hokuto Denko, HSV-110), a rotating electrode speed control unit (Pine Instrument, AFMSRCE), and a rotating disk electrode (RDE) with a home-built holder for chemically modified Au disk with a diameter of 10.0 mm. The experiments were carried out in O<sub>2</sub>-saturated 0.5 M H<sub>2</sub>SO<sub>4</sub> aqueous solutions in a three electrochemical cell, which were purged with ultrapure O<sub>2</sub> gas (99.999 %) for 1 hour prior to each measurement. The reversible hydrogen electrode (RHE) and a Pt wire were used as reference counter electrodes, respectively. The ORR polarization curves were recorded with various disk rotation rate ( $\omega$ ) of 500, 1000, 1500 and 2000 rpm at the potential sweep rate of 10 mV·s<sup>-1</sup>. Most of the measurements were carried out at room temperature. For temperature dependence experiments, the cell temperature was controlled at 20, 30, 35, 40°C in a home-built aluminum block equipped with thermoelectric peltier controller.

### 3.3 ORR rates of CoP/wire/Au

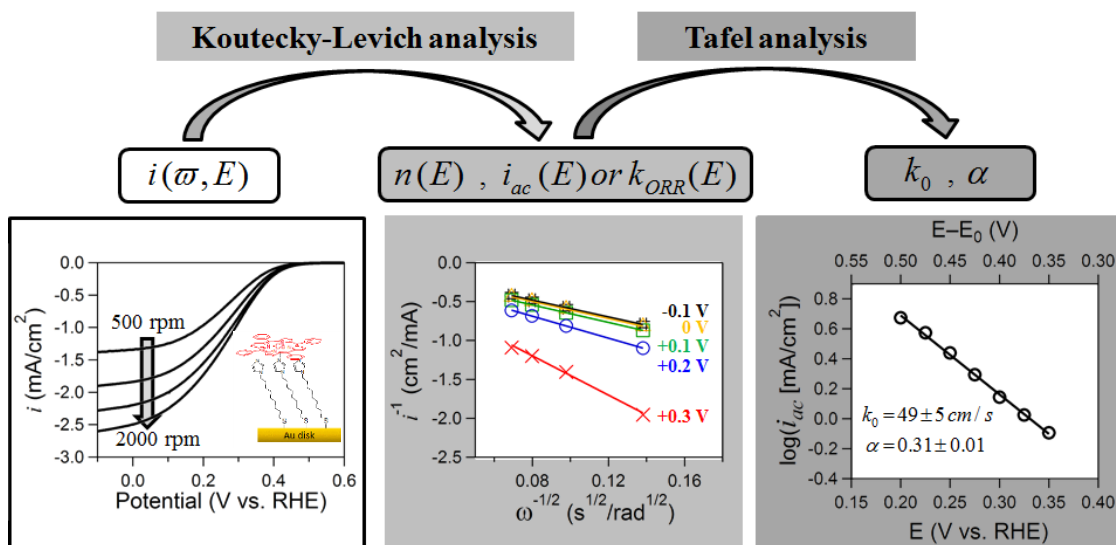


Figure 3.3.1. Flowchart of the analytical procedure for the ORR kinetics of CoP/ImC<sub>9</sub>SH-SAM/Au. (left) ORR polarization curves,  $i_{\text{ORR}}(\omega, E)$ , measured in O<sub>2</sub>-saturated 0.5 M H<sub>2</sub>SO<sub>4</sub> solution at the sweep rate of 10 mV·s<sup>-1</sup> with different rotation rates. (middle) Koutecky-Levich plots of  $i_{\text{ORR}}(\omega, E)$  for various electrochemical potentials. (right) Tafel plots obtained from  $i_{\text{ac}}(E)$ . Finally, the  $\omega$ -independent  $k_0$  and  $\alpha$  can be obtained from  $i_{\text{ORR}}(\omega, E)$ .

The details of the RDE measurements and analyses were described in chapters 1 and 2. Here, the application of the method to the ORR study is provided briefly. Figure 3.3.1 shows a case of the analytical procedure for the kinetics of ORR on the CoP/ImC<sub>9</sub>SH-SAM/Au, measured in O<sub>2</sub>-saturated 0.5 M H<sub>2</sub>SO<sub>4</sub> solution using the RDE method.<sup>3</sup> In this method, the ORR current density,  $i_{\text{ORR}}$ , is obtained as a function of both  $\omega$  and  $E$ , where  $\omega$  is the angular velocity of the RDE in rad·s<sup>-1</sup> and  $E$  is the potential in V vs. RHE, as shown in the left panel of Figure 3.3.1. The measured  $i_{\text{ORR}}(\omega, E)$  can be then analyzed according to the Koutecky-Levich equation,<sup>4</sup>

$$\begin{aligned} 1 / i_{\text{ORR}}(\omega, E) &= 1 / i_{\text{ac}}(E) + 1 / i_{\text{L}}(\omega, E) \\ &= 1 / n(E)Fk_{\text{ORR}}(E)c_{\text{O}_2} + 1 / 0.2n(E)FD^{2/3}\nu^{-1/6}c_{\text{O}_2}\omega^{1/2} \end{aligned} \quad (1)$$

where  $i_{\text{ac}}$  and  $i_{\text{L}}$  denote the activation-controlled current density and the mass-transport-limited current density, respectively,  $n(E)$  is the number of electrons transferred per O<sub>2</sub> molecule,  $F$  the Faraday constant,  $k_{\text{ORR}}(E)$  the reaction rate constant,  $c_{\text{O}_2}$  the concentration of dissolved O<sub>2</sub>,  $D$  the diffusion coefficient of O<sub>2</sub>,  $\nu$  the viscosity of solvent. For these parameters, the following values were utilized in the analysis:  $c_{\text{O}_2} = 1.2 \times 10^{-6}$  mol·cm<sup>-3</sup>,  $D = 1.9 \times 10^{-5}$  cm<sup>2</sup>·s<sup>-1</sup>,  $\nu = 1.1 \times 10^{-2}$  cm<sup>2</sup>·s<sup>-1</sup>.<sup>1,5-8</sup> As shown in the middle panel of Figure 3.3.1,  $i_{\text{ac}}(E)$  and  $i_{\text{L}}(E)$ , i.e.,  $k_{\text{ORR}}(E)$  and  $n(E)$ , are obtained using the linear fitting at each potential.

Further analysis for  $i_{ac}(E)$  can be made according to the Tafel equation,

$$\eta = a + b \log |i_{ac}| \quad (2)$$

where  $\eta = E - E_0$  denotes the overpotential for the redox reaction of  $O_2/H_2O_2$ . Here, the Tafel slope and intercept are  $b = 2.3RT/(anF)$  and  $-a/b = \log |i_0| = \log |nFk_0c_{O_2}|$ , respectively. The transfer number,  $\alpha$ , is assumed to be potential-independent.  $k_0$  is the rate constant for the exchange current at the equilibrium,  $k_0 = k_{ORR}(\eta = 0 \text{ V})$ . As shown in the right panel of Figure 3.3.1,  $\log |i_{ac}|$  is proportional to  $\eta$ . Thus, the kinetic behavior of the overall reaction on CoP/ImC<sub>9</sub>SH-SAM/Au is described by the  $\omega$ -independent parameters:  $k_0 = 49 \pm 5 \text{ cm}^{-1}$  and  $\alpha = 0.31 \pm 0.01$ , although the contributions of both IET and CET are not disentangled.

Figure 3.3.2 shows typical RDE polarization curves of ORR measured for ImC<sub>9</sub>SH-SAM/Au and CoP/ImC<sub>9</sub>SH-SAM/Au. In the absence of CoP, the ORR current was quite small in the entire region of electrochemical potentials. On the other hand, a significant increase of the ORR current was observed in the presence of CoP, indicating that CoP is indeed capable of catalyzing ORR. It is here noted that this confirmation was repeated for all of the wire molecules used in this work, prior to the kinetic analysis of the ORR polarization curves.

In the Koutecky-Levich analysis,  $n(E)$  approached 2 under sufficient negative overpotential application, indicating that the reaction on CoP involves the exchange of two electrons per  $O_2$  molecule:  $O_2 + 2e^- + 2H^+ \rightarrow H_2O_2$ . This is in good agreement with the previous reports for CoP.<sup>1,9,10</sup> Incidentally, a two-electron reduction of  $O_2$  is believed to be much simple, compared with a four-electron reduction of  $O_2$ .<sup>1,11</sup> Therefore, CoP was chosen in this study as a model catalyst to investigate the contributions of IET and CET.

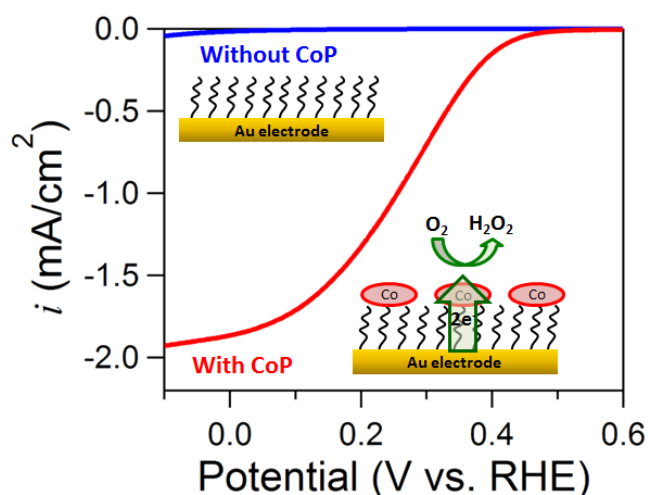


Figure 3.3.2. ORR polarization curves for ImC<sub>9</sub>SH-SAM/Au and CoP/ImC<sub>9</sub>SH-SAM/Au, measured in  $O_2$ -saturated 0.5 M  $H_2SO_4$  solution using the RDE method at the scan rate of 10  $mV \cdot s^{-1}$  with the rotation rate of 1000 rpm.

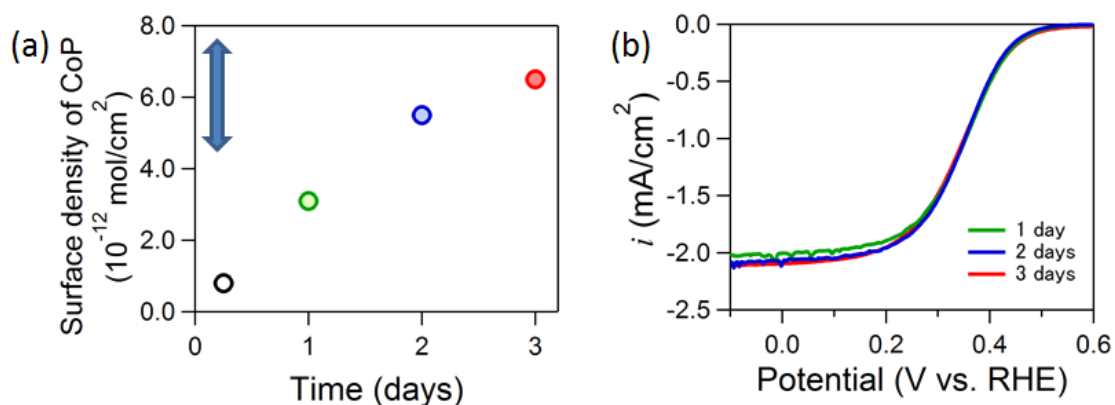


Figure 3.3.3. (a) Surface density of CoP on PySH-SAM/Au as a function of the immersion time into chloroform solution containing 0.1 mM CoP. (b) ORR polarization curves of CoP/PySH-SAM/Au with different CoP densities, measured using RDE technique with the rotation rate of 1000 rpm.

The overall kinetic behavior of the modified electrode may be dependent on the surface density of the catalytic active CoP immobilized on the electrode. In the present system, the surface density was able to be measured using the redox response of the central Co ions. As is mentioned in Chapter 2, the CoP density estimated for various wire molecules was in the range of  $6.3 \pm 1.2 \times 10^{-12} \text{ mol}\cdot\text{cm}^{-2}$ , which is indicated as a blue arrow in Figure 3.3.3. Although this density distribution was not so small, the influence to the ORR kinetics was still negligible for the relatively low current density in the present experiments; the surface density of CoP was changed on PySH-SAM/Au as a function of the immersion time of the electrode, but the ORR behavior was not affected by the difference of the CoP density. In the present work, the saturation condition for CoP adsorption was chosen to form the CoP layer, in order to minimize the difference in the CoP density among the samples. Therefore, we can expect that wire molecule-dependent ORR behavior is not due to the difference in the surface density of ORR active sites.

### 3.4 Influence of wire structures on ORR rates

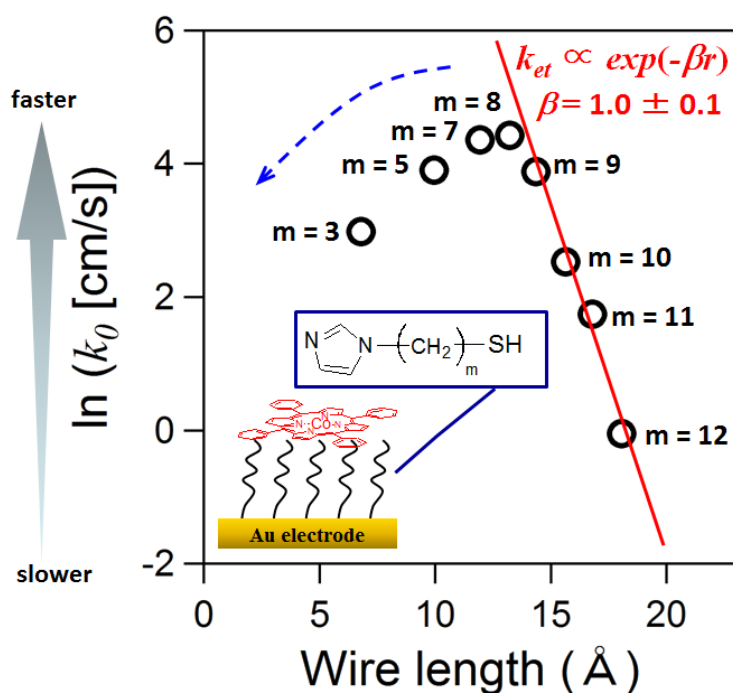


Figure 3.4.1. Semi-log plot of  $k_0$  obtained for a series of CoP/ImC<sub>m</sub>SH-SAM/Au as a function of the wire length of ImC<sub>m</sub>SH ( $m = 3, 5, 7, 8, 9, 10, 11, 12$ ).

When the wire length,  $r$ , is changed in the layered system, IET will be changed as a result of the change in the electronic coupling strength between CoP and Au if we assume that the weak coupling limit is valid for the CoP-Au interactions. According to many reports on molecular conductance in metal-molecule-metal junctions, when IET can be treated as a coherent quantum tunneling in the weak coupling limit, the rate of IET decays exponentially with increasing  $r$ .<sup>12,13</sup> However, the relation between IET and  $k_0$  may not be straightforward because CET is involved in the heterogeneous reaction. Figure 3.4.1 shows a semi-log plot of  $k_0$  obtained for a series of CoP/ImC<sub>m</sub>SH-SAM/Au as a function of the wire length of ImC<sub>m</sub>SH. For  $m > 8$ , i.e., for the relatively long wire length ( $r > \sim 13$  Å), an exponential relation is clearly observed; the exponential decay coefficient,  $\beta$ , in  $k_0 \propto e^{-\beta r}$  was estimated to be  $1.0 \pm 0.1$  Å<sup>-1</sup>. This is close to the value reported for electron tunneling through alkyl chains.<sup>12-15</sup> When  $r$  is sufficiently long, it is naturally expected that the electronic coupling can be treated under the approximation of the weak coupling limit. Under this circumstance, the activity of CoP remains the same for changing  $r$ , so that the observed length dependence of  $k_0$  can be ascribed to the change in the rate of IET. Therefore, the exponential decay observed for  $m > 8$  indicates that IET is rate-limiting in this wire length region. On the other hand, for  $m \leq 8$ , i.e., for the relatively short wire length ( $r < \sim 13$  Å),

$k_0$  is clearly apart from the exponential relation. Notably, this deviation becomes larger with decreasing  $r$ ; the maximum  $k_0$  was observed when  $r$  was at  $\sim 13 \text{ \AA}$ . It is expected that IET became comparable with CET in this wire length region. Thus, the decrease in  $k_0$  may be ascribed to a decrease in CET as a result of the change in the activity of CoP, which will be discussed later.

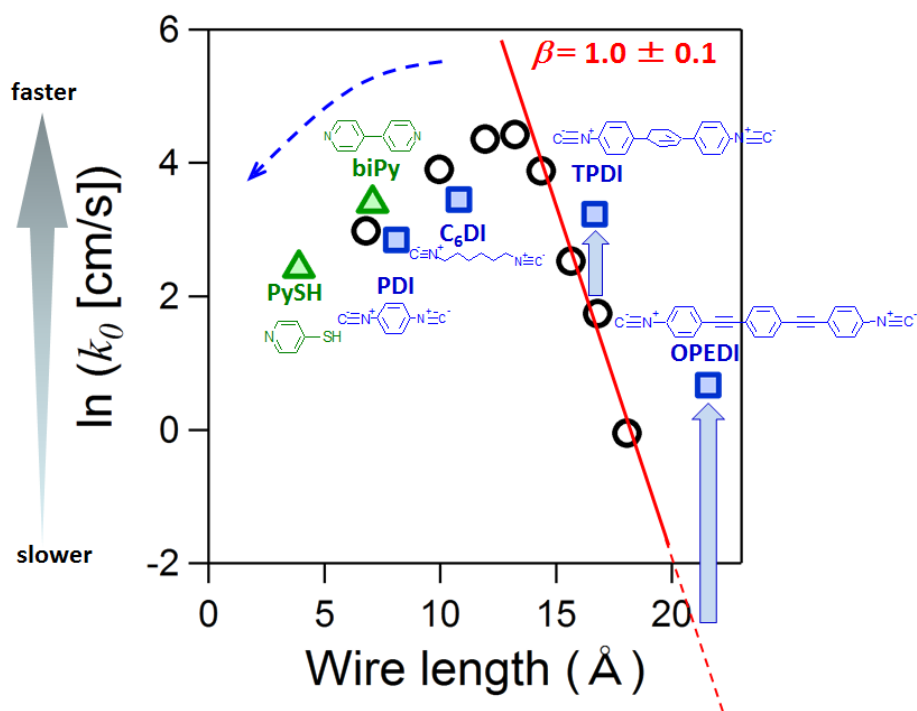


Figure 3.4.2. Wire length dependence of  $k_0$  for other wire molecules in addition to Figure 3.4.1.

The wire length dependence of  $k_0$  is more clearly presented in Figure 3.4.2, where  $k_0$  obtained for other types of the wire molecules are plotted along with those for the series of  $\text{ImC}_m\text{SH}$ . It is noted that biPy, PDI, TPDI, and OPEDI have a  $\pi$ -conjugated chain, while  $\text{C}_6\text{DI}$  and  $\text{ImC}_m\text{SH}$  have a saturated alkyl chain. PySH is the shortest wire molecule in the present study. In the longer wire length region ( $m > 8$  or  $r > 13 \text{ \AA}$ ),  $k_0$  for TPDI and OPEDI was much larger than the values expected from the exponential relation of  $\text{ImC}_m\text{SH}$ , indicated by the red line. It is widely accepted that molecular conductance of  $\pi$ -conjugated molecules is larger than those of saturated molecules (for example, the decay coefficient,  $\beta$ , is estimated to be  $\sim 0.27 \text{ \AA}^{-1}$  for the chain body of OPEDI and  $0.78 \text{ \AA}^{-1}$  for the alkyl chain).<sup>12,13,15-17</sup> Therefore, this tendency is readily acceptable when IET is rate-limiting. For the shorter wire length region, on the other hand,  $k_0$  for PySH, biPy, PDI, and  $\text{C}_6\text{DI}$  showed a similar tendency with the series of  $\text{ImC}_m\text{SH}$ ; their deviation from the red line was on the same trend with  $\text{ImC}_m\text{SH}$ . This result shows that  $k_0$  is not affected much by  $\pi$  of wire molecules in this region, suggesting that CET is rate-limiting.

Indeed, PDI and C<sub>6</sub>DI are good examples for this conclusion because they have the same anchor groups but the different chain structure;  $k_0$  for PDI was smaller than that for C<sub>6</sub>DI whereas PDI should be more conductive than C<sub>6</sub>DI.

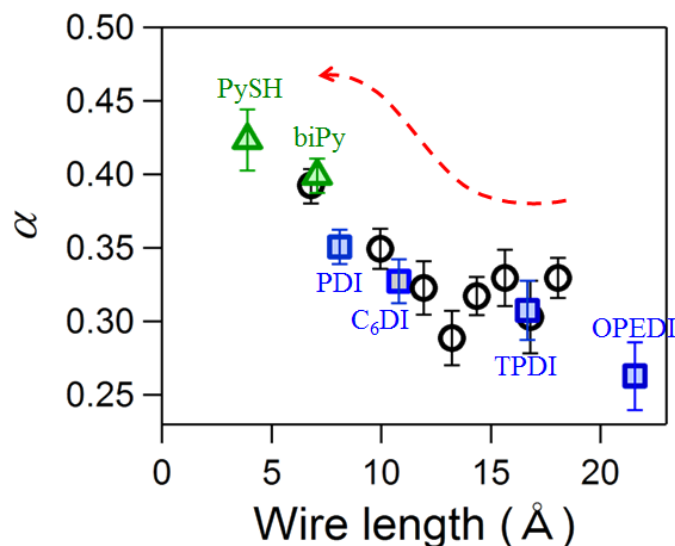


Figure 3.4.3. Wire length dependence of  $\alpha$  obtained for a series of CoP/wire/Au.

In addition to  $k_0$ , the transfer number,  $\alpha$ , is also dependent on  $r$ . As shown in Figure 3.4.3,  $\alpha$  obtained for various types of CoP/wire/Au increases with decreasing  $r$ ; this trend becomes pronounced especially for  $m \leq 8$ . Clearly, the wire length dependence of  $\alpha$  closely correlates with that of  $k_0$ . In a heterogeneous electrochemical reaction,  $\alpha$  denotes the fraction of the interfacial potential that can lower the free energy barrier for the reaction, and thus represents sensitivity of the reaction rate toward the potential application. Therefore, the rapid increase in  $\alpha$  in the shorter wire length region indicates that the influence of the applied potential to CoP becomes more significant near the Au surface; the electronic coupling between CoP and Au is stronger in this region. Consequently, the correlated behavior between  $k_0$  and  $\alpha$  indicates that the ORR activity of CoP is diminished near the Au surface due to the electronic coupling between CoP and Au electrode.

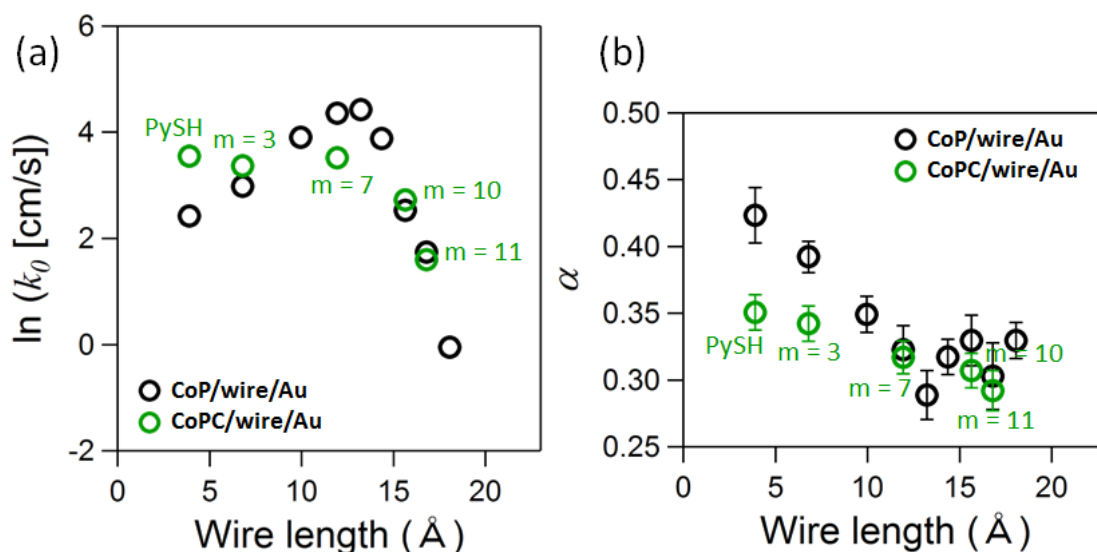


Figure 3.4.4. (a) The rate constant  $k_0$  and (b) transfer number  $\alpha$  as a function of wire length, measured for CoP/wire/Au and CoPC/wire/Au, where PySH and the series of ImC<sub>m</sub>SH were utilized to form wire-SAMs.

A similar correlation of  $k_0$  with  $\alpha$  was observed even when catalytic surface sites were formed using CoPC, which also functions as a two-electron ORR catalyst.<sup>1,18</sup> It is known that CoP and CoPC with different macrocyclic ligand structures exhibit different activity for two-electron reduction of O<sub>2</sub>; in the most of previous studies, these molecules have been directly adsorbed on a metallic surface such as graphite or Au.<sup>19</sup> This activity difference is observed even when the molecules are attached on the SAM-covered Au. Figure 3.4.4 shows the rate constant  $k_0$  and transfer number  $\alpha$  as a function of wire length, measured for CoP/wire/Au and CoPC/wire/Au, where PySH and the series of ImC<sub>m</sub>SH were chosen as wire molecules to focus on the wire length dependence. When the wire length is relatively long ( $r > \sim 13$  Å), IET is rate-limiting. Therefore, the kinetic behavior is expected to be independent of the activity of the catalytic sites. Indeed, both catalytic molecules showed very similar kinetic behaviors. In contrast, when the wire length is short, CET becomes rate-limiting, i.e., the reaction rate should be dependent on the activity. This is indeed observed in the figure; both of  $k_0$  and  $\alpha$  was changed with decreasing the wire length  $r$ . Although the overall kinetic behavior was similar between CoP and CoPC, the degree of the  $r$ -dependent change was clearly different. That is, the change in  $k_0$  or  $\alpha$  was more pronounced in CoP compared with CoPC, indicating that the activity of CoP was largely diminished by the electronic coupling with the conducting substrate. In contrast, the influence to the activity of CoPC seems to be small near the Au surface. At the same time, the responsivity to the potential did not improve much even when CoPC were located near the Au

surface, indicating that the coupling between CoPC and Au is not strong as the case for CoP. This difference between CoP and CoPC should be related to the different electronic structure of the macrocycle ligands. Therefore, there is a possibility to tune the activity and responsivity of catalytic active sites near a conducting surface by structural design of the ligand around central metal ions.

The contribution of the Au-CoP interaction can be also confirmed in the wire length dependence of Co(II/III) oxidation peak potential shown in Figure 3.4.5. As explained in Chapter 2, the peak potential exhibited so-called odd-even effect in the longer wire region with the length of more than 13 Å. This can be explained by the difference of CoP-imidazole coupling strength because the orientation of the imidazole is dependent of the carbon number of the wire

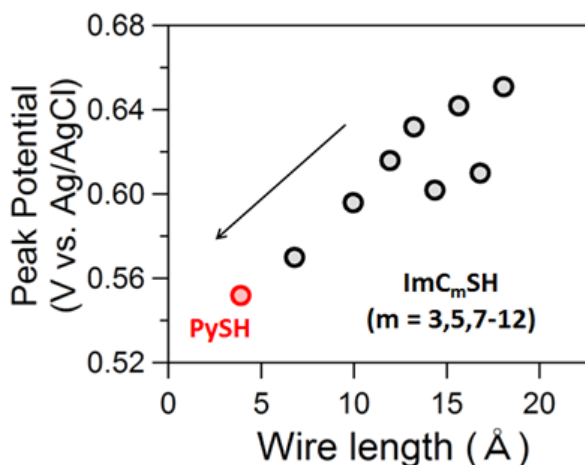


Figure 3.4.5. (Figure 2.5.4.) Oxidation peak potential of Co(II/III) as a function of the wire length from each CVs.

molecules. For the ORR activity, such an odd-even effect was not observed; this also supports that IET is rate-limiting in this region. On the other hand, in the shorter wire region, the peak potential clearly shifted negatively with decreasing wire length. This negative shift can be explained by the increased electronic coupling between Au and CoP, resulting in the increase in  $\alpha$  as shown in Figure 3.4.4. Presumably, this substrate effect diminished the ORR activity of CoP through the decrease in the electron density of Co centers. Of course, detailed modeling of the electronic coupling in the complete system including larger gold contacts and even the medium will be needed to support this explanation for the experimentally observed wire length dependence of the ET kinetics.

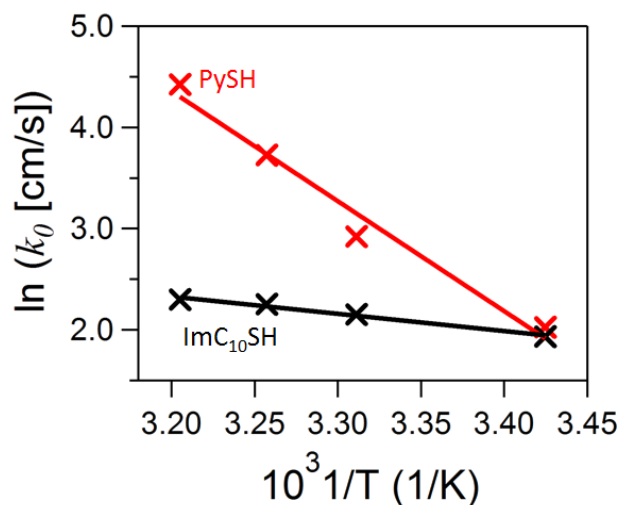


Figure 3.4.6. Arrhenius plots of  $k_0$ , measured for CoP/PySH-SAM/Au and CoP/ImC<sub>10</sub>SH-SAM/Au.

The characteristic wire length dependence of the ORR kinetics near Au surface is thought to be accompanied by the change of the rate-limiting step between IET and CET. The former is characterized by the coherent quantum electron tunneling through the wire molecules. The latter is related to the activity of CoP. These two different processes are expected to exhibit different temperature dependence. According to Arrhenius equation, the temperature dependence of the reaction rate can be expressed as,

$$\ln k_0 = \ln A - \Delta G^\ddagger / (RT) \quad (3)$$

where  $A$  is pre-exponential factor,  $\Delta G^\ddagger$  is standard free energy of activation and  $T$  stands for temperature in Kelvin. In Figure 3.4.6, the temperature dependence of  $k_0$  is presented as  $\ln k_0$  vs.  $1/T$  for two wire molecules: the shortest PySH and much longer ImC<sub>10</sub>SH. As expected, the rate of ORR on CoP/wire/Au exhibited different temperature dependence between these wire molecules. In the case of the shortest PySH,  $k_0$  was significantly changed against temperature, which agreed with the assumption that CET was rate-limiting. The activation energy,  $\Delta G^\ddagger$ , for ORR was estimated to be  $89 \pm 2$  kJ/mol by fitting the observed linear relation; the relatively large activation energy may be due to the suppression of the activity near Au surface. In contrast, the temperature dependence of  $k_0$  was much smaller for ImC<sub>10</sub>SH, suggesting that IET is indeed rate-limiting.

Intramolecular ET behavior has been extensively studied theoretically and experimentally using a donor-bridge-acceptor model.<sup>12,13,20-23</sup> The rate of the electron transfer from the donor to acceptor,  $k_{D \rightarrow A}$ , is given by

$$k_{D \rightarrow A} = 2\pi/\hbar |V_{DA}|^2 D_{FC} \quad (4)$$

where  $V_{DA}$  is the coupling between the donor and acceptor electronic states and  $D_{FC}$  is the thermally averaged, Franck-Condon-weighted density of nuclear states. The coupling,  $V_{DA}$ , is dependent on the bridge length. In the present heterogeneous electrochemical system involving the catalytically assisted CET, the donor and acceptor correspond to the anchor group chemisorbed to the Au electrode and CoP interacting with  $O_2$ , respectively, and thus  $k_{D \rightarrow A}$  corresponds to the rate of IET. When the coupling is weak, the internal ET can be treated as a coherent quantum tunneling through the virtual electronic states. Then, the length dependence of the rate constant is  $k_{D \rightarrow A} \propto e^{-\beta r}$ , as already mentioned. Indeed,  $k_0$  decayed exponentially with increasing  $r$  when  $m > 8$  ( $r > \sim 13$  Å) in the present study. Moreover,  $k_0$  was dependent on  $\beta$  in the same wire length region. It is evident that IET is rate-limiting for  $k_0$  when  $r > \sim 13$  Å.

On the other hand, in the strong coupling limit for equation (4), the nearest neighbor interactions may not be dominant in the bridge or the electron may be delocalized over the entire donor-bridge-acceptor system, resulting that the length dependence of  $k_{D \rightarrow A}$  is inversely proportional to  $r$ . In the present electrochemical system, a deviation from the quantum tunneling behavior should be expected for IET in a shorter wire length region. However, such Ohmic behavior cannot explain the significant decrease in  $k_0$  observed for  $m \leq 8$  ( $r < \sim 13$  Å). Instead, the alternation of the rate-limiting process from IET to CET was strongly suggested by the experimental results: the  $\pi$ -independence of  $k_0$ , the peak shift of CoP redox, and the larger temperature dependence for the shorter wire molecules. Therefore, the decrease in  $k_0$  near the Au surface is mainly explained by the decrease in CET as a result of a drop in the ORR activity of CoP. In general, the activity of CoP is explained as follows: Oxygen binding with a Co center in porphyrin is related to partial charge transfer from a highest occupied metal 3d orbital to the  $\pi^*$  orbital of oxygen molecule. To improve ORR activity of Co porphyrins, the energy gap between 3d orbital of Co and  $O_2$  needs to be decreased, and electron-donating substituents can raise the Co 3d orbital energy.<sup>24-26</sup> Thus, in the present CoP system, the decrease of the ORR activity near Au surface strongly suggests that the stronger Au-CoP interaction induced electron-withdrawing of Co centers.

### 3.5 Influence of metal-anchor junctions

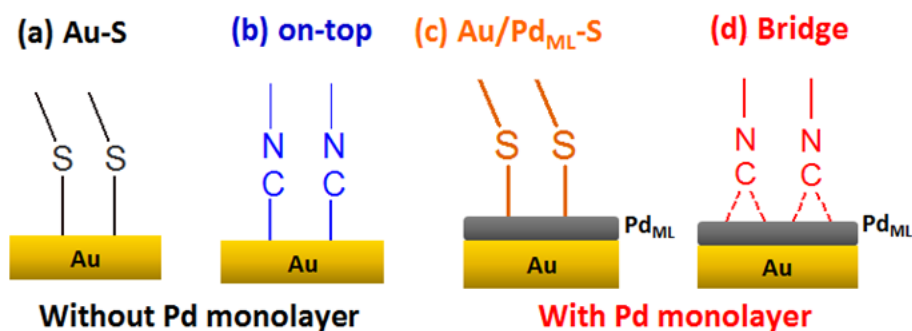


Figure 3.5.1. Illustrate of the interface structures between the electrode and wire molecules without ((a) Au-S, (b) Au-CN(on-top)) and with Pd<sub>ML</sub> ((c) Au/Pd<sub>ML</sub>-S, (d) Au/Pd<sub>ML</sub>-CN(Bridge)).

In the section 3.5, it was confirmed that there was a limit to optimize the Au-CoP connection with respect to wire molecule structures; the shorter wire length improved IET but decreased CET. In this section, an influence of the metal-anchor junction to the overall reaction rate is presented in terms of the reduction of the interfacial resistance. In the field of molecular electronics, charge transport at metal-molecule junctions is one of significant interests, and it is believed that the interface structure on the atomic scale significantly affects the transport. Indeed, a recent report clearly showed that the conductance of thiol-Au junctions is dependent on the adsorption sites using single-molecule spectro-conductance measurements consisting of a mechanical break junction system and a Raman microscope.<sup>32</sup> Figure 3.5.1 shows four different types of interface connections utilized in this work; thiol on Au (Au-S), thiol on Au/Pd<sub>ML</sub> (Au/Pd<sub>ML</sub>-S), isocyanide on Au (Au-CN(on-top)), and isocyanide on Au/Pd<sub>ML</sub> (Au/Pd<sub>ML</sub>-CN(Bridge)). In the case of thiols (-S), the presence of Pd<sub>ML</sub> is expected to weaken the adsorption strength although the information on adsorption sites is not clearly obtained.<sup>27,28</sup> On the other hand, the adsorption geometry of the isocyanide anchor group was already confirmed using the PM-IRRAS (see Chapter 2). In the presence of Pd<sub>ML</sub>, the anchor geometry changed from the on-top to the bridge configuration, indicating the stronger adsorption on Pd than on Au.<sup>29-</sup><sup>31</sup> One important point is that Pd monolayer is completely covered with wire molecular layer; hence, these SAM-covered Au/Pd<sub>ML</sub> electrodes are electrochemically inert in the absence of CoP. In other words, direct contribution of Pd<sub>ML</sub> to ORR is negligible in the present system.

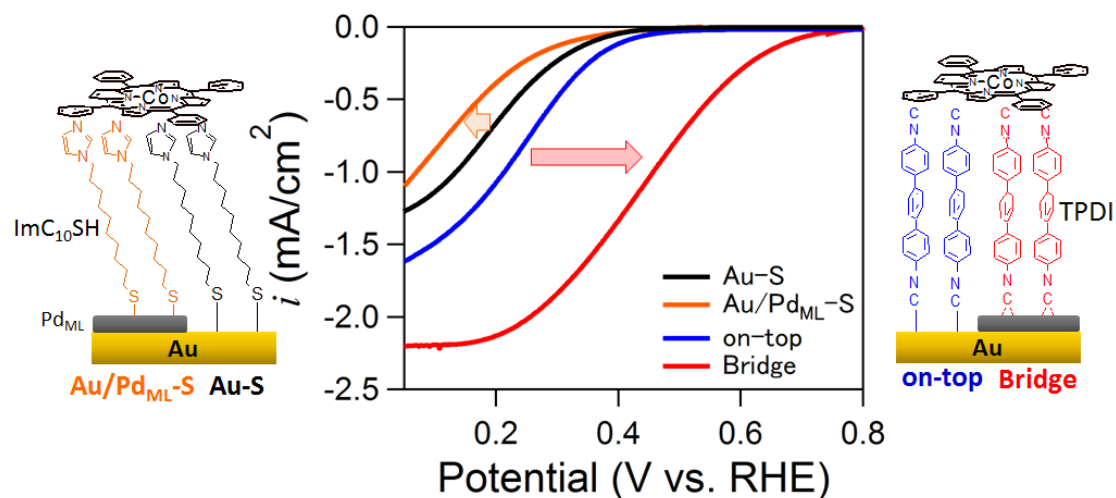


Figure 3.5.2. ORR polarization curves on CoP catalyst layers formed on the molecular wire monolayer of Imidazole-terminated alkanethiol (ImC<sub>10</sub>SH) and diisocyanide (TPDI) with and without Pd<sub>ML</sub>, measured by RDE method with rotation rate of 1000 rpm.

Figure 3.5.2 shows the polarization curves for ORR on the CoP-modified electrodes formed with two different wire molecules of similar lengths: ImC<sub>10</sub>SH and TPDI. The small difference of the ORR overpotential between Au-S and Au-CN (on-top) is mainly caused by the difference of  $\pi$ -conjugation in the wire body. In the presence of Pd<sub>ML</sub>, these wire molecules exhibited opposite tendency for the ORR rate; Au/Pd<sub>ML</sub>-S showed undesirable increase in the ORR overpotential whereas Au/Pd<sub>ML</sub>-CN (bridge) presented a significant decrease in the overpotential.

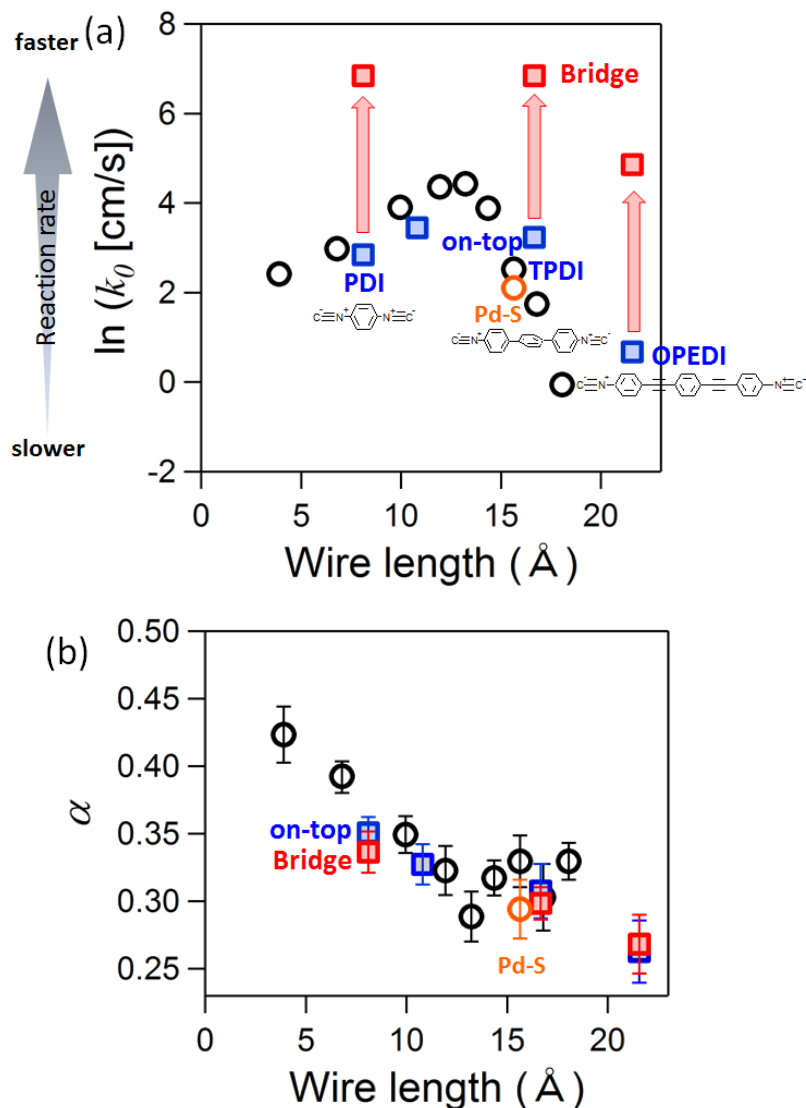


Figure 3.5.3. (a) The rate constant  $k_0$  and (b) transfer number  $\alpha$  as a function of wire length, measured for the CoP-modified electrodes with the four different interface structures: Au-S (black circles), Au/Pd<sub>ML</sub>-S (orange circle), Au-CN (on-top, blue squares), and Au/Pd<sub>ML</sub>-CN (bridge, red squares).

The effect of the Pd<sub>ML</sub> is more clearly presented in  $k_0$ . Figure 3.5.3a shows plots of  $k_0$  values measured on CoP-modified Au/Pd<sub>ML</sub> electrodes with wire molecules of PDI, TPDI, OPEDI and ImC<sub>10</sub>SH as well as those on CoP-modified Au electrodes presented in Figure 3.4.2. All isocyanide molecules (PDI, TPDI and OPEDI) showed significant increase in  $k_0$  in the presence of Pd<sub>ML</sub>. The important point is that this increase was observed even in the shorter wire length region where CET is rate-limiting. On the other hand, Figure 3.5.3b shows that the presence of Pd<sub>ML</sub> did not affect the  $\alpha$ , indicating that the CoP-substrate interactions were not changed with and without Pd<sub>ML</sub>. It is therefore thought that CET remains intact in the presence of Pd<sub>ML</sub>.

Consequently, it is natural to conclude that Pd-CN junction has a better electron transport property than the other junctions such as Pd-S, Au-S, and Au-CN (on-top). The formation of bridge configuration is presumably a key for this enhancement.

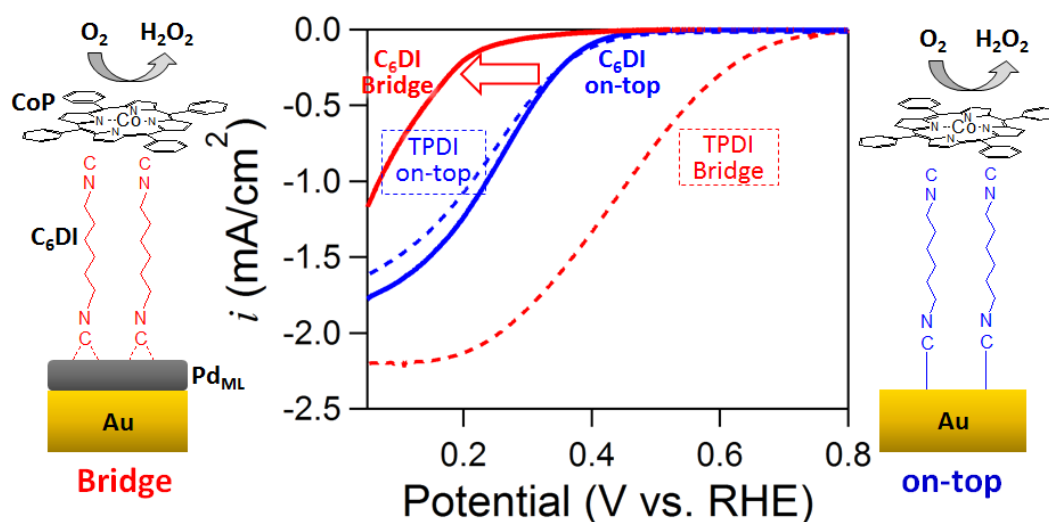


Figure 3.5.4. ORR polarization curves on CoP catalyst layers formed on C<sub>6</sub>DI-SAMs with and without Pd<sub>ML</sub>, measured by RDE method with rotation rate of 1000 rpm.

Actually, the effect of the Pd-CN junction is dependent on the  $\pi$ -conjugation degree of the wire molecules. Figure 3.5.4 shows the comparison of the ORR polarization curves measured on the CoP layers formed on alkyl isocyanide (C<sub>6</sub>DI-SAMs) or aryl isocyanide (TPDI-SAMs) with and without Pd<sub>ML</sub>. On Au surfaces without Pd<sub>ML</sub>, the ORR curves were very similar between these wire molecules. In the case of C<sub>6</sub>DI, the presence of Pd<sub>ML</sub> largely decreased the reaction rate through the increase of the reaction overpotential. This is completely opposite with the case for TPDI. Since PM-IRRAS showed both wire molecules have the bridge configuration on Pd<sub>ML</sub> surface, this result suggests that the effect of Pd<sub>ML</sub> for PDI, TPDI or OPEDI is not due to the formation of the bridge configuration alone. One reasonable explanation is that the combination of  $\pi$ -conjugated wire and anchor is needed to reduce the interfacial resistance. The Au-S and Pd-S bonds are dominantly formed by  $\sigma$ -bonding. On the other hand, isocyanide anchor allows multiple bonding interactions with the metal substrate via a  $\sigma/\pi^*$  synergistic bonding.<sup>29-31</sup> The on-top configuration on Au is formed dominantly by  $\sigma$ -donation from the carbon lone pair of the isocyanide anchor to Au. The bridge configuration on Pd is formed by  $\pi^*$ -back donation from d orbitals of Pd to  $\pi^*$ -antibonding orbital of CN as well as the  $\sigma$ -donation. Therefore, when the electron pathway in the molecular wires is formed by the  $\sigma/\pi^*$  synergistic bonding and  $\pi^*$ -orbital of  $\pi$ -conjugated wires, i.e., the lowest unoccupied orbital (LUMO), the electron transport can take

place resonantly, leading to a significant decrease in the interfacial resistance. Conversely, when the wire body consists of alkyl chains, such resonant electron transport is not expected; the introduction of the  $\sigma/\pi^*$  synergistic bonding at the metal-anchor contact would reduce the electronic coupling between the main body and anchor in the wire molecule, resulting in further decrease in conductivity.

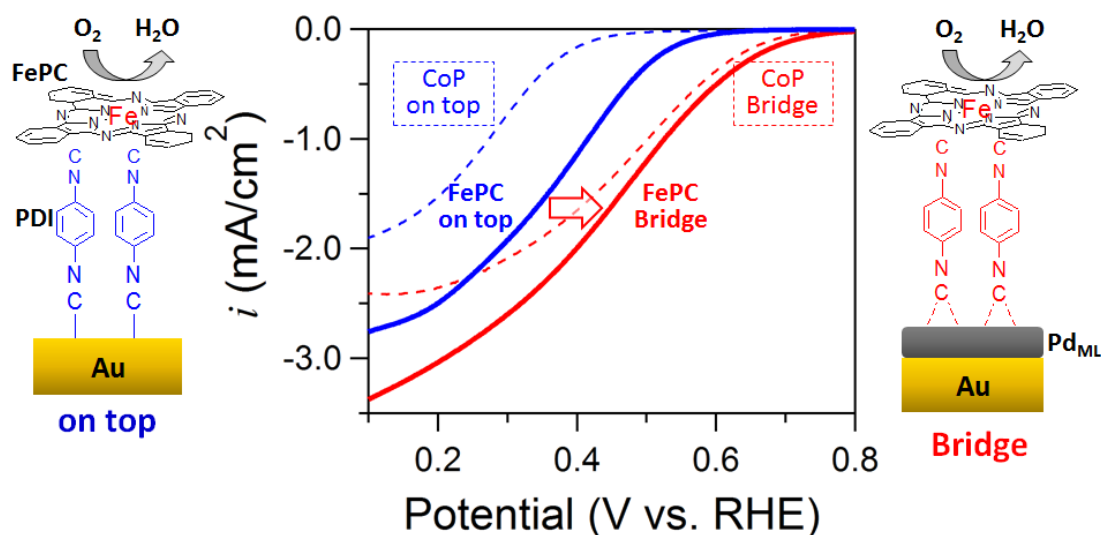


Figure 3.5.5. ORR polarization curves on FePC catalyst layers formed on PDI-SAMs with and without Pd<sub>ML</sub>, measured by RDE method with rotation rate of 1000 rpm.

Now, it is thought that the effect of Pd<sub>ML</sub> is to reduce the interfacial resistance at metal-anchor contacts. If this is true, the effect of Pd<sub>ML</sub> should be independent of the property of molecular catalysts. To confirm such universality, ORR kinetics on FePC was examined with and without Pd<sub>ML</sub>, which is known to be a four-electron ORR catalyst.<sup>20</sup> Figure 3.5.5 shows the comparison of ORR polarization curves for FePC and CoP layers formed on PDI-SAMs with and without Pd<sub>ML</sub>. The presence of Pd<sub>ML</sub> certainly improved the reaction rate in the case of FePC layers, indicating that this strategy is useful for improving interfacial electron transfer rates in various functional surfaces.

### 3.6 Conclusion

The degree of the electronic coupling between catalytic active sites and conducting electrode was systematically tuned by using various types of wire molecules. In the weak coupling condition with the relatively large catalyst-electrode separation, the electronic states of catalytic local sites are rather isolated from the conducting electronic states. Consequently, the overall reaction rate is limited by the electron transport rate at the catalyst-electrode interface while the activity of the catalytic sites is invariant by immobilization to the surface. Under this circumstance, the molecular design for activity enhancement of surface sites is not essential in the overall reaction kinetics. In the strong coupling condition with the relatively short catalyst-electrode separation, the electronic states of the catalytic sites are no longer independent from the conducting electronic states. Then, the catalytic activity is significantly lowered while the electron transport through the wire molecules becomes faster. This takes place even when the catalytic molecules are not directly attached on the electrode. Actually, it is difficult to take into account the substrate effect when catalytic active sites are designed. To develop highly efficient electrocatalysts, therefore, it is better to firstly focus on improvement of intermolecular electron transfers between catalytic molecules and reactants, followed by tuning of the electronic coupling between catalytic sites and a conducting electrode so that both of the internal electron transport and the catalytic activity are properly balanced. For the internal electron transport, the metal-anchor contact is also one essential factor to determine the resistance. Resonant and efficient electron transport can be expected when the orbitals of the metal-anchor bonding are properly connected with LUMO of the wire body. The molecular-scale design for efficient electrocatalysts will be advanced by considering the activity of catalytic local sites and the internal electronic connection to a conducting surface separately.

## References

- (1) Wang, H.; Maiyalagan, T.; Wang, X. *ACS Catal.* **2012**, *2*, 781.
- (2) Zagal, J. H. in: Vielstich, W.; Lamm, A.; H. Gasteiger (Eds.), *Handbook of Fuel Cells-Fundamentals, Technology and Applications*, vol. 2 Part 5, John Wiley & Sons, Ltd., Chichester, 2003, p. 544.
- (3) Markovic, N. M.; Adzic, R. R.; Vesovic, V. B. *J. Electroanal. Chem.* **1984**, *165*, 121.
- (4) Koutecky, J.; Levich, V. G. *Zh. Fiz. Khim.* **1958**, *32*, 1565.
- (5) Collman, J. P.; Marrocco, M.; Denisevich, P. *J. Electroanal. Chem.* **1979**, *101*, 117.
- (6) Gewirth, A. A.; Thorum, M. S. *Inorg. Chem.* **2010**, *49*, 3557.
- (7) Adams, D. M.; Brus, L.; Chidsey, C. E. D.; Creager, S.; Creutz, C.; Kagan, C. R.; Kamat, P. V.; Lieberman, M.; Lindsay, S.; Marcus, R. A.; Metzger, R. M.; Michel-Beyerle, M. E.; Miller, J. R.; Newton, M. D.; Rolison, D. R.; Sankey, O.; Schanze, K. S.; Yardley, J.; Zhu X.. *J. Phys. Chem. B* **2003**, *107*, 6668.
- (8) Wang, G.; Kim, T. -W.; Lee, T.; Wang, W.; Reed, M. A. In *Handbook of Nanoscale Optics and Electronics*, Wiederrecht, G. Ed.; *Elsevier*, **2010**, 141.
- (9) Zagal, J. H.; Griveau, S.; Silva, J. F.; Nyokong, T.; Bedioui, F. *Coord. Chem. Rev.* **2010**, *254*, 2755.
- (10) Tomfohr, J. K.; Sankey, O. F. *Phys. Rev. B*, **2002**, *65*, 245105.
- (11) Sachs, S. B.; Dudek, S. P.; Hsung, R. P.; Sita, L. R.; Smalley, J. F.; Newton, M. D.; Feldberg, S. W.; Chidsey, C. E. D. *J. Am. Chem. Soc.* **1997**, *119*, 10563.
- (12) Hong, S.; Reifengerger, R.; Tian, W.; Datta, S.; Henderson, J.; Kubiak, C. P. *Superlattices Microstruct.* **2000**, *28*, 289.
- (13) Hush, N. S. *Coord. Chem. Rev.* **1985**, *64*, 135.
- (14) Morozan, A.; Campidelli, S.; Filoramo, A.; Josselme, B.; Palacin, S. *Carbon*, **2011**, *49*, 4839.
- (15) Newton, M. D. *Chem. Rev.* **1991**, *91*, 767.
- (16) Barbara, P. F.; Meyer, T. J.; Ratner, M. A. *J. Phys. Chem.* **1996**, *100*, 13148.
- (17) Nitzan, A. *J. Phys. Chem. A* **2001**, *105*, 2677.
- (18) Uosaki, K.; Elumalai, G.; Noguchi, H.; Masuda, T.; Lyalin, A.; Nakayama, A.; Taketsugu, T. *J. Am. Chem. Soc.* **2014**, *113*, 361.
- (19) Zagal, J. H. **1992**, *119*, 89-136.

- (20) Cao, R.; Thapa, R.; Kim, H.; Xu, X.; Kim, M. G.; Li, Q.; Park, N.; Liu, M.; Cho, J. *Nature Commun.* **2013**, *4*, 2076.
- (21) Wei, P. -J.; Yu, G. -Q.; Naruta, Y.; Liu, J. -G. *Angew. Chem. Int. Ed.* **2014**, *53*, 6659.
- (22) Henderson, J. I.; Feng, S.; Bein, T.; Kubiak, C. P. *Langmuir* **2000**, *16*, 6183.
- (23) Stapleton, J. J.; Daniel, T. A.; Uppili, S.; Cabarcos, O. M.; Naciri, J.; Shashidhar, R.; Allara, D. L., *Langmuir*, **2005**, *21*, 11061.
- (24) Shi, Z.; Zhang, J. *J. Phys. Chem. C* **2007**, *111*, 7084.
- (25) Zagal, J. H.; Cardenas-Jiron, G. I. *J. Electroanal. Chem.* **2000**, *489* (1-2), 96.
- (26) Liao, M. S.; Scheiner, S. *J. Comput. Chem.* **2002**, *23* (15), 1391.
- (27) Love, J. P.; Wolfe, D. B.; Haasch, R.; Chabinyk, M. L.; Paul, K. E.; Whitesides, G. M.;uzzo, R. G. *J. Am. Chem. Soc.* **2003**, *125*, 2597.
- (28) Williams, J. A.; Gorman, C. B. *J. Phys. Chem. C* **2007**, *111*, 12804.
- (29) Angelici, R. J.; Lazar, M. *Inorg. Chem.*, **2008**, *47*, 9155.
- (30) Murphy, K. L.; Tysoe, W. T.; Bennett, D. W. *Langmuir*, **2004**, *20*, 1732.
- (31) Swanson, S. A.; McClain, R.; Lovejoy, K. S.; Alamdari, N. B.; Hamilton, J. S.; Scott, J. C. *Langmuir*, **2005**, *21*, 5034.
- (32) Kaneko, S.; Murai, D.; Marqués-González, S.; Nakamura, H.; Komoto, Y.; Fujii, S.; Nishino, T.; Ikeda, K.; Tsukagoshi, K.; Kiguchi, M. *J. Am. Chem. Soc.* in press. DOI: 10.1021/jacs.5b11559

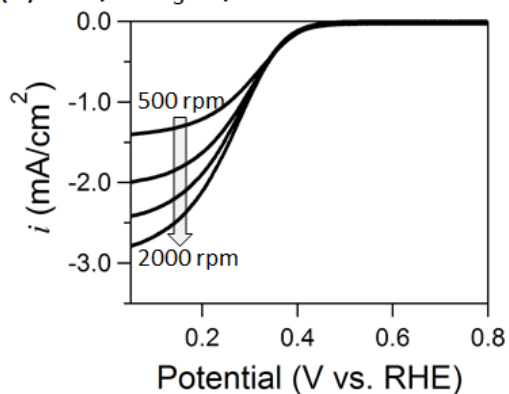
## Appendix

### ORR polarization curves for all samples

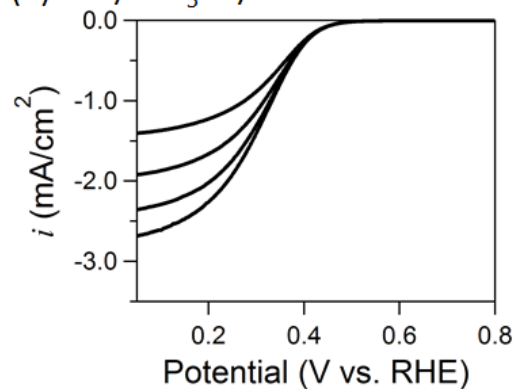
#### 1, CoP series

##### A. Imidazole group

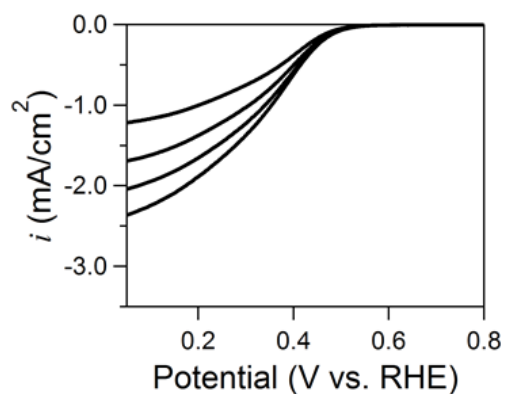
(a) CoP/ImC<sub>3</sub>SH/Au



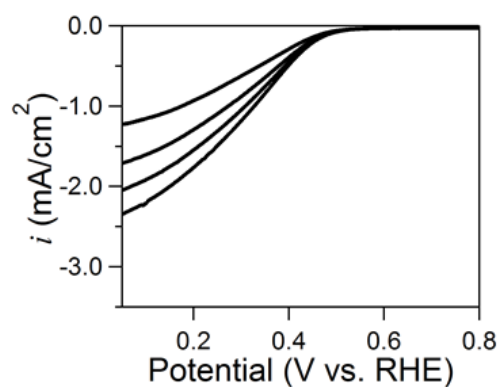
(b) CoP/ImC<sub>5</sub>SH/Au



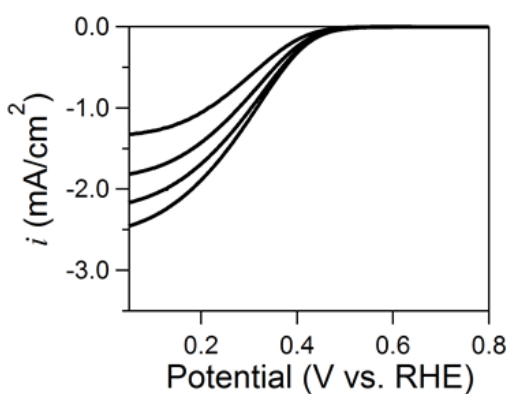
(c) CoP/ImC<sub>7</sub>SH/Au



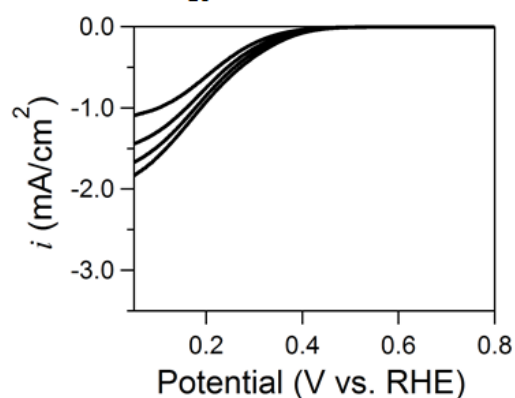
(d) CoP/ImC<sub>8</sub>SH/Au



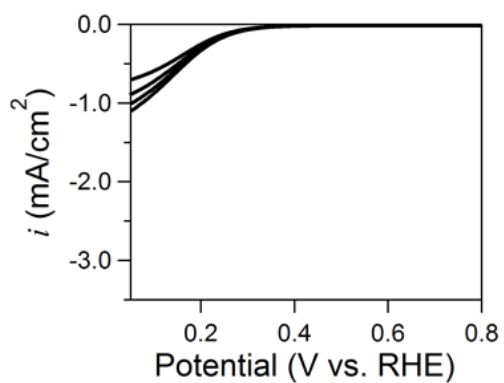
(e) CoP/ImC<sub>9</sub>SH/Au



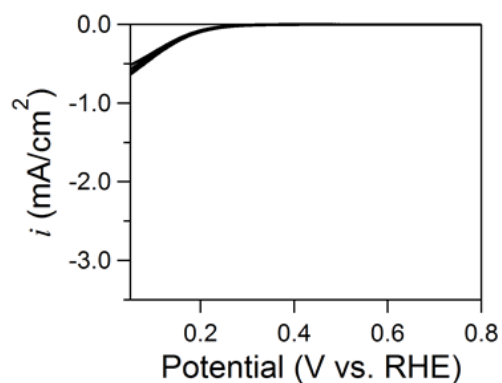
(f) CoP/ImC<sub>10</sub>SH/Au



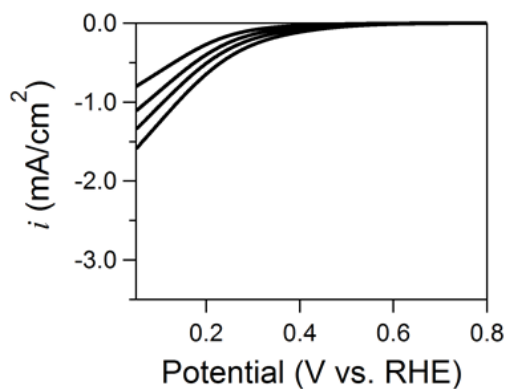
(g) CoP/ImC<sub>11</sub>SH/Au



(h) CoP/ImC<sub>12</sub>SH/Au

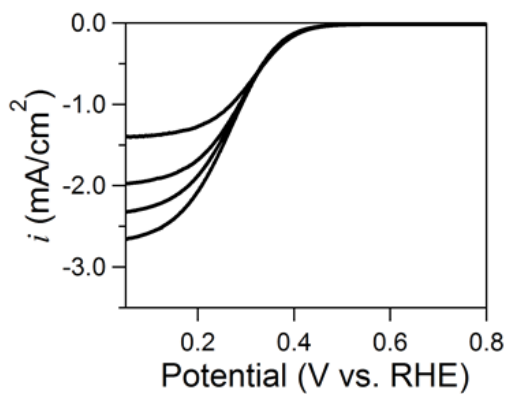


(i) CoP/ImC<sub>10</sub>SH/Pd<sub>ML</sub>/Au

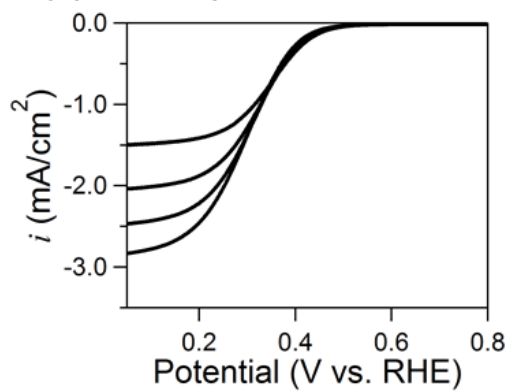


## B. Pyridine group

(a) CoP/PySH/Au

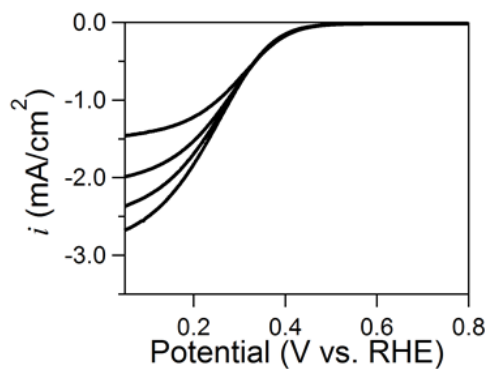


(b) CoP/biPy/Au

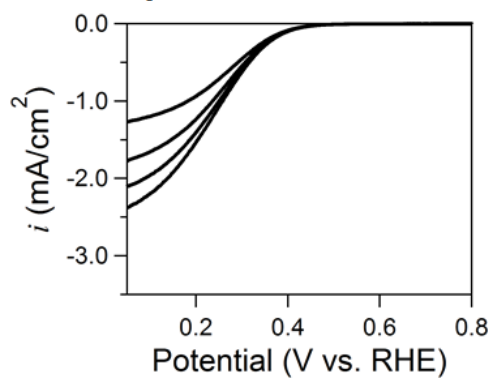


### C. Isocyanide group

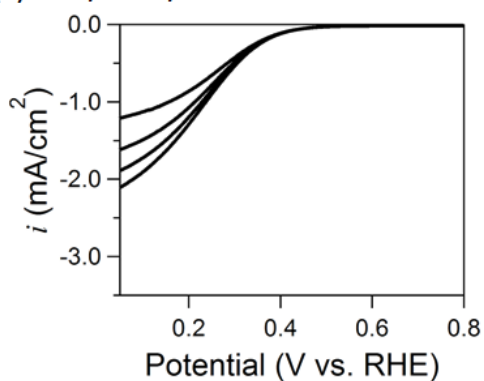
(a) CoP/PDI/Au



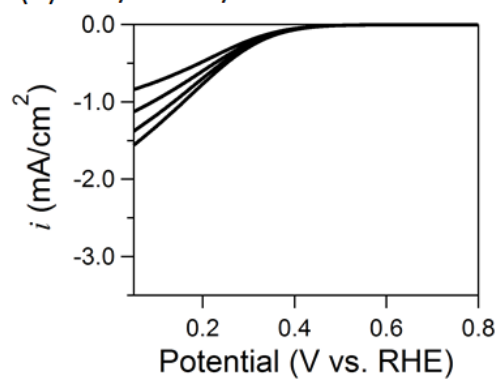
(b) CoP/C<sub>6</sub>DI/Au



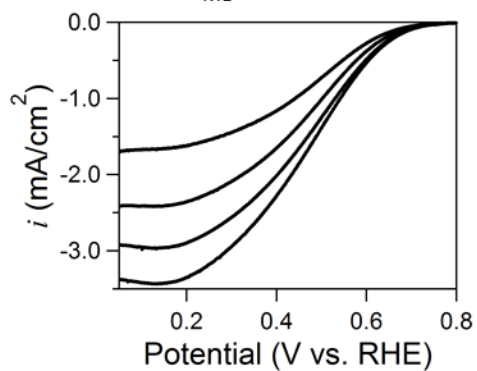
(c) CoP/TPDI/Au



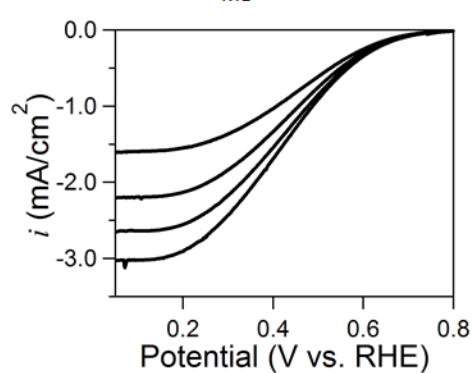
(d) CoP/OPEDI/Au



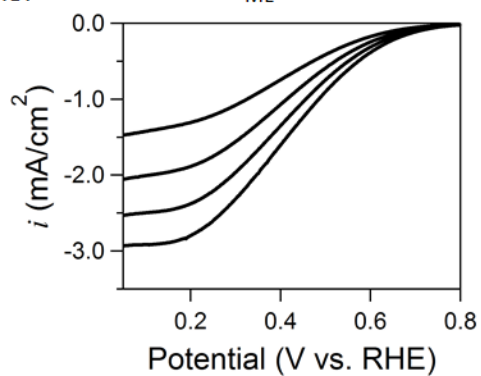
(e) CoP/PDI/Pd<sub>ML</sub>/Au



(f) CoP/TPDI/Pd<sub>ML</sub>/Au



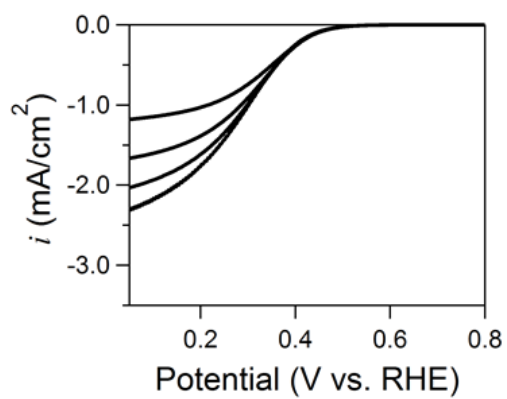
(g) CoP/OPEDI/Pd<sub>ML</sub>/Au



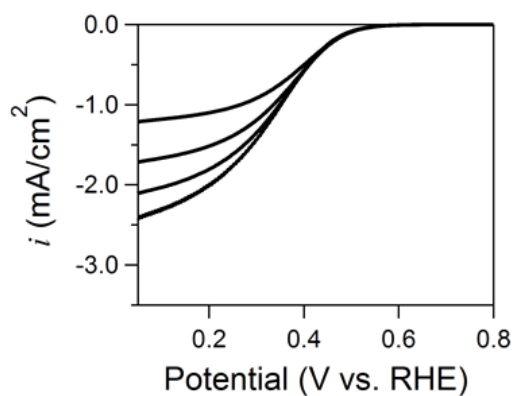
## 2, CoPC series

### A. Imidazole group

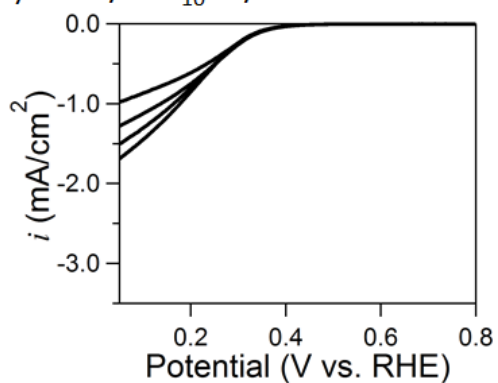
(a) CoPC/ImC<sub>3</sub>SH/Au



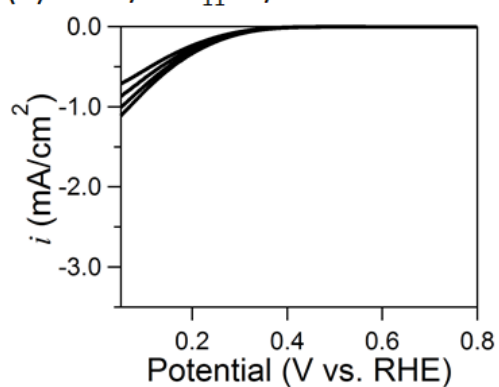
(b) CoPC/ImC<sub>7</sub>SH/Au



(c) CoPC/ImC<sub>10</sub>SH/Au

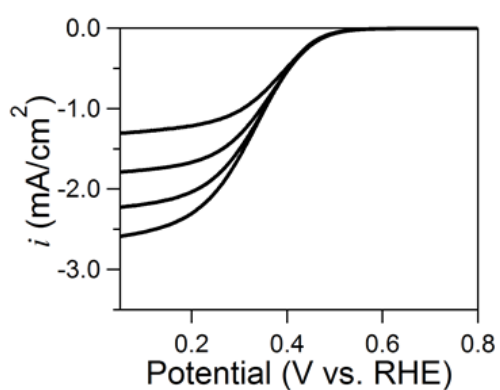


(d) CoPC/ImC<sub>11</sub>SH/Au



### B. Pyridine group

(a) CoPC/PySH/Au



# Chapter 4

## Internal quantum efficiency of photo-induced uphill electron transfer through photo-absorbing dyes connected with an Au electrode

### 4.1 Introduction

In this chapter, we focus on photo-induced uphill electron transfer reactions on a dye-modified electrode. In the case of photo-induced uphill electron transfer systems, back electron transfers and energy transfers must be taken into account as energy dissipation pathways, in addition to the rate-determining issues for downhill electron transfers, which were already discussed in Chapter 3. To achieve efficient photo-energy conversion from the microscopic viewpoints, it is essential to improve the internal quantum efficiency (IQE) as well as to increase the light-harvesting efficiency (LHE). For IQE, enhancement of the charge separation efficiency is one of critical points; various types of photo-absorbing supramolecular units with donors and/or acceptors have been synthesized according to the Marcus theory, as shown in

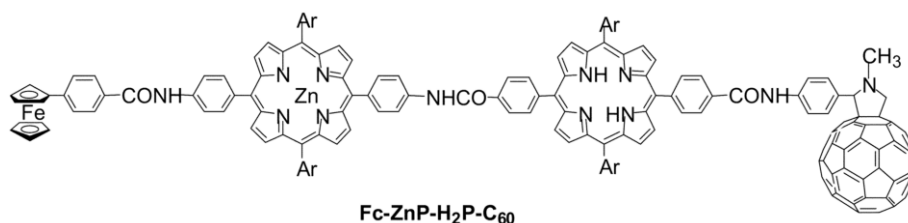


Figure 4.1.1. An example of photo-absorbing supramolecular system having donor and acceptor to improve the efficiency of charge separation. (ref9)

Figure 4.1.1.<sup>1-9</sup> When a photo-absorbing system is immobilized to a metal surface, energy transfers from excited molecules to the metal is known to decrease IQE to a large extent.<sup>10-19</sup> This energy dissipation process is due to electromagnetic interactions between the induced dipoles of excited dye molecules and the mirror dipoles in the metal.<sup>16-19</sup> This undesirable long-range contribution can be minimized when photo-absorbing units are located with large separation from the metal surface. Alternatively, this should make the IET slower, as learnt in Chapter 3. The slow IET rate may decrease the charge separation efficiency. At the same time, however, the back electron transfer rate from the excited states to the metal may be also decreased. Although

some of the previous reports have already addressed this problem, it is of interest to examine both of the electronic and electromagnetic coupling contributions to IQE, based on the advantage of the layer-by-layer method.

For the LHE enhancement, it is essential to increase the optical thickness of photo-absorbing layers. This can be achieved by two methods: molecular design of dyes with larger absorption cross-sections and the increase in the surface density of dye molecules. This may increase the intermolecular electromagnetic coupling such as self-quenching, which will affect the IQE. The intermolecular energy transfer has been extensively studied for randomly distributed dyes in homogenous solution and for a pair of dye molecules with controlled orientation and connection.<sup>20-23</sup> However, limited information is available for the contribution of the intermolecular energy transfer to IQE at an electrified interface.

In this chapter, porphyrin monomers and dimers were connected to Au surface using wire molecules in a layer-by-layer manner. Then, the relation between the electrode-dye separation and IQE was investigated in terms of the IET rate through wire molecules. The contribution of the intermolecular energy transfers to IQE was also investigated by comparison of two different types of porphyrin dimers.

## 4.2 Experimental

The details for preparation and characterization of metalloporphyrin-modified electrodes were described in Chapter 2. All photoelectrochemical studies were performed in a three-electrode electrochemical cell filled with 0.1 M NaClO<sub>4</sub> aqueous solution

containing 5 mM methylviologen (MV<sup>2+</sup>), which function as an electron acceptor, using a potentiostat (Hokuto Denko, HABF-501A). A variety of dye-modified Au electrodes with diameter of 10 mm, shown in Figure 4.2.1, was utilized as a working electrode. A Pt wire and an Ag/AgCl (sat. KCl) were used as counter and reference electrodes, respectively. All electrolyte solutions were purged with ultrapure Ar (99.999 %) for 1 hour prior to each

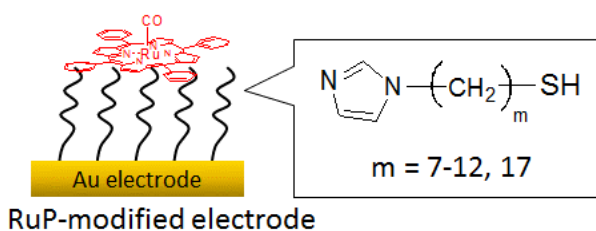


Figure 4.2.1. RuP-modified gold electrode with various lengths of wire molecules.

measurement. The electrodes were illuminated with a 500 W Xe lamp (Ushio, OPM2-502X) through a monochromator (Oriel Conerstone 130). Photocurrent action spectra were measured by scanning the excitation wavelength at 100 nm·min<sup>-1</sup>. The time course of the photocurrent response was measured under pulsed-irradiation at 425 nm with an intensity of 0.95 mW·cm<sup>-2</sup>. The light intensity was measured by an optical power meter (Melles Griot Broadband Power/Energy Meter, 13PEM001).

### 4.3 Contribution of electron- and energy-transfers between the metal substrate and dye molecules to IQE

#### 4.3.1 Photoelectrochemical characteristics of RuP/ImC<sub>9</sub>SH-SAM/Au

A black line in Figure 4.3.1 shows an absorption spectrum of RuP in chloroform solution. Two peaks were observed at 410 nm and 528 nm in the absorption spectrum, which were assigned to the Soret-band and Q-band of the porphyrin rings, respectively. The red line in Figure 4.3.1 shows a cathodic photocurrent action spectrum of RuP/ImC<sub>9</sub>SH-SAM/Au obtained under applied potential of -0.2 V (vs. Ag/AgCl). The two peaks are thought

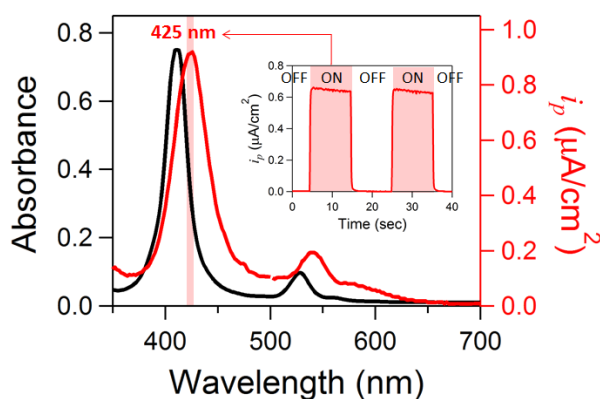


Figure 4.3.1. Absorption spectrum of RuP in chloroform solution (black line) and cathodic photocurrent action spectrum of RuP/ImC<sub>9</sub>SH-SAM/Au under applied potential at -0.2 V vs. Ag/AgCl (red line). Inset: Photoelectrochemical response under the 425-nm light irradiation with 0.95 mW/cm<sup>2</sup>.

to be due to the Soret- and Q-band absorption because of the similar appearance. The immobilization of RuP with the imidazole group is evident in the difference of the peak positions between these spectra. The relatively small shift in RuP, compared with CoP, can be explained by the difference in the coordination number between them; note that RuP is additionally coordinated with CO. These features of the photocurrent action spectrum were observed for other samples with different wire molecules. The inset of Figure 4.3.1 shows the time course of the photocurrent measured under illumination with 425-nm pulses, indicating the reproducible and stable photocurrent responses.

Figure 4.3.2 shows energy diagrams of photocurrent generation at the RuP-modified electrode. The redox potential for RuP\*/RuP<sup>+</sup> was roughly estimated from the Q band transition energy. In this system, the Au electrode gives an electron to a RuP radical cation (RuP<sup>•+</sup>) (1), after the photo-excitation of RuP layer and electron donation to methylviologen (MV<sup>2+</sup>) (2) resulting in the forward electron transfer from the Au electrode to MV<sup>2+</sup>, through the wire layers. This process may be competitive with a back electron transfer from the excited RuP\* to the electrode (3), energy transfer from the excited RuP\* to Au (4), a decay of the excited RuP\* (5) and a back electron transfer from MV<sup>2+</sup> to RuP<sup>•+</sup> (6), and. Therefore, the reduction of these pathways is essential for efficient photocurrent generation.

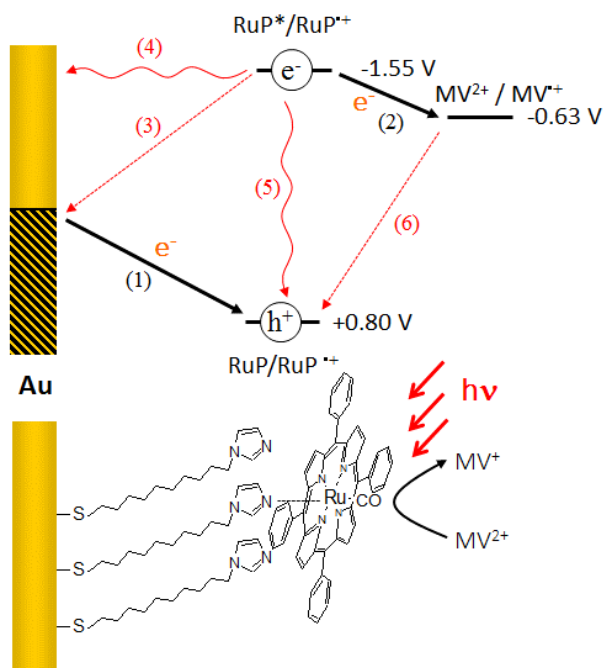


Figure 4.3.2. Energy diagram for photo-induced uphill electron transfer at the RuP-modified electrode. Electron transfer processes, back electron transfer processes, and energy loss processes are indicated as black, red and wavy arrows, respectively.

Figure 4.3.3 shows the potential dependence of the cathodic photocurrent density in RuP/ImC<sub>9</sub>SH-SAM/Au, measured under the 425-nm excitation with 0.95 mW/cm<sup>2</sup>. The photocurrent density significantly increased when more negative potential was applied to the electrode. According to the energy diagram, the more negative potential application can improve the electron transfer rate (1). Therefore, the non-radiative decay of the excited state or charge recombination through the

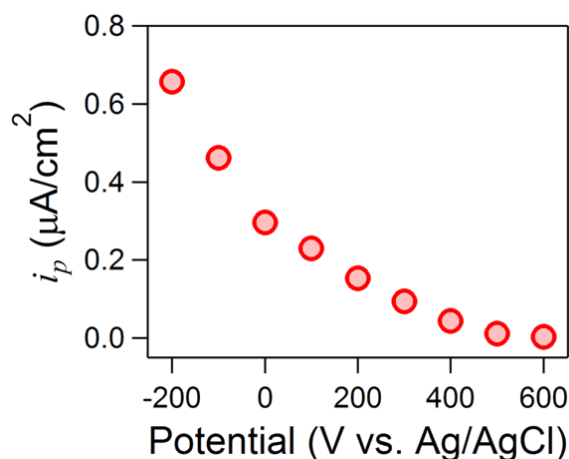


Figure 4.3.3. Photocurrent density vs. applied potential, measured for RuP/ImC<sub>9</sub>SH-SAM/Au under the 425-nm light excitation.

MV<sup>2+</sup>/MV<sup>+</sup> redox is hindered, resulting in the increase in IQE. Incidentally, IQE at -0.2 V was estimated to be 14% by considering the surface density and absorption cross-section of RuP.

### 4.3.2 Wire length dependence of IQE for a series of RuP/wire molecule/Au

The above experiments were repeated for the other wire molecules. Figure 4.3.4a shows the wire length dependence of IQE. This result clearly shows that IQE is maximum at around  $m = 9$ . It should be here pointed that the wire length dependence of  $k_0$  for ORR in Chapter 3 exhibited similar behavior, as shown in Figure 4.3.4b. In the present uphill electron transfer systems, back electron transfers and energy transfers must be taken into account in addition to the issues for determining the rate of the downhill electron transfer. For the contribution of energy transfer from RuP\* to Au, the larger Au-RuP separation is better for the efficient IQE. Therefore, the decrease in the IQE in the longer wire length region is caused by the increase of (4) as a result of the slow electron tunneling through the wire molecules. The rate of the electron transfer (2) in

the photocurrent generation should be different from  $k_0$  for ORR. Nevertheless, the wire length dependence of IQE was very similar with that of  $k_0$ , suggesting that the IET was rate-limiting in the weak coupling region. In the short wire length region, a rapid decrease of IQE was observed

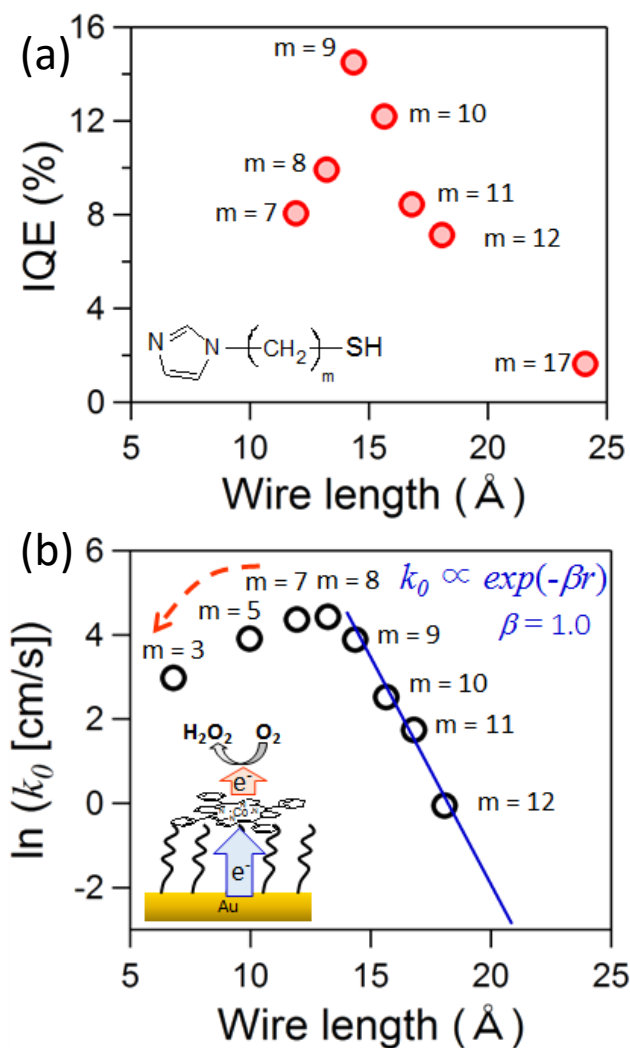


Figure 4.3.4. (a) Plots of IQE obtained for a series of RuP/ImC<sub>m</sub>SH-SAM/Au, and (b) Plots of  $k_0$  obtained for a series of CoP/ImC<sub>m</sub>SH-SAM/Au as a function of the wire length of ImC<sub>m</sub>SH (taken from Chapter 3).

with decreasing of the length. There are several possibilities for explaining the decrease. The excited state quenching should be larger near Au surface. The back electron transfer from RuP\* to Au may also contribute to the decrease of IQE. The strong coupling between Au substrate and RuP may modify the performance of RuP dye molecules, as demonstrated in the ORR experiments. So far, it is difficult to conclude which is the dominant origin for the decrease of IQE near Au surface.

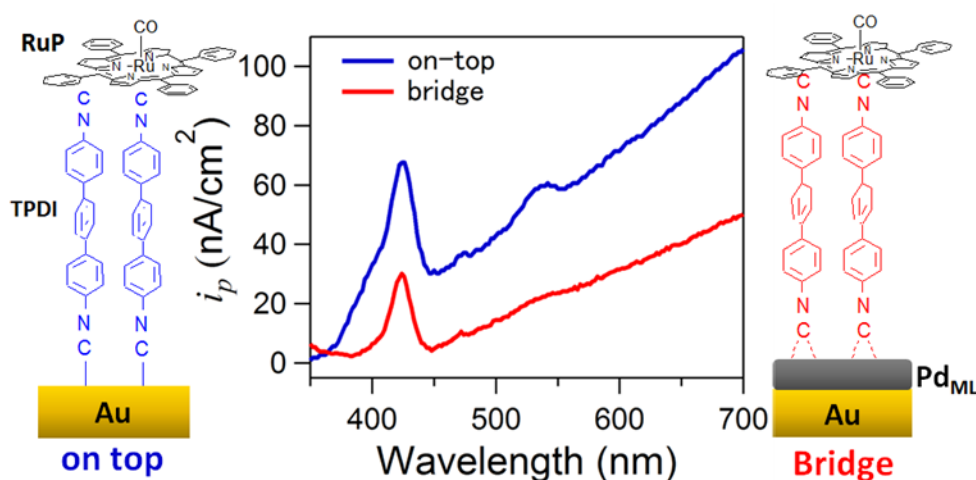


Figure 4.3.5. Cathodic photocurrent action spectrums of on-top (RuP/TPDI-SAM/Au: blue line) and bridge (RuP/TPDI-SAM/Pd<sub>ML</sub>/Au: red line) at -0.2 V vs. Ag/AgCl.

If the proposed model is correct for the decrease of IQE in the long wire region, one can expect that the use of wire molecules with  $\pi$ -conjugated longer body and anchor should improve IQE via the enhancement of IET. To investigate this possibility, TPDI was utilized as a wire molecule. In addition, the Au-TPDI interface structures was changed by using the Pd monoatomic layer (Pd<sub>ML</sub>). (TPDI can be adsorbed on Au surface with on-top configuration and on Pd with bridge configuration.) Figure 4.3.5 shows cathodic photocurrent action spectra for on-top configuration (RuP/TPDI-SAM/Au) and bridge configuration (RuP/TPDI-SAM/Pd<sub>ML</sub>/Au). The incident wavelength was scanned from UV to near IR. Unfortunately, the photocurrent in these systems changed with time, and the obtained photocurrent density was much smaller than those obtained for the series of ImC<sub>m</sub>SH wire molecules. This is probably due to the lower surface density of TPDI-SAMs; the direct reverse electron transfers from MV<sup>2+</sup> to Au can proceed when MV<sup>2+</sup> cations pass through the low-density SAMs. In the case of the electrochemical potential-driven downhill electron transfer reactions such as ORR, such direct reverse electron transfer to Au does not decrease the overall reaction rate. If the electrode surface can be

completely passivated using  $\pi$ -conjugated wire molecules, the efficiency of photocurrent generation is expected to be increased by extension of the electrode-dye separation without lowering the electron tunneling efficiency.

#### 4.4 Contribution of energy-transfer between dye molecules to IQE

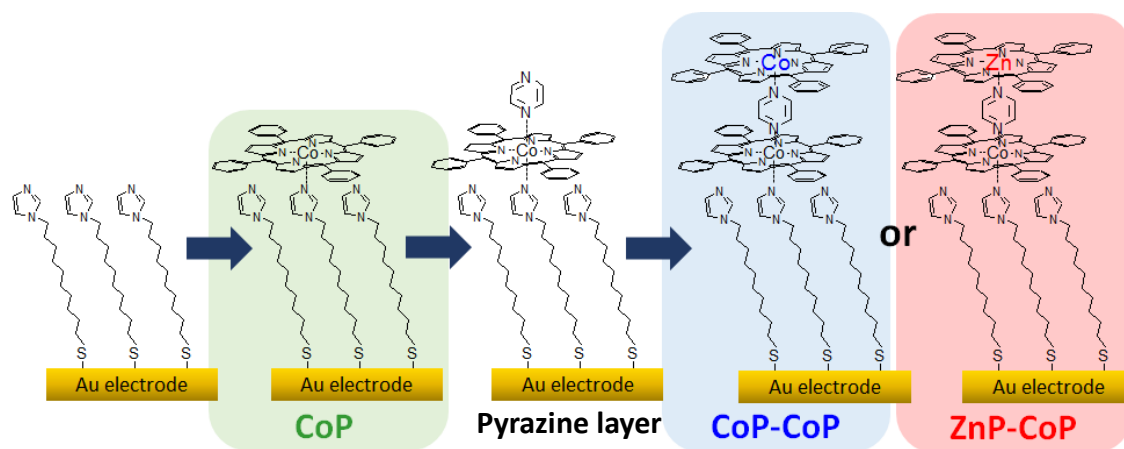


Figure 4.4.1. Schematic illustration of layer-by-layer stepwise assembly of CoP-CoP and ZnP-CoP dimers on Au electrodes.

In this section, two different types of metalloporphyrin dimers with a defined intermolecular distance were immobilized on imidazole-modified Au electrodes. The same molecular layers of ImC<sub>11</sub>SH were utilized as a spacer to compare IQE for these two dimers with fixed Au-porphyrin separation. Figure 4.4.1 shows a layer-by-layer formation process of metalloporphyrin dimers bound to an Au electrode via axial ligation of the central metal ions to ImC<sub>11</sub>SH-SAM. Details of sample preparation is described in Chapter 2. The first porphyrin layer attached to the SAMs was fixed to CoP, and the second layer was altered between CoP and ZnP so that CoP-CoP homo-dimers and ZnP-CoP hetero-dimers were formed. The advantage of this method is that both the electrode-porphyrin distance and porphyrin-porphyrin distance are well controlled by the thickness of the imidazole-terminated monolayer and the size of pyrazine, respectively.

Figure 4.4.2a shows the absorption spectra of chloroform solution containing CoP with and without pyridine. In the absence of pyridine, CoP displayed two absorption peaks at 415 nm and 525 nm, which were assigned to Soret and Q bands, respectively. Upon addition of pyridine, the intensity of the original peaks decreased and new two peaks appear at around 435 and 550 nm. The appearance of the new peaks indicates that pentacoordinated CoP was formed by ligation of pyridine.<sup>24,25</sup> Figure 4.4.2 shows the photocurrent action spectrum of CoP-modified electrode in the presence of MV<sup>2+</sup>. The photocurrent peak was found at 435 nm, which agreed with the absorption band of pyridine-coordinated CoP. This clearly indicates that CoP was indeed immobilized on the SAMs via the axial ligation. The photocurrent peak associated with Q-band was not clearly observed in the

present system, probably due to the relatively large background photocurrent response. As shown the red line in Figure 4.4.2b, the SAM-modified electrode without CoP didn't show any photocurrent response. Moreover, no photocurrent observed on the CoP-modified electrode in the absence of MV<sup>2+</sup>, indicating that the photo-induced charge transfer takes place from the electrode to MV<sup>2+</sup> through the excited state of CoP. Incidentally, the photocurrent response irradiated with 435 nm light is presented in the inset of Figure 4.4.2b, showing that the CoP layer is stable under photo illumination. Similar behavior was observed for CoP-CoP and ZnP-CoP dimers, too.

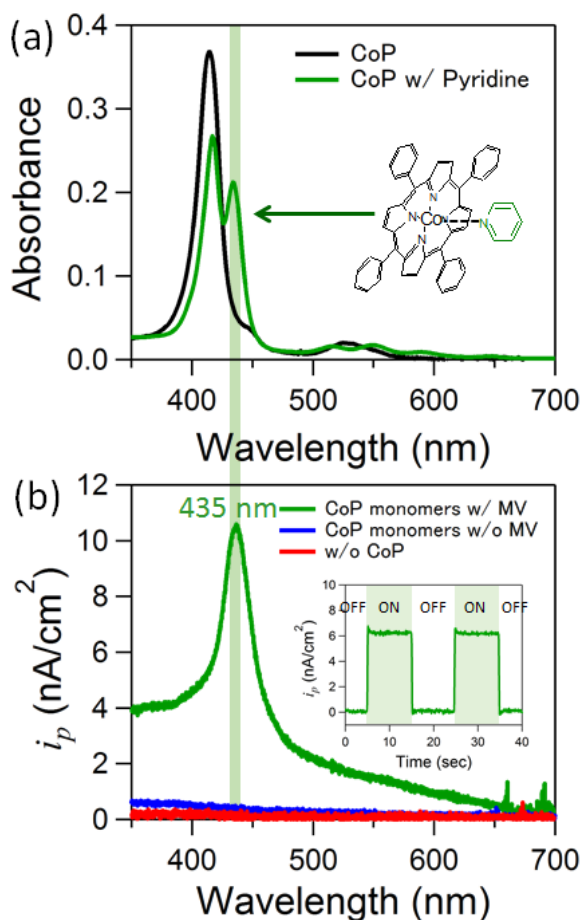


Figure 4.4.2. (a) Absorption spectra of CoP (black line) and a mixture of CoP and pyridine (green line) in chloroform solution. (b) Cathodic photocurrent action spectra of CoP monomer on the electrode with (green line) and without MV<sup>2+</sup> (blue line) and w/o CoP layer (red line) at -0.1 V vs. Ag/AgCl. Inset: Photoelectrochemical response of CoP monomer w/ MV<sup>2+</sup> under the 435-nm light irradiation with 0.9 mW/cm<sup>2</sup>.

Figure 4.4.3 shows the comparison of cathodic photocurrent action spectra measured on CoP monomer, pyrazine layer, and CoP-CoP dimer, where pyrazine layer denotes pyrazine-coordinated CoP layers formed on the surface. As already discussed in Chapter 2, the surface density of CoP between CoP monomer and pyrazine layer did not change. Nevertheless, the photocurrent of pyrazine layer was

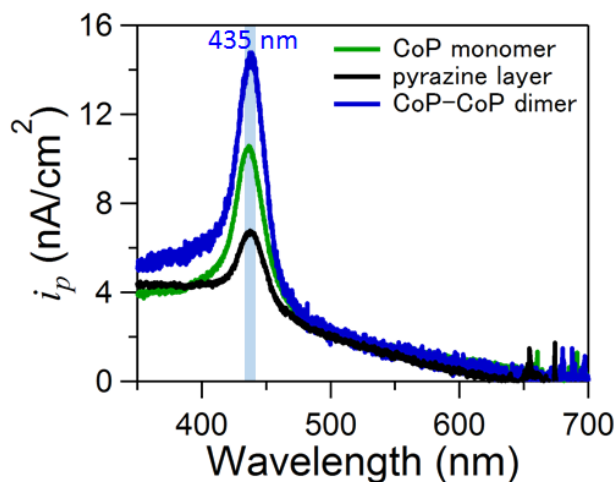


Figure 4.4.3. Cathodic photocurrent action spectra of CoP monomer (green line), pyrazine layer (black line), and CoP-CoP dimer (blue line) at -0.1 V vs. Ag/AgCl.

smaller than that of CoP monomer. This indicates that pyrazine adsorption inhibited electron transfer from  $\text{CoP}^*$  to  $\text{MV}^{2+}$ , suggesting that Co central ions function as an electron transfer active site. On the other hand, the photocurrent of CoP-CoP dimer increased with increasing surface density of CoP. Importantly, the Soret band position did not show any shift among the samples, indicating that the electronic structure of CoP was not affected much by the construction of the dimer structure.

The cathodic photocurrent densities of CoP monomer, and CoP-CoP and ZnP-CoP dimers, measured under the 435-nm excitation with 0.9 mW/cm<sup>2</sup>, are plotted as a function of the applied electrochemical potential, as shown in Figure 4.4.4a. In the case of CoP, the photocurrent increased with changing the potential to the negative direction. Since light-harvesting efficiency (LHE) is independent of the potential, this variation is simply explained by the potential dependence of IQE. In the case of the two dimers, the potential dependence of the photocurrent was rather complicated; when the more negative potential was applied, the photocurrent of the dimers was notably larger than that of the monomer. However, when the applied potential was changed to the positive direction, the photocurrent of

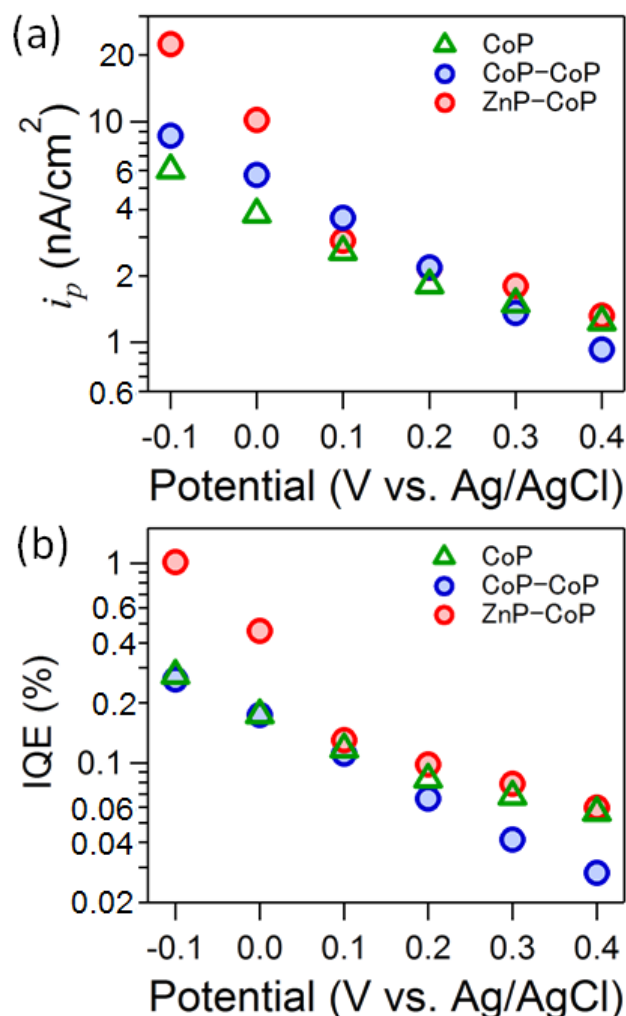


Figure 4.4.4. (a) Photocurrent densities vs. applied potential, measured for CoP (green triangles), CoP-CoP (blue circles), and ZnP-CoP (red circles) under the 435-nm light excitation. (b) IQE vs. applied potential, estimated from (a).

the dimers decreased more rapidly than that of CoP. In particular, the photocurrent of CoP-CoP was even smaller than that of CoP at +0.4 V. Since LHE is larger in the dimers than in the monomer, the larger photocurrent of the dimers at the negative potential region can be explained by the increase in LHE. (The surface density of porphyrin was estimated to be  $7.5 \times 10^{-12}$  mol·cm<sup>-2</sup> for CoP,  $11.5 \times 10^{-12}$  mol·cm<sup>-2</sup> for CoP-CoP, and  $13.5 \times 10^{-12}$  mol·cm<sup>-2</sup> for ZnP-CoP from the redox charge of the central metal ions, as already shown in Chapter 2.) On the other hand, these larger LHE in the dimers did not increase the photocurrent at the positive potential region, suggesting that IQE was different between the dimers and the monomer. This is indeed

more clearly presented when the photocurrent density was converted to IQE by considering the surface density and the absorption cross-section of the porphyrins, as shown in Figure 4.4.4b. At the negative potential region, CoP and CoP-CoP showed the same IQE, meaning that the larger photocurrent in CoP-CoP at this potential region was purely due to the larger LHE in the dimer. Notably, ZnP-CoP showed larger IQE than CoP, suggesting that IQE was indifferent between the homo- and hetero-dimers. In contrast, at the positive potential region, CoP-CoP showed smaller IQE than CoP whereas ZnP-CoP did similar IQE with CoP. This also implies that the contribution of the dimer formation to IQE was different between homo- and hetero-dimers.

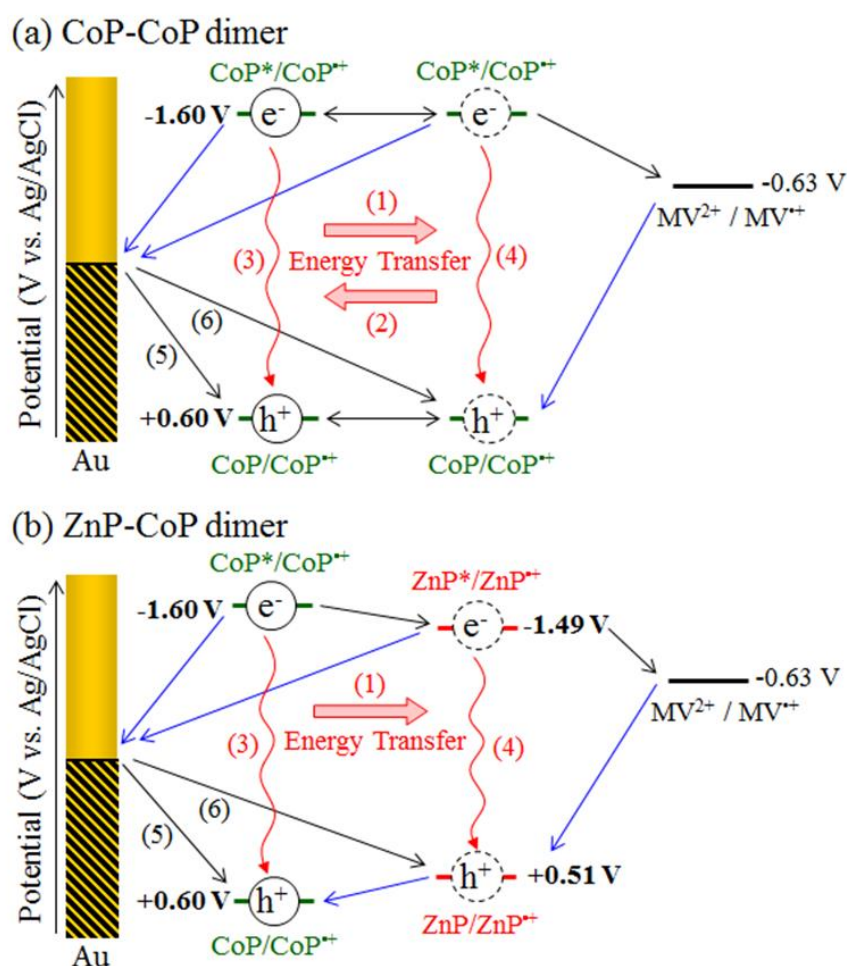


Figure 4.4.5. Energy diagrams for (a) CoP-CoP homo-dimer system, and (b) ZnP-CoP hetero-dimer system. Electron transfer processes, energy loss processes, and energy transfer processes are indicated as straight, wavy, and bold arrows, respectively.

Figure 4.4.5 shows energy diagrams of photocurrent generation in the two dimer systems. The redox potentials for CoP/CoP<sup>+</sup> and ZnP/ZnP<sup>+</sup> were obtained from the cyclic voltammograms

of the modified electrodes. The potentials for  $\text{CoP}^*/\text{CoP}^+$  and  $\text{ZnP}^*/\text{ZnP}^+$  were roughly estimated from the Q band transition energy. Under irradiation with a conventional light intensity, one can assume that two porphyrins in a dimer are not excited simultaneously. That is, one electro-hole pair is created in a dimer when the molecular system is excited. Therefore, resonance energy transfers in the dimers are expected to play an important role to determine IQE. In the case of the CoP-CoP homo-dimer, the energy transfer from the excited  $\text{CoP}^*$  to the ground state CoP can occur back and forth in the dimer (the energy transfer paths (1) and (2)). This leads to a decrease in the lifetime of the excited state through the quenching paths (3) and (4). Consequently, the photocurrent in the CoP-CoP dimer becomes smaller than that in the CoP monomer. It is here noted that the applied potential at the molecule-electrode interface can lower the free energy barrier for the electron transfer (5) or (6), resulting in an increase of IQE through the formation of the long-lived excited states for both of the CoP and CoP-CoP systems only at the negative potential region. Then, the difference of IQE between CoP and CoP-CoP becomes negligible in the presence of a sufficient interface potential. In the case of the ZnP-CoP hetero-dimer, the energy transfer can take place only from the excited  $\text{CoP}^*$  to the ground state ZnP because of the energy difference in the excited state formation. Therefore, a decrease of the lifetime of the excited states in the dimers may not be significant even at the positive potential region. When the more negative potential is applied, the efficient electron transfer from the electrode to the excited hole in the dimers is expected as well as the efficient energy transfer from CoP to ZnP, leading to the larger IQE than that in the monomer. As a result, the photocurrent is largely enhanced in this case.

## 4.5 Conclusion

In this chapter, the porphyrin monomer system was constructed on Au surface with various wire molecules to control the Au-porphyrin distance. The porphyrin dimers with the fixed porphyrin-porphyrin distance were also prepared on Au surface with a defined Au-porphyrin separation. The contribution of the electron- and energy-transfers at the metal-porphyrin interfaces and at the porphyrin-porphyrin connections was investigated in terms of IQE for the photo-driven uphill electron transfers.

First, in the case of the porphyrin monomer, the wire length dependence of IQE showed the similar tendency with that of  $k_0$  for ORR, even though the energy loss from the excited porphyrins to Au was expected to decrease with the length of wire molecules. This result indicates that the rate of IET via the wire molecules critically determine the charge separation efficiency, and hence, IQE. In principle, the use of  $\pi$ -conjugated long wire molecules should improve IQE although the experimental attempt did not succeed because of the undesirable contribution of the direct reverse electron transfer from acceptors to Au.

Next, in the case of the porphyrin dimer model, IQE was affected by the direction of the energy transfer between dye-molecules. The unidirectional energy transfer increased IQE due to the enhancement of charge separation efficiency. In contrast, the bidirectional energy transfer decreased IQE because of the lowering of the lifetime of excited states. The enhancement of LHE, i.e., the increase of surface density of dye molecules, may causes the lowering of IQE via the intermolecular energy transfers. On the other hand, sequential excitation energy transfers from higher-energy dyes to lower-energy dyes is believed to be a key strategy in natural photosynthetic systems. Control of energy and electron transfers using molecular-scale design is indispensable for developing efficient photo-energy conversion systems with high IQE and LHE.

## References

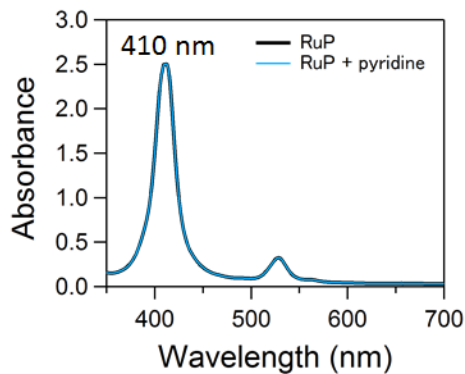
- (1) Vilan, A.; Yaffe, O.; Biller, A.; Salomon, A.; Kahn, A.; Cahen, D. *Adv. Mater.*, **2010**, *22*, 140.
- (2) Marcus, R. A.; Sutin, N. *Biochim. Biophys. Acta*, **1985**, *811*, 265.
- (3) Marcus, R. A. *Angew. Chem. Int. Ed. Engl.*, **1993**, *32*, 1111.
- (4) Mataga, N.; Asahi, T.; Kanda, Y.; Okada, T. *Chem. Phys.*, **1988**, *127*, 249.
- (5) Wasielewski, M. R. *Chem. Rev.*, **1992**, *92*, 435.
- (6) Imahori, H.; Sakata, Y. *Adv. Mater.*, **1997**, *9*, 537.
- (7) Fukuzumi, S.; Imahori, H. in *Electron Transfer in Chemistry*, ed. V. Balzani, Wiley-VCH, Weinheim, 2001, vol. 2, pp. 270-337
- (8) Ebersson, L. *Electron Transfer Reactions in Organic Chemistry; Reactivity and Structure*, Springer, Heidelberg, 1987, vol. 25.
- (9) Imahori, H.; Guldi, D. M.; Tamaki, K.; Yoshida, Y.; Luo, C.; Sakata, Y.; Fukuzumi, S. *J. Am. Chem. Soc.*, **2001**, *123*, 6617.
- (10) Uosaki, K.; Kondo, T.; Zhang, X.-Q.; Yanagida, M. *J. Am. Chem. Soc.* **1997**, *119*, 8367.
- (11) Imahori, H.; Norieda, H.; Ozawa, S.; Ushida, K.; Yamada, H.; Azumi, T.; Tamaki, K.; Sakata, Y. *Langmuir* **1998**, *14*, 5335.
- (12) Fukuzumi, S. *Org. Biomol. Chem.* **2003**, *1*, 609.
- (13) Yamada, H.; Imahori, H.; Nishimura, Y.; Yamazaki, I.; Ahn, T. K.; Kim, S. K.; Kim, D.; Fukuzumi, S. *J. Am. Chem. Soc.* **2003**, *125*, 9129.
- (14) Imahori, H.; Norieda, H.; Nishimura, Y.; Yamazaki, I.; Higuchi, K.; Kato, N.; Motohiro, T.; Yamada, H.; Tamaki, K.; Arimura, M.; Sakata, Y. *J. Phys. Chem. B* **2000**, *104*, 1253.
- (15) Imahori, H.; Norieda, H.; Yamada, H.; Nishimura, Y.; Yamazaki, I.; Sakata, Y.; Fukuzumi, S. *J. Am. Chem. Soc.* **2001**, *123*, 100.
- (16) Chance, R. R.; Prock, A.; Silbey, R. *Adv. Chem. Phys.* **1978**, *37*, 1.
- (17) Waldeck, D. H.; Alivisatos, A. P.; Harris, C. B. *Surf. Sci.* **1985**, *158*, 103.
- (18) Zhou, X.-L.; Zhu, X.-Y.; White, J. M. *Acc. Chem. Res.* **1990**, *23*, 327.
- (19) Cnossen, G.; Drabe, K. E.; Wiersma, D. A. *J. Chem. Phys.* **1993**, *98*, 5276.
- (20) Nagata, T.; Osuka, A.; Maruyama, K. *J. Am. Chem. Soc.*, **1990**, *112*, 3054.
- (21) Schwarz, F. P.; Gouterman, M.; Muljiani, Z.; Dolphin, D. H. *Bioinorg. Chem.* **1972**, *2*, 1.
- (22) Gonen, O.; Levanon, H. *J. Chem. Phys.* **1986**, *84*, 4132.

- (23) Kilså, K.; Kajanus, J.; Mårtensson, J.; Albinsson, B. *J. Phys. Chem. B* **1999**, *103*, 7329.
- (24) Stynes, D. V.; Stynes, H. C.; Ibers, J. A.; James, B. R. *J. Am. Chem. Soc.* **1973**, *95*, 1142.
- (25) Nappa, M.; Valentine, J. S. *J. Am. Chem. Soc.* **1978**, *100*, 5075.

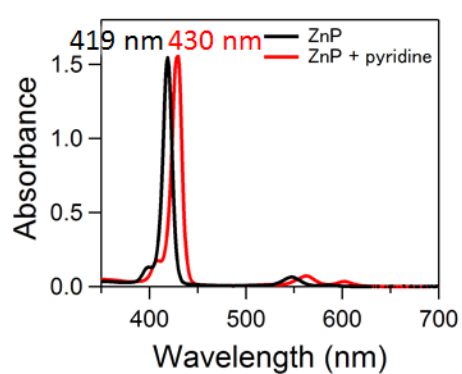
## Appendix

### A. Absorption spectra

(a) RuP and a mixture of RuP and pyridine in chloroform solution

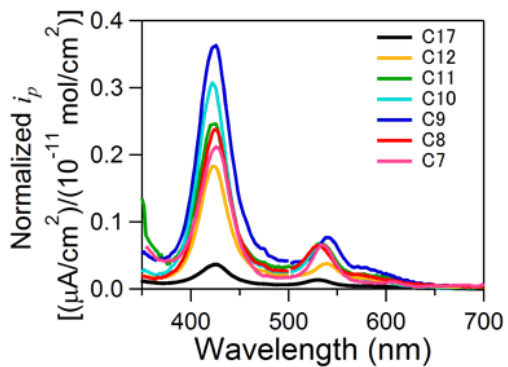


(b) ZnP and a mixture of ZnP and pyridine in chloroform solution

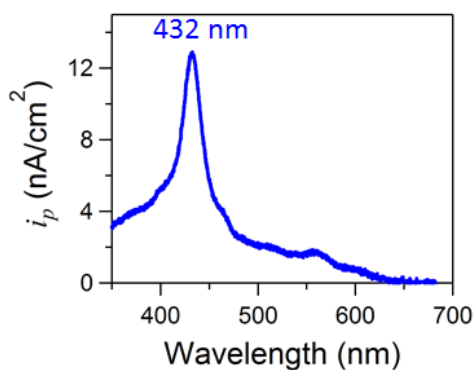


### B. Cathodic photocurrent action spectra

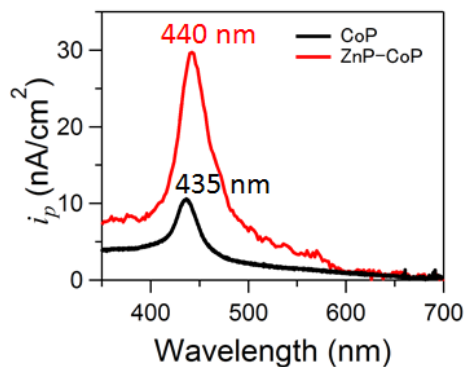
(a) RuP monomer formed on various wire molecules



(b) ZnP monomer formed on ImC<sub>11</sub>SH-SAM



(c) CoP monomer and ZnP-CoP dimer formed on ImC<sub>11</sub>SH-SAM



# Chapter 5

## General conclusion

---

In this thesis, kinetics of the electrochemical and photoelectrochemical reactions at molecule-modified electrodes has been treated in order to improve the understanding of the underlying interfacial electron transfer phenomena and to present a molecular-scale strategy of surface functionalization. The simplified model system consisting of a conducting substrate, molecular wires, and functional molecules was fabricated by layer-by-layer assembly. Thus, the wide variety of combinations of molecular components was able to be examined experimentally, which enabled disentangling the contributions of the performance of the functional groups and the electronic connection through the wires to the overall reactions. In particular, metalloporphyrins and metallophthalocyanines were selected as a model of the functional molecule because of their catalytic activity for ORR and capability for photo-absorption, and the electron transfers for both of the potential-driven downhill and photo-driven uphill processes were investigated using the same model system.

### **The relation between surface structures and electron transfer reactions through catalytic active sites**

Atomic and molecular scale design for catalytic active sites on an electrode surface is one of the most essential problems in the field of electrocatalysis. However, the local electronic property of active sites is usually coupled with that of the conducting substrate, resulting in the difficulty in development of highly efficient electrocatalysts. It is difficult to perform first-principles calculations for a system consisting of conducting and localized electronic states. For better understanding of this problem, the electronic coupling between active sites and substrate was controlled by alternating molecular wires with various structures. The kinetic study of ORR clearly showed that the activity of the catalyst molecules was significantly suppressed under the strong coupling condition while the coherent quantum electron tunneling via the molecular wires was rate-limiting under the weak coupling condition. It was found that the metal-anchor contact was also an essential factor to limit the electron transfer rate. The use of resonance electron tunneling through LUMO of wire molecules and the  $\pi$ -back donating metal-anchor junction largely improved the overall reaction rate in both of the strong coupling and weak coupling

regions.

### **The relation between surface structures and uphill electron transfers through photo-absorbing sites**

Uphill electron transfer is a central issue of photo-energy conversion. To develop a highly efficient system, energy losses via back electron transfers and energy transfers must be taken into account, in addition to the issues for the downhill electron transfers discussed in Chapter 3. The undesirable contribution from these two energy loss paths will decrease with increasing the electrode-dye separation. However, the relation between the photocurrent and the electrode-dye separation clearly exhibited that the slow internal electron transfers dominantly limit the IQE. The use of  $\pi$ -conjugated long wire molecules may improve the IQE in the weak coupling region. Moreover, resonant energy transfer among neighboring dye molecules largely affected IQE; the unidirectional energy transfer enhanced IQE while the bidirectional one contributed oppositely.

### **Future perspective**

In this thesis, both of uphill and downhill electron transfer kinetics was examined from the fundamental aspects. The electronic coupling between a conducting substrate and functional groups was of great importance that significantly affected the overall performance of the functional electrode system. The development of a functional surface can be simplified by separate consideration of molecular-scale design for functional sites and tuning of the electronic connection between the functional sites and the conducting substrate. This methodology for the interface design is in principle useful for development of practical devices such as electrocatalysts in fuel cells or solar-energy conversion in organic solar cells. In such devices, the high density of active sites is needed in addition to the high performance of each active site to deliver high current output. The present study was conducted using two-dimensional planar system with nearly ideal interface structures on the molecular scale. Apparently, three-dimensional integration of active sites is an essential issue we must overcome for practical devices. Especially in solar cells, formation of optically thick organic layers is indispensable for efficient light harvesting, and hence, the energy transfer loss among neighboring dye molecules can be a serious problem. The idea for controlling electron and energy transfers at two-dimensional surfaces will be relevant to three-dimensional systems.

## Acknowledgments

I would like to express my sincere gratitude to Prof. Kei Murakoshi for continuous encouragement and discussion throughout this thesis work.

I am deeply grateful to Prof. Katsuyoshi Ikeda for his continuous guidance and support during my graduate work and for his great ideas that formed the basis of this thesis work. Whenever I needed help or inspiration, he was always available to give me advice. His scientific knowledge, intuition, and clarity of thinking have set an example to me.

I want to express my deep gratitude to Prof. Kohei Uosaki of National Institute for Materials Science (NIMS). He gave me accurate advice in regards to me too and I sincerely enjoyed NIMS life.

I also would like to express deep acknowledgment to Prof. Koichiro Ishimori, Prof. Takanori Suzuki and Prof. Hiroki Habazaki for their valuable discussion and helpful suggestions.

I am thankful to Dr. Satoshi Yasuda, Dr. Kenta Motobayashi (Nagoya Institute of Technology) and Dr. Hidenori Noguchi for their valuable discussion and helpful suggestions. I would like to thank Dr. Kenji Hara (Tokyo University of Technology) for providing the TPDI and OPEDI molecules. I am grateful to all the colleagues of the Laboratory of Physical Chemistry, Department of Chemistry, Graduate School of Science, Hokkaido University, Nanomaterials and Surface Science Laboratory, Department of Engineering Physics, Electronics, and Mechanics at Nagoya Institute of Technology and Global Research Center for Environment and Energy based on Nanomaterials Science (GREEN) at NIMS for their indispensable comments and for giving me cheerful and productive life in the Labs.

Finally, I would like to express my greatest gratitude to my parents and my brothers for their hearty support and encouragement throughout these years, without which I would not be able to achieve this work.

March, 2016

Shino Sato